Development of high quality silicon nitride chips for integrated nonlinear photonics

Houssein El Dirani

N°d'ordre NNT : 2019LYSEC27

THESE de DOCTORAT DE L'UNIVERSITE DE LYON
opérée au sein de l'Ecole centrale de Lyon

Ecole Doctorale Electronique, Electrotechnique, Automatique

Spécialité de doctorat :Dispositifs photoniques et optoélectroniques
Discipline :Optique non linéaire

Soutenue publiquement le 07/10/2019, par :

Houssein EL DIRANI

Master-2 en optoélectronique de l'École Nationale Supérieure de Physique, Électronique et Matériaux (Phelma, Grenoble, France)

Development of high quality Silicon nitride chips for integrated nonlinear photonics

Composition du jury

***M**. D. BAJONI*	*Professeur, University of Pavia (Italy)*	*en qualité d'examinateur*
***M**. B. KUYKEN*	*Professeur, Ghent University (Belgium)*	*en qualité de rapporteur*
***M**. C. SCIANCALEPORE*	*Ingénieur chercheur optique, CEA-Leti*	*en qualité d'examinateur*
***M**. S. COMBRIE*	*Ingénieur chercheur optique, Thales TRT*	*en qualité d'examinateur*
***M**. G. LEO*	*Professeur, Université Paris Diderot*	*en qualité de rapporteur*
***Mme** C. MONAT*	*Professeur, Ecole Centrale de Lyon*	*en qualité d'examinateur*
***M**. X. LETARTRE*	*Directeur de recherche (INL-CNRS)*	*en qualité de directeur de thèse*

To my family…

Acknowledgements

This PhD thesis was a collaboration between CEA-LETI (Grenoble) and Lyon nanotechnology institution.

First, I would like to thank the members of the jury for the time spent to evaluate this work and attend my PhD defense. Thank you, Prof. Daniele Bajoni, Prof. Bart Kuyken, Prof. Giuseppe Leo and Dr. Sylvain Combrié.

Foremost, I would like to express my deepest sense of gratitude to my advisors Corrado Sciancalepore, Christelle Monat and Xavier Letartre. Without them this thesis might not have been written. Thank you Christelle Monat not only for your continuous support of my PhD study and research but also for your personality and the way of thinking and dealing with things. No words can express my thanks to Corrado Sciancalepore for your daily support, patience, motivation, enthusiasm, and immense knowledge. I have learned a lot from you not only in scientific domain but also with your advices for daily life.

I would like to thank all the members of LETI-DOPT/DTSI departments and LTM at CEA-Grenoble for their precious help and practical advices. Special thanks to B. Szelag, E. Pargon, C. Petit-Etienne, S. Kérdiles, V. Muffato, S. Brision and S. Garcia for helping me to explore the clean room horizon and the details of a process flow.

I am indebted to Ayman Nassar Kamel from DTU, Sylvain Boust from III-V Lab and Philippe Grosse for the help to characterize my chips. I could not forget to thank also Prof. F. Van dijk Prof. K. Yvind, Prof. M. Pu and Prof. L. K. Oxenløwe for their valuable comments and suggestions.

Particular thanks to all my friends with whom I shared unforgettable moments. Thank you Federico, Loraine, Mrad, Vincent, Marco, Bayram, Mathieu and … There are too many to write here and I would not like to forget anyone.

I cannot finish without saying how grateful I am to my family. Without them I could not have been succeeded my career. Thank you my father Souleiman, my mother Daad and of course thank you my only brother and best mate Hassan.

Thank you for supporting and encouraging me all the time.

Thank you all.

Abstract

The data traffic need for ultra-high definition videos as well as for the mobile data continues to grow. Within the last decade, optical frequency combs have revolutionized the telecommunications field and paved the way for groundbreaking data transmission demonstrations at previously unattainable data rates. Beside the telecommunications field, optical frequency combs brought benefits also for many other applications such as precision spectroscopy, chemical and bio sensing, optical clocks, and quantum optics. The efficiency of the four-wave mixing phenomenon from which the optical frequency comb arises critically depends on the propagation losses and consequently on the device roughness induced by the lithography and the etching processes. In addition, the bulk material absorption reduces the efficiency of the nonlinear phenomena. By using state-of-the-art complementary metal oxide semiconductor processes, the roughness can be reduced thanks to the maturity of the manufacturing, while the material bulk absorption can be reduced by thermal treatments. In addition, using a CMOS material enables a low-cost fabrication and the co-integration with electronic devices into the same chip.

Silicon-nitride-on-insulator is an attractive CMOS-compatible platform for optical frequency comb generation in the telecommunication band because of the low two-photon absorption of silicon nitride when compared with crystalline silicon. However, the as deposited silicon nitride has a hydrogen related absorption in the telecommunication band. Although high-temperature annealing has been traditionally used to reduce the hydrogen content and successfully demonstrate silicon nitride-based frequency combs, this approach made the co-integration with silicon-based optoelectronics elusive, thus reducing dramatically its effective complementary metal oxide semiconductor compatibility.

In this thesis, we report on the fabrication and test of annealing-free silicon nitride nonlinear photonic circuits. In particular, we have developed a process to fabricate low-loss, annealing-free and crack–free Si_3N_4 740-nm-thick films for Kerr-based

nonlinear photonics, featuring a full process compatibility with front-end silicon photonics. Experimental evidence shows that micro-resonators using such annealing-free silicon nitride films are able to generate a frequency comb spanning 1300-2100 nm via optical parametrical oscillation based on four-wave mixing. In addition, we present the further optimized technological process related to annealed silicon nitride optical devices using high-confinement waveguides, allowing us to achieve record-low losses. This was enabled via a carefully tailored patterning etching process and an annealing treatment particularly efficient due to the already low hydrogen content in our as-deposited silicon nitride. Such improved Si_3N_4 platform allowed us to demonstrate on-chip integrated Kerr frequency comb sources using silicon nitride resonators that were butt-coupled to a III-V DFB laser used as a pump source. This proof of concept proves the validity of our approach for realizing fully packaged compact optical frequency combs.

Keywords: (130.0130) Integrated optics; (130.3120) Integrated optics devices; (130.3130) Integrated optics materials; (190.0190) Nonlinear optics; (270.0270) Quantum optics; (190.4380) Four wave mixing.

Résumé

La montée exponentielle du trafic de données liée au développement de l'interconnexion entre objets et personnes sur la toile nécessite de nouvelles technologies. Au cours de la dernière décennie, les peignes de fréquences optiques ont révolutionné le secteur des télécommunications, ouvrant la voie à une transmission de données à un débit de données auparavant inaccessible. Mis à part le domaine des télécommunications, les peignes de fréquences optiques ont été avantageusement exploités dans d'autres domaines comme la détection optique, la détection chimique, les horloges optiques… L'efficacité du phénomène de mélange à quatre ondes, qui sous-tend la génération des peignes de fréquences, dépend de manière significative des pertes par propagation dans les guides d'ondes optiques et, par conséquent, de la rugosité de ces derniers. De plus, l'absorption intrinsèque du matériau réduit l'efficacité des phénomènes non linéaires tout en contribuant à l'atténuation du signal lumineux dans le milieu optique de propagation. Grâce à la maturité des procédés de fabrication dits CMOS, la rugosité peut être réduite en optimisant la gravure, tandis que l'absorption peut être réduite par des traitements thermiques. L'utilisation d'un matériau CMOS permet donc une fabrication à faible coût et la co-intégration avec d'autres dispositifs optoélectroniques sur la même puce.

Le nitrure de silicium sur isolant est une plateforme prometteuse pour la génération de peignes de fréquences optiques grâce à la faible absorption à deux photons dans ce matériau par rapport au silicium cristallin. Cependant, le nitrure présente une absorption dans la bande des télécommunications relié à la présence des liens moléculaires N-H. Tandis que des recuits à haute température ont été utilisés pour réduire le contenu en hydrogène du film et démontrer avec succès la génération de peignes de fréquence, ces procédés rendent la co-intégration monolithique de ces dispositifs en nitrure de silicium avec une optoélectronique à base de silicium très difficile, réduisant ainsi considérablement sa compatibilité avec les autres matériaux

CMOS. Dans cette thèse, nous décrivons la conception, la fabrication et les caractérisations de circuits photoniques non-linéaires en nitrure de silicium sans recuit. En particulier, nous avons mis au point un procédé de fabrication de films de Si_3N_4 d'une épaisseur de 740 nm, sans utilisation de recuit et avec une maitrise de la gestion des contraintes typiquement associées à ce type de matériau pour l'optique non linéaire. Cette approche offre une compatibilité de fabrication technologique avec la photonique sur silicium. Des preuves expérimentales montrent que les micro-résonateurs utilisant de tels films de nitrure de silicium sans recuit sont capables de générer un peigne de fréquence s'étendant sur 1300-2100 nm via une oscillation paramétrique optique basée sur du mélange à quatre ondes. En allant encore plus loin, nous présentons également les travaux d'optimisation technologique portant sur des microrésonateurs en nitrure de silicium recuits avec des guides d'onde à fort confinement modal, qui nous ont permis d'atteindre des pertes de propagation record. Ces résultats ont été rendus possible grâce à une optimisation fine des étapes de gravure des guides d'onde ainsi qu'à l'utilisation de traitements thermiques-chimiques efficaces. Cette nouvelle approche nous a permis de démontrer par ailleurs des sources de peignes de fréquences intégrées sur puce utilisant des résonateurs en nitrure de silicium couplés par aboutement à un laser III-V DFB utilisé comme une pompe. Cette preuve de concept prouve la validité de notre plateforme de circuits photoniques non-linéaires en Si_3N_4 pour la réalisation de peignes de fréquences optiques ultra-compacts à faible consommation.

Mots clés : (130.0130) Optique intégrée; (130.3120) Dispositifs d'optique intégrés; (130.3130) Matériaux pour l'optique intégrée; (190.0190) Optique non linéaire; (270.0270) Optique quantique ; (190.4380) Mélange à quatre ondes.

Publications, Conferences, Patents

Publications

1. **H. El Dirani** *et al.,* “Ultralow-loss tightly-confining Si_3N_4 waveguides and high-Q microresonators,” *Opt. Express*., vol. 27, no. 21, 2019.

2. **H. El Dirani** *et al.,* “Annealing-free Si_3N_4 frequency combs for monolithic integration with Si photonics,” *Appl. Phys. Lett*., vol. 113, no. 8, 2018.

3. **H. El Dirani** *et al.,* “Crack-free silicon-nitride-on-insulator nonlinear circuits for continuum generation in the c-band,” *IEEE Photonics Technol. Lett*., vol. 30, no. 4, pp. 355–358, 2018.

4. P. Demondogin, **H. El Dirani**, *et al.,* "Ultrafast saturable absorption dynamics in hybrid graphene/Si_3N_4 waveguides," *APL Photonics*, vol. 4, no. 7, p. 076102, Jul. 2019.

5. Q. Wilmart, **H. El Dirani** *et al.,* " A versatile silicon-silicon nitride photonics platform for enhanced functionalities and applications, " *Appl. Sci.*, vol. 9, no. 2, p. 255, 2019.

6. M. Bertrand, **H. El Dirani** *et al.,* "A 3-dB Coupler in Slow Wave Substrate Integrated Waveguide Technology," *IEEE Microw. Wirel. Components Lett.*, vol. 29, no. 4, pp. 270–272, Apr. 2019.

Conferences

7. **H. El Dirani** *et al.,* "Crack-free silicon-nitride-on-insulator nonlinear circuits for continuum generation in the C-band," In *IEEE Photonics Conference* (pp. 1-4). *2018*.

8. **H. El Dirani** *et al*., "SiNOI and AlGaAs-on-SOI nonlinear circuits for continuum generation in Si photonics,," in *Proceedings of SPIE - The International Society for Optical Engineering*, 2018, vol. 10535

9. **H. El Dirani** *et al.,* "Optical frequency comb generation using annealing-free Si_3N_4 films for front-end monolithic integration with Si photonics," in *Proceedings of SPIE - The International Society for Optical Engineering*, 2019, vol. 10921, p. 7.

10. **H. El Dirani** *et al., " Nonlinear properties of ultra-low losses hydrogen-annealed submicron silicon waveguides,* ‘’ in Solid State Devices and Materials SSDM 2018, Tokyo, Sept. 2018.

11. **H. El Dirani** *et al.,* " Si_3N_4-based optical frequency comb generation featuring front-end CMOS- and Si-photonics process compatibility," in Solid State Devices and Materials SSDM 2018, Tokyo, Sept. 2018.

12. F. Sabattoli, **H. El Dirani**, et al.,"A Source of Heralded Single Photon Using High Quality Factor Silicon Ring Resonators," ICTON 2019. (Invited).

13. **H. El Dirani** *et al.*, "UV-Light Generation In Silicon Nitride Resonator Pumped At Telecom Wavelengths’’ in IEEE GFP conference, 2019.

14. **H. El Dirani** *et al.*, " Low-Loss Silicon Technology for High-Q Resonator Quantum Sources, " in IEEE GFP conference, 2019.

15. C. Sciancalepore, **H. El Dirani,** Q. Wilmart, C. Socquet-Clerc, L. Adelmini, S. Pauliac, D. Robin-Brosse, S.Olivier, "O-band Echelle grating CWDM demultiplexers on SiNOI exhibiting quasi-absolute thermal insensitiveness," in *Proceedings of SPIE - The International Society for Optical Engineering*, 2018, vol. 10535.

16. C. Sciancalepore, **H. El Dirani** *et al*., "O-band Echelle grating CWDM demultiplexers on SiNOI exhibiting low thermal sensitivity,"in Solid State Devices and Materials SSDM 2017, Sendai, Sept. 2017

17. A. Kamel, **H. El Dirani**, M. Casale, S. Kerdiles, C. Socquet-Clerc, M. Pu, L. Oxenlowe, K. Yvind, C. Siancalepore ‘’Frequency comb generation in crack-free Si-photonics compatible Si_3N_4 microresonator chip’’ in *Conference on Lasers and Electro-Optics*, 2018, p. JTu2A.120.

18. C. Bellegarde**, H. El Dirani** *et al.,* ‘’Technological advances on Si and Si_3N_4 low-loss waveguide platforms for nonlinear and quantum applications‘’ in *spiedigitallibrary.org*, 2019, p. 8.

19. P. Demongodin,, **H. El Dirani** *et al.,* ‘’Saturable absorption of nonlinear graphene coated waveguides, ‘’ in *Conference on Lasers and Electro-Optics*, 2019, p. STh1J.6.

20. A. Kamel, **H. El Dirani**, *et al.,* ‘’Generation of clustered frequency comb via intermodal four-wave mixing in an integrated Si_3N_4 microresonator, ‘’ in *Conference on Lasers and Electro-Optics*, 2019, p. SF3H.2.

21. M.Casale, S. Kerdiles, P. Brianceau, V. Hugues, **H. El Dirani**, and C. Sciancalepore, ‘’ Low-temperature crack-free Si 3 N 4 nonlinear photonic circuits for CMOS-compatible optoelectronic co-integration, ‘’ in *Integrated*

Optics: Devices, Materials, and Technologies XXI, 2017, vol. 10106, p. 1010608..

21. Q. Wilmart, C. Sciancalepore, D.Fowler, **H. El Dirani**, *et al.,* ‘’Enhanced Silicon photonics platform: towards low energy consumption of optical transceivers for datacenter communications .,” in *2018 IEEE CPMT Symposium Japan (ICSJ)*, 2018, pp. 59–62.

22. S. Boust, **H. El Dirani** *et al.*, ‘’ Compact optical frequency comb source with a DFB butt-coupled to a silicon nitride microring,‘’ IEEE microwave photonic conference, 2019.

23. L. Youssef, **H. El Dirani**, *et al*., ‘’ High-yield ultra-low losses Si_3N_4 microresonators for energy-efficient nonlinear photonics, ‘’ OSA FiO 2019.

Patents

24. **H. El Dirani**, C. Sciancalepore, M.Casale,(2018). U.S. Patent Application No. 15/923,571.

25. **H.El Dirani,** M.Casale, and C. Sciancalepore,(2018). U.S. Patent Application No. 15/862,173.

Table of content

CHAPTER 1
INTRODUCTION

1.1. Nonlinear solution for Data traffic needs

The Internet has changed our lives. It is one of the most useful tools human beings have ever invented. In our days, the Internet is the modern source of information. In fact, it is the largest library ever created, and is growing daily. Since people use the Internet for communication, both personnel and professional relationships became faster, more effective and less expensive. Moreover, it has revolutionized communications to the extent that it is now our preferred medium for everyday communication. The Internet is used for many other reasons like entertainment, school, market… In almost everything we do today, we use the Internet.

The rate of the Internet traffic continues to grow (fig. 1). According to Cisco Systems Inc., besides the need of data-traffic for ultra-high definition (UHD or 4K) video demand, between 2017 and 2022, both the mobile data and the internet video surveillance traffic will increase sevenfold, whereas the internet gaming traffic will grow ninefold. In addition, the Internet traffic of the busiest 60 minute period in a day is growing more rapidly than the average Internet traffic. The busy hour internet traffic will increase by a factor of 4.8 between 2017 and 2022 [1]. Furthermore, 28.5 billion networked devices are anticipated by 2022, up from 18 billion in 2017.

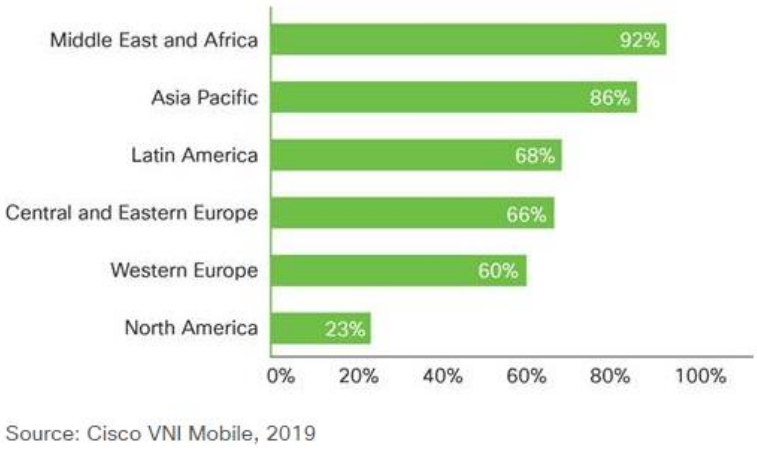

Figure 1-Mobile data traffic growth in 2017 (from[1])

Currently, high speed communication systems consist of discrete directly modulated continuous-wave lasers (DMLs) – such as distributed feedback lasers (DFBs) or vertical-cavity surface-emitting lasers (VCSELs) - operating at different wavelengths where the information is coded using direct on-off keying (OOK) or

external electro-optical modulators for more advanced modulation formats (PAM4, QPSK, CWDM4, SWDM4 etc…) and higher aggregate bandwidths. All the signals are multiplexed into a single fiber to be transported to the receiver. On the receiver side, the signals are de-multiplexed and converted into electrical signals by the use of high-speed high-responsivity photodetectors. This concept of different data streams sent simultaneously over a single optical fiber network is called wavelength-division multiplexing (WDM). Currently, short reach links in data centers are dominated by 850 nm multi-mode vertical-cavity surface-emitting lasers (MM VCSELs) that are feeding multimode fibers because of the low-cost, power-efficient, high fabrication yield of these GaAs-based lasers which can be operated at tens of Gigabits per second[2]. Nevertheless, the modal and chromatic dispersion in the multi-mode fiber, as well as the mode partition noise from MM VCSELs, limit the transmission reach of the data centers nowadays to a few hundred meters at most.

After the successful integration of most optical components on silicon such as III-V-on-Si integrated lasers, high-speed modulators, Ge-on-Si photodiodes, filters and wavelength (de)multiplexers, the Si photonics technology became the promise for a new low-cost scalable technology for optical interconnects. This may replace multi-mode vertical cavity surface emitting lasers (MM VCSELs) specially for large channel counts (4 or more) and long reach links (>300 meters) [2]. Furthermore, silicon photonic devices can be made using existing mature complementary-metal-oxide-semiconductor (CMOS) fabrication techniques, enabling a low-cost fabrication and the co-integration with electronic components onto a single microchip [3].The principle of Si photonics based optical transceiver is presented in fig. 2.

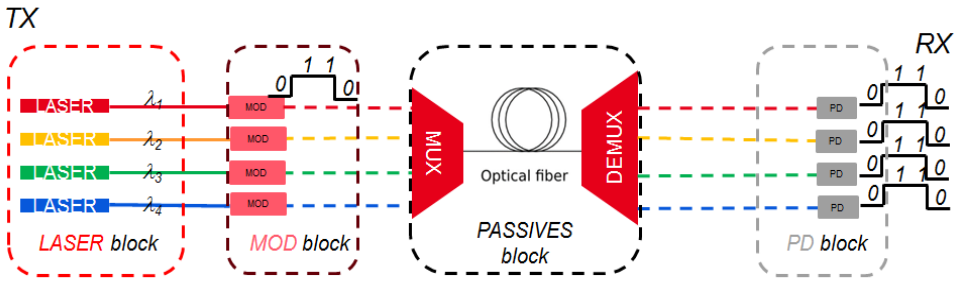

Figure 2-Representation of an optical transceiver. Lasers emit light at different wavelengths. The signals are encoded by the information using modulators on each channel. The multiplexer put together the signals on the same optical fiber. The signals are then demultiplexed in order to be detected by the photodetectors.

In order to accommodate the data-traffic growth with the current technology, one simple solution would consist in adding more and more III-V/Si lasers onto the same chip. However, the footprint of existing operational edge-emitting III-V/Si lasers is non-negligible (> 1 mm). Adding to that, these lasers are intrinsically power-hungry. In fact, 350 mW of electrical power is needed per each laser line, with wall-plug efficiencies (WPEs) of around 13% at 1550 nm [4], while WPEs of more than 35 % are nowadays standard to 850-nm-emitting VCSEL technology.

Is there any other less energy-hungry solution? Are we able to handle the heating issues of a densely-packed area overcrowded with tens or hundreds of lasers operating in parallel? And yet, putting InP/GaAs III-V active regions over a CMOS circuit would clearly heat up the photonic layer above it, reducing the external quantum efficiency and overall the WPE dramatically. The feasibility of such photonics-electronics system co-integration along a more-Moore path would be then at stake in the very end.

One potential solution to overcome the challenges associated with the integration of a dense array of lasers on a chip could be brought by nonlinear optics. Among other phenomena, this allows for the realization of non-classical light sources such as supercontinuum or optical frequency combs, which could provide a dense array of spectral optical lines emitted by a single device.

In 1960, and for the first time, strong and coherent laser optical fields became available [5]. One year later, the nonlinear optics field was born with the observation of second harmonic generation (SHG) due to the high field strength [6] launched onto a bulk piece of crystalline quartz. In the following years and decades, a wide variety of nonlinear phenomena arising from the interaction of intense optical fields and suitable materials have been reported, such as Raman lasers in nitrobenzene [7], [8] and third harmonic generation [9], [10]. More importantly, the combination of nonlinear optics and resonators expanded the number of applications, with the advent of optical parametric oscillators and, even more recently, optical frequency combs.

Optical frequency comb (OFC) generation was demonstrated for the first time in 2008, in crystalline resonators made of calcium fluoride (CaF_2) polished using a

turning lathe by hand [11], [12]. OFCs have been also demonstrated in crystalline resonators made of magnesium fluoride (MgF_2) that can be fabricated similarly to calcium fluoride resonators with a turning and manual polishing. Nevertheless, MgF_2 is more advantageous than CaF_2 since the thermo-refractive and the thermos-elastic effects in magnesium fluoride have the same sign, which is important for the thermal self-locking of a pump laser to the resonator, providing a long-term time-stable coherent comb generation [12]. OFC generation has been demonstrated for the first time on a silicon wafer in fused silica toroidal microcavity using a specific under-etching process to avoid leakage into the silicon substrate underneath [13]. In addition, light is coupled in these resonators by approaching mechanically a tapered fiber which is mounted in a bracket sitting on a piezo translation stage assuring the fine positioning of the fiber [13]. While this technique can be carried out in a laboratory, it cannot be achieved on-chip using a CMOS compatible monolithic approach.

For telecom applications, the development of photonic integrated circuits that require ultrahigh bandwidth, nonlinear optical signal processing has been dominated by the use of silicon on insulator (SOI) photonics and the condition to be fully CMOS compatible is widely accepted [14]. In particular when signals are dispatched on a chip at several wavelengths simultaneously, as in the case of on-chip wavelength division multiplexing, a CMOS compatible multi-wavelength optical source is critical [15].

However, the key to increase nonlinear phenomena are light confinement in space and time. This imposes small cross-section waveguides with low losses (or resonators with high quality factors), a high material nonlinear response and the capability to engineer the dispersion (see chapter 2). Even though crystalline silicon (as in SOI waveguides) meets most of these criteria, the low value of its electronic bandgap (1.12 eV) causes nonlinear absorption at high pump power, which has thus far precluded the generation of frequency combs in silicon resonators pumped at telecoms wavelengths.

Since 2010, silicon-nitride-on-insulator (SiNOI) has imposed itself as an attractive chip-based platform for the generation of wideband optical frequency combs (fig. 3)

pumped at telecom wavelengths, because of its relatively high nonlinearity (× 10 that of silica and larger than that of highly nonlinear Hydex glass [16]) as well as the absence of two-photon absorption and free carrier generation that plague crystalline silicon. In the meanwhile, silicon photonic integrated circuits (Si-PICs) have demonstrated increasing maturity levels for a wide range of optical functions such as III-V-on-Si integrated lasers [4] , high-speed modulators [17], Ge-on-Si photodiodes [18], as well as filters and wavelength (de)multiplexers [19], thus continuously highlighting the potential of silicon optoelectronics integration with cost-effective complementary metal-oxide-semiconductor (CMOS) technology [20], [21]. In this context, the monolithic integration of Kerr-based frequency combs with Si photonics and CMOS micro-nano-electronic nodes holds the promise for on-chip high-capacity transmitters that would benefit from the maturity and low cost of CMOS manufacturing and scalability.

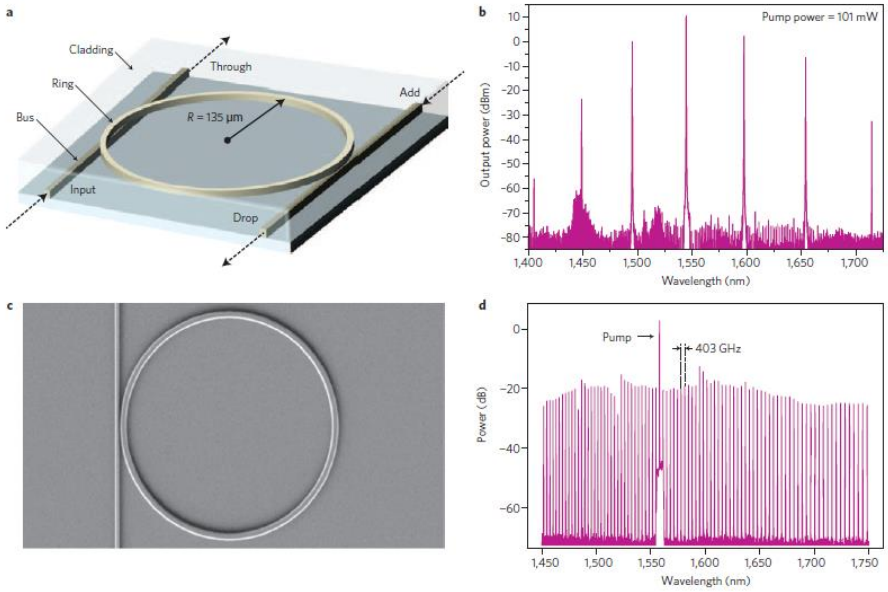

Figure 3-Integrated optical-parametric-oscillator multiple-wavelength sources in Hydex and SiN ring resonators. a, Hydex four-port with a Q-factor of 1.2×10^6 and a diameter of 270 µm. b, Output spectrum of an Hydex hyper-parametric oscillator for a pump power of 101 mW injected on resonance at 1,544.15 nm. c, SEM image of a SiN microring resonator (58 µm radius, Q = 500,000 coupled to a bus waveguide. d, Output spectrum of a 58-µm-radius SiN ring-resonator optical parametric oscillator with a single pump wavelength tuned to resonance at 1,557.8 nm. (From [16])

The realization of relatively thick (> 700 nm) stoichiometric Si_3N_4 films, as required by microring frequency combs, which imply both a tight confinement of light and anomalous group velocity dispersion (GVD), remains challenging. In particular, all

prior works strictly made use of long high-temperature annealing (~1200 °C for at least 3 h) of the deposited silicon nitride film [22]–[25]. This extreme annealing step has been accounted for by the need to densify the silicon nitride film through driving out excess hydrogen and break N-H bonds, so as to get closer to a stoichiometric Si_3N_4 film and reduce the material absorption loss in the C-band. However, this annealing induces thermal stress that eventually leads to cracks during the device processing unless sophisticated pre-patterning strategies are adopted prior to the film deposition [16], [23]. Yet, in the perspective of nonlinear optics-silicon optoelectronics co-integration, these extreme annealing temperatures would severely degrade the front-end-of-the-line (FEOL) silicon optoelectronic circuits underneath. Specifically, doped optical circuits would be unacceptably affected by the undesirable dopant diffusion in junction-based Si modulators and by the hetero-interface degradation of Ge-on-Si photodetectors.

As an alternative, optical parametric oscillation has been demonstrated by using the proprietary composition of Hydex waveguides in 2013 [16]. However, the nonlinear parameter $\boldsymbol{\gamma}$ of Hydex is six times lower than that of silicon nitride, thus increasing the required power for frequency comb generation, hence the risk of waveguide optical damage. Comb generation has also been demonstrated in 2018 using deuterated silicon nitride (SiN:D) deposited at 300 °C [26]. However, although being a CMOS-compatible processing building block, it is worth to point out that deuterated silicon nitride can be exclusively used during the back-end-of-the-line (BEOL) fabrication, thus preventing a straightforward monolithic integration with both silicon photonics and sub-100 nm standard CMOS electronics circuitries during a collective FEOL processing [27]. Furthermore, this material has a relatively strong thermal shift that occurs from the larger residual hydrogen-related absorption coefficient (when compared to purely stoichiometric Si_3N_4 films) making it difficult to stabilize the comb in the soliton state as described in [26]. In addition, for similar resonance quality factors, deuterated silicon nitride microresonators require higher threshold powers for comb generation than stoichiometric Si_3N_4, which indicates a lower nonlinear index of SiN:D and increases, as for the Hydex, the risk of waveguide optical damage.

Ultimately, in this thesis, we present a key step toward Kerr-based broadband sources featuring full process compatibility with Si optoelectronic circuits on CMOS-lines. This holds the potential for long-lasting impact and is important to the broad photonics community due to the unique integration prospects offered by our fabrication approach.

More specifically, in this thesis:

- **we report a novel deposition technique for growing relatively thick stoichiometric Si_3N_4 films** ensuring tight optical mode confinement and anomalous group velocity dispersion that are necessary for frequency comb generation;
- **our process alleviates the need for sophisticated substrate pre-patterning** strategies that have been developed worldwide to avoid the formation of cracks upon device fabrication within thick silicon-nitride films;
- **our process meets the thermal processing constraints** that support the monolithic co-integration of our broadband comb source CMOS with silicon optoelectronics;
- we validate the full nonlinear potential of our annealing-free and crack-free approach through the demonstration of a broadband frequency comb source at telecom wavelengths (730 nm in bandwidth, 1340 nm – 2070 nm).

Moreover, we present record low losses of high confinement silicon nitride waveguides using annealing treatments and on-chip integrated Kerr frequency comb sources based on the butt coupling between a III-V DFB laser and a silicon nitride micro-resonator.

1.1. Manuscript organization

After this introduction, we present, in the second chapter, a brief theoretical description of the nonlinear processes that are associated with optical frequency comb generation. We present the main key parameters that determine the efficiency of nonlinear processes in chip-based platforms, as well as an overview of different nonlinear material platforms, in particular CMOS compatible ones, including Si_3N_4, our chosen material.

The third chapter presents the underlying theory of light confinement in a ring resonator as well as our design work for achieving optical frequency combs in Si_3N_4 microring resonators. More precisely, the linear parameters describing the response of microrings are first introduced, such as the resonance condition, the condition to get a critically coupled resonator, the quality factor, the field enhancement and free spectral range. We then present how to dimension our Si_3N_4waveguides to obtain anomalous dispersion, which is the condition to get four wave mixing based frequency combs. Finally, we also discuss the required waveguide dimensions to get phase matching for high-order harmonic generation in this material platform.

In the chapter 4, we present the fabrication techniques and methods that have been developed to obtain annealing-free and crack-free silicon nitride ring resonators with sufficiently high quality factors and thick film to generate frequency combs.

In the chapter 5, we present the characterization work of our silicon nitride devices, in both the linear regime (waveguide propagation losses and ring quality factors) and the nonlinear regime at telecom wavelengths. We discuss how our material nonlinear index was first measured via self-phase modulation and four wave mixing experiments, and present our experimental results on frequency comb and high-order harmonic generation under relatively high pump power.

The chapter 6 finally presents our recent optimization work related to Si_3N_4 optical devices. First, we were able to achieve record low losses for annealed silicon nitride waveguides providing a tight light confinement. This was enabled via a carefully tailored patterning etching process as well as some optimized post-process annealing treatment. We present our improved nonlinear results using this novel approach: it allowed us to demonstrate on-chip integrated Kerr frequency comb sources using silicon nitride resonators that were butt-coupled to a III-V DFB laser used as a pump source. This proof of concept proves the validity of our approach for realizing fully packaged compact optical frequency combs.

CHAPTER 2
NONLINEAR OPTICS THEORY AND RELATED MATERIAL PLATFORMS

In a homogeneous, linear and isotropic dielectric medium, the polarization is aligned with and proportional to the electric field, while oscillating at the same frequency. If light intensity becomes very high, though, light-matter interaction is perturbed and deviates from this simple picture. In this case, the polarization field also depends on the electric field intensity (square of the electric field). In fact, higher order terms of polarization are included into Maxwell's equations giving rise to nonlinearities and this results in several new and interesting phenomena such as second-harmonic generation (SHG), third-harmonic generation (THG), three- and four-wave mixing, optical frequency comb generation and self-phase modulation (SPM). In this chapter we provide a qualitative description of the nonlinear processes as well as an overview of different nonlinear chip-based material platforms that have been used in this context. More precisely, we introduce the specific properties of waveguides that are relevant in the context of integrated nonlinear optics, such as dispersion, the nonlinear index and the two photon absorption parameter.

2.1.Wave Equation for Nonlinear Optics

The modification of the optical properties of a material by the presence of sufficiently intense light gives rise to nonlinear optics phenomena. The nonlinear effects that are observed in waveguides can be built up from the wave equation taking into account the higher order terms of the polarization expressed as a function of the electric field. In this part we will explain how the wave equation can be derived from Maxwell's equations that describe the propagation of electromagnetic fields in dielectric waveguides.

In the macroscopic case, Maxwell's equations are formulated as follows:

$$\nabla . \boldsymbol{D} = \rho \tag{2.1.1}$$

$$\nabla . \boldsymbol{B} = 0 \tag{2.1.2}$$

$$\nabla \times \boldsymbol{E} = -\frac{\partial \boldsymbol{B}}{\partial t} \tag{2.1.3}$$

$$\nabla \times \boldsymbol{H} = \boldsymbol{J} + \frac{\partial \boldsymbol{D}}{\partial t} \tag{2.1.4}$$

where D is the electric flux density, ρ is the charge density, B is the magnetic flux density, E is the electric field, H is the magnetic field and J is the current density. We will work with these equations in dielectric waveguides containing neither free charges nor free currents so that ρ and J are zero.

The field amplitudes are related to the flux densities by the constitutive equations:

$$\boldsymbol{D} = \varepsilon_0 \boldsymbol{E} + \boldsymbol{P} \tag{2.1.5}$$

$$\boldsymbol{B} = \mu_0 \boldsymbol{H} + \boldsymbol{M} \tag{2.1.6}$$

where $\varepsilon_0 = 8.85 \times 10^{-12} \mathrm{F.m^{-1}}$ is the permittivity of free-space and $\mu_0 = 4\pi \times 10^{-7} \mathrm{H.m^{-1}}$ is the vacuum permeability. The dielectric we are working with is nonmagnetic so that the magnetic polarization, $\boldsymbol{M}$, is zero .

The optical nonlinearity can be often described by expressing the polarization $\boldsymbol{P}$ as a Taylor series with respect to the field strength E as:

$$\begin{aligned} \boldsymbol{P} &= \varepsilon_0 [\chi^{(1)} \boldsymbol{E} + \chi^{(2)} \boldsymbol{E^2} + \chi^{(3)} \boldsymbol{E^3} + \cdots] \\ &\equiv \boldsymbol{P}^{(1)} + \boldsymbol{P}^{(2.1)} + \boldsymbol{P}^{(3)} + \cdots. \end{aligned} \tag{2.1.7}$$

where $\chi^{(1)}$ is the linear optical susceptibility and is related to the refractive index by the relation $\chi^{(1)} = n^2 - 1$. $\chi^{(2)}$ and $\chi^{(3)}$ are known as the second- and third-order nonlinear optical susceptibilities, respectively. In the case of linear optics the polarization depends linearly on the electric field and can be described by the relationship:

$$\boldsymbol{P}^{(1)} = \varepsilon_0 \chi^{(1)} \boldsymbol{E} \tag{2.1.8}$$

We refer to $\mathrm{P}^{(2)} = \varepsilon_0 \chi^{(2)} \mathrm{E}^2$ as the second-order nonlinear polarization and to $\mathrm{P}^{(3)} = \varepsilon_0 \chi^{(3)} \boldsymbol{E^3}$ as the third-order nonlinear polarization. In centrosymmetric materials (Si, Ge, amorphous glass…) $\chi^{(2)}$ is zero and $\chi^{(3)}$dominates the nonlinear properties. We will see later in this chapter that the physical processes resulting from the second-order polarization are distinct from those occurring as a result of the third-order polarization. Even though in amorphous materials $\chi^{(2)}$ is a priori null, an effective $\chi^{(2)}$ can arise in waveguides (or more generally in patterned geometries) at the interface between the core and the cladding or at the waveguide surface.

In order to derive the wave equation, we take the curl of the Maxwell's equation (2.1.3), interchange the order of time and space derivative on the right-hand side of the resulting equation, and use 2.1.4 and 2.1.6 to replace $\nabla \times \boldsymbol{B}$ by $\mu_0(\partial \boldsymbol{D}/\partial t)$ to obtain the equation:

$$\nabla \times \nabla \times \boldsymbol{E} + \mu_0 \frac{\partial^2 \boldsymbol{D}}{\partial^2 t} = 0 \tag{2.1.9}$$

Using the equation 2.1.5 to eliminate $\boldsymbol{D}$ from the last equation we obtain the expression of the most general form of the wave equation in nonlinear optics:

$$\nabla \times \nabla \times \boldsymbol{E} + \mu_0 \varepsilon_0 \frac{\partial^2 \boldsymbol{E}}{\partial^2 t} = -\mu_0 \frac{\partial^2 \boldsymbol{P}}{\partial^2 t} \tag{2.1.10}$$

Expressing the polarization term in the latter equation as the sum of a linear ($\boldsymbol{P}^{(1)} = \varepsilon_0 \chi^{(1)} \boldsymbol{E}$) and a nonlinear part ($\boldsymbol{P}^{NL} = \boldsymbol{P}^{(2)} + \boldsymbol{P}^{(3)} \ldots$) gives the following expression:

$$\nabla \times \nabla \times \boldsymbol{E} + \mu_0 \varepsilon_0 (\chi^{(1)} + 1) \frac{\partial^2 \boldsymbol{E}}{\partial^2 t} = -\mu_0 \frac{\partial^2 \boldsymbol{P^{NL}}}{\partial^2 t} \tag{2.1.11}$$

The curl of a curl of $\boldsymbol{E}$ ($\nabla \times \nabla \times \boldsymbol{E}$) in the equation (2.1.11) is equal to the gradient of the divergence of the electric field ($(\nabla(\nabla . \boldsymbol{E}))$ minus the Laplacien vector ($\nabla^2 \boldsymbol{E}$). In nonlinear optics, using the equation 2.1.1, the divergence of the electric field can usually be dropped [28]. In addition using $\chi^{(1)} + 1 = n^2$ (material index) and $c = 1/\sqrt{\mu_0 \varepsilon_0}$ (speed of light in vacuum) the wave equation can be expressed as:

$$\nabla^2 \boldsymbol{E} - \frac{n^2}{c^2} \frac{\partial^2 \boldsymbol{E}}{\partial^2 t} = -\frac{1}{\varepsilon_0 c^2} \frac{\partial^2 \boldsymbol{P^{NL}}}{\partial^2 t} \tag{2.1.12}$$

In the absence of the nonlinear polarization, the solutions of the equation 2.1.12 are free waves propagating with the phase velocity equal to c/n.

In equation (2.1.12), the nonlinear polarization can be interpreted as a radiation source, which might contain new frequencies that were not part of the incident field.

In a dispersive medium where the refractive index does change with frequency, each frequency component of the field must be considered separately. The electric field and polarization can be expressed as the sum of the various frequency components:

$$\boldsymbol{E}(\boldsymbol{r},\boldsymbol{t}) = \sum_{\boldsymbol{n}} \boldsymbol{E_n}(\boldsymbol{r},\boldsymbol{t}) \quad (2.1.13a)$$

$$\boldsymbol{P^{NL}}(\boldsymbol{r},\boldsymbol{t}) = \sum_{\boldsymbol{n}} \boldsymbol{P_n^{NL}}(\boldsymbol{r},\boldsymbol{t}) \quad (2.1.13b)$$

Only positive field frequencies are to be taken into account, and each frequency component of the electromagnetic field can be represented in terms of its complex amplitude $\widetilde{\boldsymbol{E}}_{\boldsymbol{n}}(\boldsymbol{r})$ as:

$$\boldsymbol{E_n}(\boldsymbol{r},\boldsymbol{t}) = \widetilde{\boldsymbol{E}}_{\boldsymbol{n}}(\boldsymbol{r})\boldsymbol{e}^{-\boldsymbol{j}\boldsymbol{\omega_n}\boldsymbol{t}} + \boldsymbol{c.c.}, \quad (2.1.14a)$$

$$\boldsymbol{P_n^{NL}}(\boldsymbol{r},\boldsymbol{t}) = \widetilde{\boldsymbol{P}}_{\boldsymbol{n}}^{\boldsymbol{NL}}(\boldsymbol{r})\boldsymbol{e}^{-\boldsymbol{j}\boldsymbol{\omega_n}\boldsymbol{t}} + \boldsymbol{c.c.}, \quad (2.1.14b)$$

If we introduce the equations 2.1.14 into equation 2.1.12, we obtain as many wave equations as the number of frequencies, i.e. for each frequency component $\boldsymbol{\omega_n}$ of the field:

$$\nabla^2\widetilde{\boldsymbol{E}}_{\boldsymbol{n}}(\boldsymbol{r}) - n^2(\omega)\frac{{\omega_n}^2}{c^2}\widetilde{\boldsymbol{E}}_{\boldsymbol{n}}(\boldsymbol{r}) = -\frac{{\omega_n}^2}{\varepsilon_0 c^2}\widetilde{\boldsymbol{P}}_{\boldsymbol{n}}^{\boldsymbol{NL}}(\boldsymbol{r}) \quad (2.1.15)$$

Note that the different frequency components are coupled via the nonlinear polarization term on the right hand side, which accounts for the interactions between the different frequencies. Using this equation we will explain the different nonlinear phenomena that can be observed.

2.2. Propagation constant and effective index

Before analyzing the consequences of the nonlinear response of matter, we first present some notions of guided wave optics in the linear regime. Although channel waveguide geometries are studied in this PhD work, the theoretical description is restricted to planar waveguides, since the underlying physics is very similar.

While propagating in a direction, light recovers its initial state after travelling one length of lambda. Consequently, per unit length there will be 1/ lambda cycles. The angular frequency is the number of cycles per second (frequency) multiplied by 2π. Likewise, the wavenumber is the equivalent of the angular frequency, but with respect to the distance variable. Leading to the wavenumber:

$$k = \frac{2\pi}{\lambda} \tag{2.2.1}$$

In space, the light waves propagate at a speed of $c = 299{,}792{,}458\ m/s$. In a bulk material, the latter is divided by the refractive index. Thus, the number of cycles per length unit is multiplied by the refractive index and the propagation constant in the bulk material is:

$$\beta = \frac{2\pi}{\lambda} n \tag{2.2.2}$$

In integrated photonics, light is guided in a core of higher index (n_h) material surrounded by a lower index (n_l) cladding by total internal reflection when the angle of incidence is greater than the critical angle of Snell's law:

$$n_l sin\theta_l = n_h sin\theta_h \tag{2.2.3}$$

From Snell's law, we can deduce that the critical angle is:

$$\theta_c = sin^{-1}\frac{n_l}{n_h} \tag{2.2.4}$$

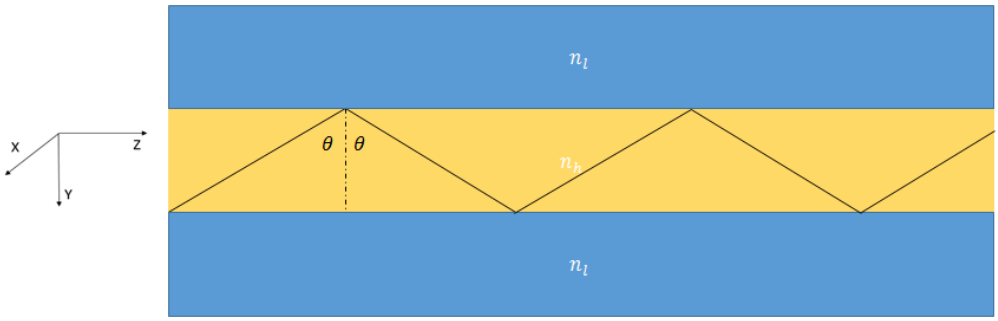

Figure 4- An illustration of geometric optics with a higher index material, $\boldsymbol{n_h}$, surrounded by a lower index material $\boldsymbol{n_l}$

The case studied in this thesis corresponds to a high index material surrounded on both sides by the same lower index material as shown in Fig. 4. Due to the reflections at the core/ cladding waveguide interfaces, the distance traveled by light in the Z direction is the real distance traveled (the black line) multiplied by $sin\theta$. We have to take this into account to present analytically the electric field by multiplying the index of the material by $sin\theta$. In fact, we can define the effective index and the propagation constant in a waveguide as follows:

$$n_{eff} = n_h sin\theta \quad (2.2.5)$$

$$\beta = k_0 n_h sin\theta \quad (2.2.6)$$

2.3. Dispersion

In integrated photonic circuits associated with a given plane, we define the linearly polarized states TE (Transverse Electric) and TM (Transverse Magnetic) as:

-TE: Electric field parallel to the circuit plane,

-TM: Magnetic field parallel to the circuit plane.

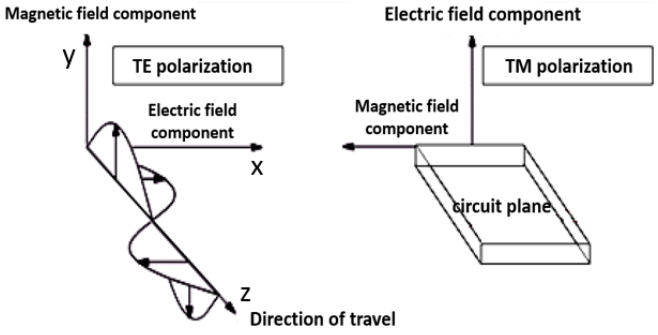

Figure 5- Polarization states

In the TE mode, if the propagation direction is parallel to the Z axis as shown in Fig. 5 and the electric field is parallel to the X axis, the spatial component of the electric field complex amplitude from the equation 2.1.14a is given by:

$$\tilde{E}(r) = \tilde{E}(y,z) = E_0 E_x(y) e^{-j\beta z} \quad (2.3.1)$$

Introducing the equation 2.3.1 in the wave equation without taking into account the nonlinear polarization, we obtain the following equation:

$$\frac{\partial^2 E_x}{\partial y^2} + \left({k_0}^2 n_i^2 - \beta^2\right) E_x = 0 \quad (2.3.2)$$

where n_i is the refractive index of the core or the cladding. Supposing the core region from figure 4 extends from ±d, the solutions of the equation are as follow:

$$E_x(y) = \begin{cases} A_l e^{-(y-d)\sqrt{\beta^2 - {k_0}^2 n_l^2}} & \text{for } y>d \\ A_h cos\left(y\sqrt{{k_0}^2 n_h^2 - \beta^2}\right) or\ A_3 sin\left(y\sqrt{{k_0}^2 n_h^2 - \beta^2}\right) & \text{for } -d < y < d \\ A_l e^{(y+d)\sqrt{\beta^2 - {k_0}^2 n_l^2}} & \text{for } y<-d \end{cases} \quad (2.3.3)$$

As mentioned before, the velocity of the light propagating in a dielectric is the speed in free-space divided by the refractive index. This is the velocity at which the phase of any frequency component of the wave travels. In a bulk medium, this value is defined as:

$$v_p = \frac{\omega}{k} \quad (2.3.4)$$

However, when light is confined in a waveguide and propagates in a given direction, the phase velocity is modified as per:

$$v_p = \frac{\omega}{\beta} = \frac{c}{n_{eff}}, \quad (2.3.5)$$

where the wave number is substituted by the propagation constant.

Since the propagation constant (β) is a function of frequency, the phase velocity changes as well for different wavelengths. If we look at an optical pulse with multiple frequencies, we can define the group velocity v_g as the speed at which the pulse envelope (or energy) travels:

$$v_g = \frac{\partial \omega}{\partial \beta} \quad (2.3.6)$$

Using the relation $\beta/_{k_0} = n_{eff}$, we can rewrite the group velocity as follow:

$$\frac{1}{v_g} = \frac{1}{c}\left(n_{eff}(\omega) + \omega\frac{\partial n_{eff}}{\partial \omega}\right) = \frac{1}{c}\left(n_{eff}(\lambda) - \lambda\frac{\partial n_{eff}}{\partial \lambda}\right) = \frac{n_g}{c} \quad (2.3.7)$$

where n_g is the group index. We can realize that the group index is approximately the effective index with a slight adjustment to account for how the effective index changes with frequency. The effective index variation with frequency is defined by the second-order dispersion via:

$$\beta_2 = \frac{\partial^2 \beta}{\partial \omega^2} = \frac{1}{c}\left(2\frac{\partial n_{eff}}{\partial \omega} + \omega \frac{\partial^2 n_{eff}}{\partial \omega^2}\right) \quad (2.3.8)$$

This parameter is referred to as the group velocity dispersion $[s^2.m^{-1}]$. It is responsible for different phenomena such as pulse temporal broadening or, when combined with nonlinearity or chirped pulses, pulse compression. The group velocity dispersion is related to the group index as follow:

$$\beta_2 = \frac{1}{c}\frac{\partial n_g}{\partial \omega} \quad (2.3.9)$$

The change of $1/v_g$ with respect to wavelength is called the dispersion parameter $[ps.nm^{-1}.km^{-1}]$ and is defined as:

$$D = \frac{1}{c}\frac{\partial n_g}{\partial \lambda} = -\frac{\lambda}{c}\frac{\partial^2 n_{eff}}{\partial \lambda^2} \quad (2.3.10)$$

The dispersion parameter and the group velocity dispersion are thus related to one another through:

$$D = -\frac{2\pi c}{\lambda^2}.\beta_2 \quad (2.3.11)$$

These parameters are very important in waveguide based nonlinear optics, due to the phase-matching requirements of the nonlinear processes, especially those involving waves at non-degenerate frequencies, as will be described in section 2.4.

2.4. Manifestation of the Nonlinear Optical response

We next describe the main phenomena associated with nonlinear optical interactions at 1550 nm using coupled amplitude equations derived from the nonlinear optical wave equation presented in section 2.1.

Four-wave-mixing

In this section, we consider continuous-wave degenerate-four-wave-mixing where two pump-photons at ω_p are converted to two photons that are symmetrically detuned from the pump frequency $(2\omega_p - \omega_i = \omega_s)$ as presented in fig. 6. This process is a manifestation of the third order nonlinear susceptibility $\chi^{(3)}$. We take

this particular process as an example to introduce the main characteristics of nonlinear waveguides that can be exploited to increase the efficiency of nonlinear processes in general. In addition, four-wave mixing remains essential in the generation of frequency combs, which has been the main focus of this PhD.

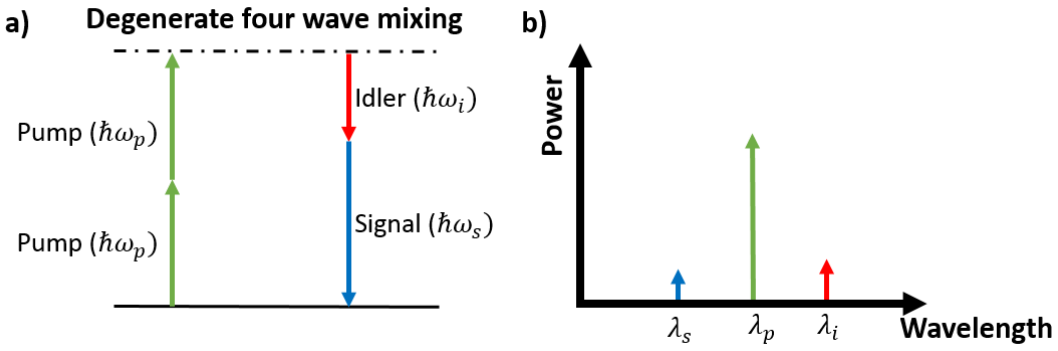

Figure 6- Degenerate four wave mixing. (a) Energy level diagram of Degenerate four-wave mixing and (b) the corresponding sideband lines generated.

The process involves four waves, as the name suggests, which are usually designated as two pump waves, a signal and an idler wave, respectively. In case of multiple frequency fields, the equation 2.1.14b takes the following form:

$$\boldsymbol{P(r,t) = \sum_n \tilde{P}_n(r) e^{j\omega_n t} + C^{te}} \quad (2.4.1)$$

$$\tilde{P}_n(\boldsymbol{r}) = \chi^{(1)} \tilde{\boldsymbol{E}}_n(\boldsymbol{r}) + \tilde{P}_n^{NL}(\boldsymbol{r}) \quad (2.4.2)$$

$$\tilde{P}_n^{NL}(r) = \sum_{i,j,k} \epsilon_0 \chi^{(3)}(\boldsymbol{\omega_n = \omega_i + \omega_j + \omega_k : \omega_i, \omega_j, \omega_k}) \tilde{\boldsymbol{E}}_i(\boldsymbol{r}) \tilde{\boldsymbol{E}}_j(\boldsymbol{r}) \tilde{\boldsymbol{E}}_k(\boldsymbol{r}) \quad (2.4.3)$$

We focus here on the third-order nonlinearity, while neglecting the second order non linearity ($\chi^{(2)}$), because the material studied in our case (Si_3N_4) is amorphous.

The subscripts $\boldsymbol{i}$, $\boldsymbol{j}$ and $\boldsymbol{k}$ in the equation 2.4.3 can represent any frequency component of the field such that their sum (or difference) is equal to the frequency $\boldsymbol{\omega_n}$. This originates from the photon energy conservation, which intrinsically results from the elastic characteristics of nonlinear Kerr processes (unlike Raman or Brillouin interactions for instance).

In the case of multiple fields interacting, the nonlinear polarization term oscillating at the field frequency $\boldsymbol{\omega_n}$, can be rewritten in the following form:

$$P_n^{NL}(r) = P_n(z) e^{j(\Delta\beta_n z - \omega_n t)} \quad (2.4.4)$$

where $\Delta\beta_n$ arises from equation 2.4.3 as the sum or difference of the propagation constants of the interacting waves. From equation 2.4.3, we can find $\boldsymbol{P_n(z)}$ and introduce it in the nonlinear wave equation (2.1.15). Therefrom, under the slowly varying envelope approximation, the coupled amplitude equations take the general form [28]:

$$\frac{\partial E_n}{\partial z}(r) = \frac{j2\pi\boldsymbol{\omega_n}}{nc} P_n^{NL}(r) = \frac{j2\pi\boldsymbol{\omega_n}}{nc} \boldsymbol{P_n(z)} \boldsymbol{e^{j(\Delta\beta_n z - \omega_n t)}} \tag{2.4.5}$$

As mentioned above, due to energy conservation, the idler wave frequency $\boldsymbol{\omega_i}$, is related to the pump and signal frequencies via $\omega_{\mathrm{i}} = 2\omega_p - \omega_s$. Eventually, considering that the generated waves have a low power and that the pump is strong and remains undepleted, the coupled amplitude equations can be written as follows [29], [30]:

$$\frac{\partial E_{\mathrm{p}}}{\partial z} = -\frac{\alpha_{\mathrm{p}}}{2} E_{\mathrm{p}} + j\gamma \left|E_{\mathrm{p}}\right|^2 E_{\mathrm{p}} \tag{2.4.6}$$

$$\frac{\partial E_{\mathrm{s}}}{\partial z} = -\frac{\alpha_{\mathrm{s}}}{2} E_{\mathrm{s}} + 2j\gamma \left|E_{\mathrm{p}}\right|^2 E_{\mathrm{s}} + \gamma E_{\mathrm{p}}^2 E_{\mathrm{i}}^* e^{-j\Delta\beta z} \tag{2.4.7}$$

$$\frac{\partial E_{\mathrm{i}}}{\partial z} = -\frac{\alpha_{\mathrm{i}}}{2} E_{\mathrm{i}} + 2j\gamma \left|E_{\mathrm{p}}\right|^2 E_{\mathrm{i}} + \gamma E_{\mathrm{p}}^2 E_{\mathrm{s}}^* e^{-j\Delta\beta z} \tag{2.4.8}$$

In these equations, we introduced additional terms (the first terms on the right hand side), which account for the linear loss at frequency $\boldsymbol{\omega_n}$ (α_{n} is the propagation loss per unit of distance along the waveguide). Note that the Si_3N_4 material does not suffer from nonlinear losses (like two-photon absorption or free carrier absorption) at the frequency of interest (1.55 μm), so that the sole loss contributions in equations (2.4.6) to (2.4.7) are these linear terms. In these equations, we also introduced the nonlinear parameter γ defined as:

$$\gamma = \frac{\omega n_2}{cA_{eff}} \tag{2.4.9}$$

where n_2 is the nonlinear index of the material and A_{eff} is the effective modal area. The nonlinear parameter [/W/m] effectively describes the amount of nonlinearity of a given nonlinear waveguide (per unit of peak power and per unit of propagation distance). This metric allows us to compare various guided-wave material platforms

using different materials and providing different degrees of light confinement. In the amplitude coupled equations we neglected the difference of A_{eff} and the dispersion of n_2 between the pump, signal and idler and therefore γ is the same for the different fields. The second term of the equation 2.4.6 represents self-phase modulation, whereas the second terms of the equations 2.4.7 and 2.4.8 feature the cross phase modulation of the pump on the signal and the idler, respectively.

The parametric gain and the wavelength conversion that are more specifically related to the degenerate four-wave mixing process are determined by the third-term in equations 2.4.7 and 2.4.8. This term depends on the linear phase-mismatch $\Delta\beta$ between the different waves involved in the process and defined here as:

$$\Delta\beta = 2\beta_p - \beta_s - \beta_i \tag{2.4.10}$$

This term appears when the term $P_{\boldsymbol{n}}(\boldsymbol{z})$ from equation 2.4.4 is replaced in the coupled amplitude equations. However, taking into account cross phase modulation and self-phase modulation, the final net phase-mismatch can eventually be expressed as [31], [32]:

$$\kappa = 2\gamma P_p - \Delta\beta \tag{2.4.11}$$

It can be easily shown that nonlinear interaction processes are much more efficient when the phase matching condition is satisfied, i.e. for four-wave mixing processes, when $\kappa = 0$. Under this condition, the signal can be amplified exponentially along the propagation distance across the waveguide, while a maximum conversion efficiency between the signal to idler is achieved. The four-wave mixing conversion efficiency is then given by:

$$\eta = \frac{P_{idler}}{P_{signal}} = (\gamma P_p L_{eff})^2 \tag{2.4.12}$$

where P_p is the coupled peak pump power, γ is the nonlinear waveguide parameter from equation 2.4.9 and L_{eff} is the effective length given by

$$L_{eff} = \frac{1-e^{-\alpha.L}}{\alpha} \tag{2.4.13}$$

Depending on the linear propagation loss α (considered to be the same for all three wavelengths), L_{eff} converges towards $L_{max}=1/\alpha$ as a function of the waveguide length (L). This shows the need for decreasing the linear loss, in order to achieve efficient nonlinear processes.

From equation 2.4.11, we realize that the phase matching condition is dependent on both the pump power and the propagation constant of each wave involved. To get the net phase matching κ equal to zero, the linear phase mismatch (Δβ) has to be positive and compensate for the nonlinear phase mismatch ($2\gamma P_p$). This can only be satisfied when the derivative of the function β(ω) is decreasing for increasing frequency (see fig 7). This means that the group velocity dispersion (β_2) has to be negative at the pump frequency.

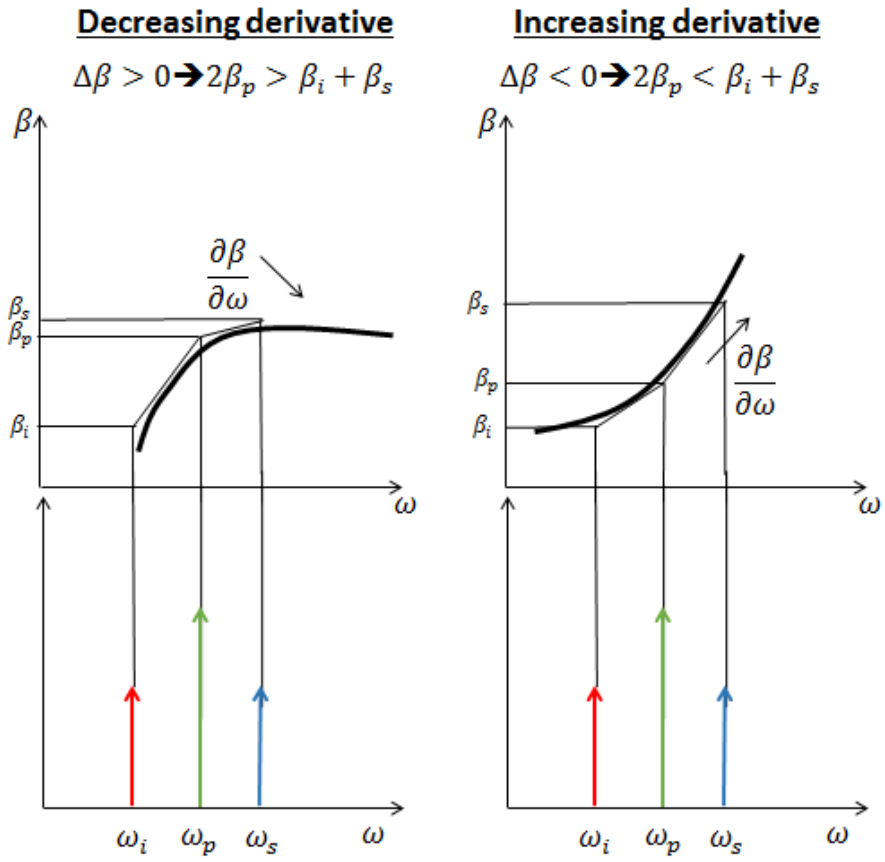

Figure 7- The difference between decreasing derivative and increasing derivative

When the derivative of the function is decreasing ($\beta_2 < 0$), the dispersion is called anomalous and the dispersion parameter from equation 2.3.10 is positive.

This example illustrates how guided-wave optics can be used to enhance nonlinear processes, through providing long interaction distance between the waves (thanks to the use of low-loss waveguides) and through allowing phase matching by engineering the waveguide dispersion. Practically, anomalous dispersion (hence phase matching) can be achieved by adjusting the waveguide cross-section, i.e. for specific width and thickness of the waveguide made of a given material (with a characteristic material dispersion). An accurate control of waveguide dimensions is required, making it advantageous to use silicon photonic compatible materials and the associated mature electronic manufacturing.

Frequency comb generation

The nonlinear interaction between light and the material can be enhanced using a resonator. The resonator used in our studies is a looped waveguide with anomalous dispersion that is evanescently coupled to a bus waveguide (fig 8). The theory of light propagation in such resonators is discussed in details in chapter 3, section 1.

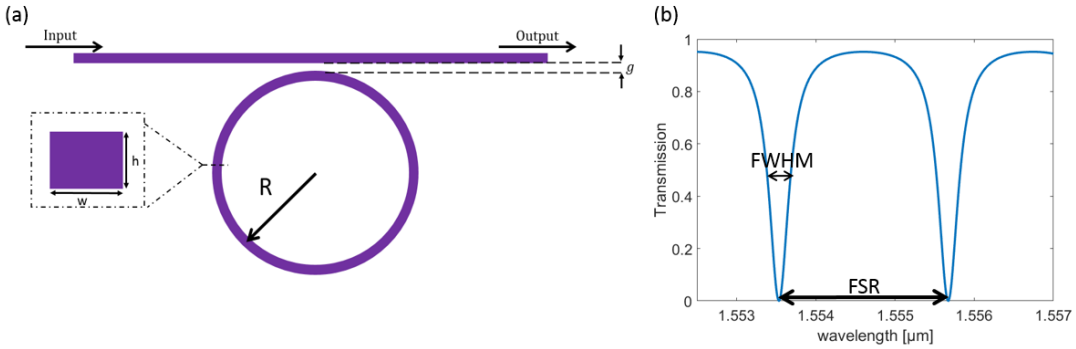

Figure 8- (a) An illustration of a ring resonator coupled to a bus waveguide (b) schematics of the transmission of a ring resonator.

The transfer function of the ring is a regular series of dips in the transmission spectrum (see Figure 8b), which correspond to the different resonances of the resonator. An important parameter is the free spectral range (FSR), i.e. the spectral distance between the neighboring resonances, as given by:

$$FSR = \frac{\lambda^2}{2\pi R n_g} \tag{2.4.14}$$

where R is the radius of the ring and n_g is the group index of the looped waveguide.

If the resonator exhibits anomalous dispersion, the cascaded four-wave mixing processes within the resonator can lead to optical parametric oscillation and eventually Kerr frequency comb generation. Beyond a so-called threshold power, optical parametric oscillation is triggered when the generated signals are sufficiently high to compensate for the intra-cavity losses. Neglecting the influence of the coupling non-ideality and considering being under the phase-matching condition,the threshold power is given by the relation[33]:

$$P_{th} \cong 1.54\left(\frac{\pi}{2}\right)\frac{Q_c}{2Q_L}\frac{n^2 L A_{eff}}{n_2 \lambda_p}\frac{1}{Q_L{}^2} \qquad (2.4.15)$$

where L and λ_p, are the cavity length and the pump wavelength, and Q_c and Q_L are the coupling and loaded quality factors of the micro-resonator at the pump wavelength, respectively.

When the intra-cavity power increases, the intensity of the generated signals increases and these act as new pumps to generate new frequencies by degenerate and non-degenerate four wave mixing (fig 9). For higher pump power, this sequence cascades until a full frequency comb with native line spacing is achieved. This corresponds to the situation where the spectral distance between two neighboring lines exactly matches the resonator free spectral range (FSR). More details about the design of these devices for achieving frequency combs will be given in chapter 3.

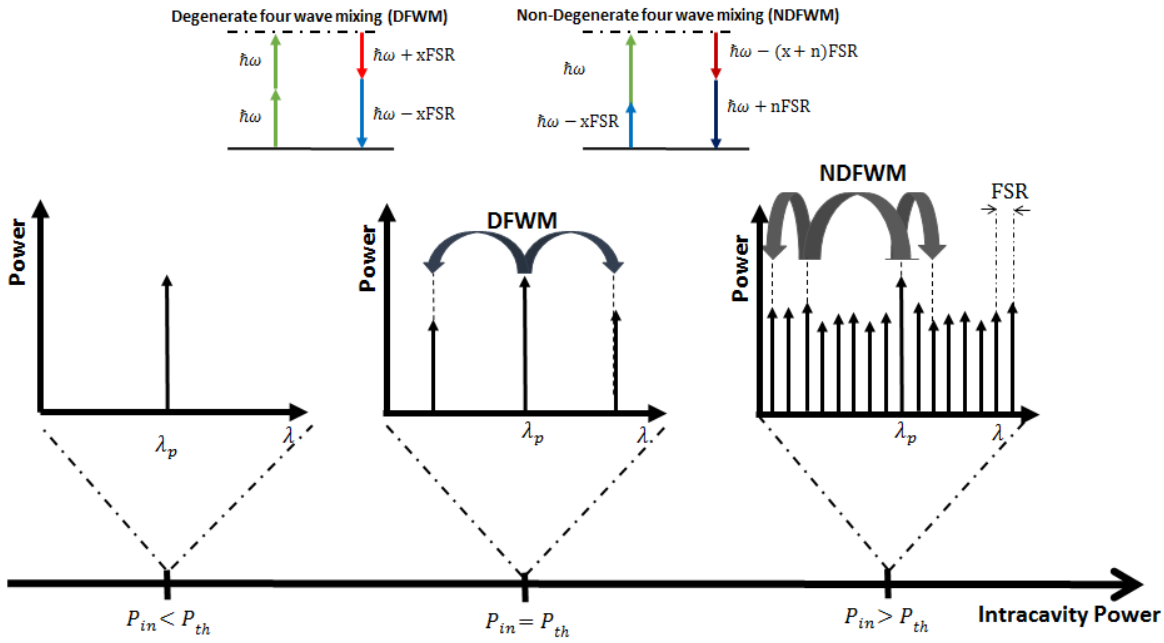

Figure 9- Frequency comb generation mechanism.

Third harmonic generation

Another $\chi^{(3)}$ induced nonlinear process is third harmonic generation (THG), whereby three photons at the pump frequency, ω_p, are converted into one photon at the TH frequency, ω_{TH}, such that $\omega_{TH} = 3\omega_p$. Similarly to four wave mixing, third harmonic generation can be described by using coupled amplitude equations. The coupled amplitude equations for third harmonic generation are as follows [28]:

$$\frac{\partial E_{\mathrm{p}}}{\partial z} = \frac{j\omega_p^2 \chi^{(3)}}{\beta_p c^2} |E_{\mathrm{TH}}|^2 E_p^* e^{-j\Delta\beta z} \tag{2.4.16}$$

$$\frac{\partial E_{\mathrm{TH}}}{\partial z} = \frac{j\omega_{TH}^2 \chi^{(3)}}{2\beta_{TH} c^2} |E_{\mathrm{p}}|^3 e^{-j\Delta\beta z} \tag{2.4.17}$$

In a similar way as for the FWM process, the phase-matching has an important role in the conversion efficiency. The linear phase-mismatch is defined in this case by:

$$\Delta\beta = 3\beta_{\mathrm{p}} - \beta_{\mathrm{TH}} \tag{2.4.18}$$

This equation can be expressed as a function of the effective indexes of the pump and the third harmonic waves, as:

$$\Delta\beta = 3\beta_{\mathrm{p}} - \beta_{\mathrm{TH}} = \frac{1}{c}\left(3\omega_p n_{eff,p} - \omega_{TH} n_{eff,TH}\right) = \frac{\omega_{TH}}{c}\left(n_{eff,p} - n_{eff,TH}\right) \tag{2.4.19}$$

From this equation we can conclude that the effective index at the pump ($n_{eff,p}$) and third harmonic ($n_{eff,TH}$) frequencies must be equal to enhance the efficiency of this process. In practice, it is hard to have materials with a wide bandgap that can maintain this condition, and be transparent for all photon energies. Consequently, this process has typically a low conversion efficiency.

Second harmonic generation

While $\chi^{(2)}$processes should be forbidden in centro-symmetric materials, an effective $\chi^{(2)}$ ($\chi^{(2)}_{eff}$) can arise in waveguides from the interface between a core made from an amorphous CMOS-material and the cladding. Consequently, a second-order nonlinear response can arise from the asymmetric dipole potential formed at the surface [34], [35]. The second-order nonlinear process of second harmonic generation (SHG) is known as frequency doubling where two pump photons are converted from the pump frequency, ω_p, to one photon at the SH frequency, ω_{SH}, such that $\omega_{SH} = 2\omega_p$.

The coupled amplitude equations for second harmonic generation are as follows [28]:

$$\frac{\partial E_{\mathrm{p}}}{\partial z} = \frac{j\omega_p^2 \chi^{(2)}_{eff}}{\beta_p c^2} E_{\mathrm{SH}} E_p^* e^{-j\Delta\beta z} \tag{2.4.20}$$

$$\frac{\partial E_{\mathrm{SH}}}{\partial z} = \frac{j\omega_{SH}^2 \chi^{(2)}_{eff}}{2\beta_{SH} c^2} \left|E_{\mathrm{p}}\right|^2 e^{-j\Delta\beta z} \tag{2.4.21}$$

In a similar way as for the THG process, the phase-matching has an important role in the conversion efficiency. The linear phase-mismatch is defined by:

$$\Delta\beta = 2\beta_{\mathrm{p}} - \beta_{\mathrm{SH}} \tag{2.4.21}$$

This equation can be written as a function of the effective indexes of the pump and the second harmonic as:

$$\Delta\beta = 2\beta_{\mathrm{p}} - \beta_{\mathrm{SH}} = \frac{1}{c}\left(2\omega_p n_{eff,p} - \omega_{SH} n_{eff,SH}\right) = \frac{\omega_{SH}}{c}\left(n_{eff,p} - n_{eff,SH}\right) \tag{2.4.22}$$

From this equation, we can conclude that the effective index at the pump ($n_{eff,p}$) and second harmonic ($n_{eff,SH}$) frequency must be equal to enhance the efficiency of this process.

Another strategy can be used to achieve SHG with high conversion efficiency, like using birefringent materials or through quasi-phase matching in periodically poled lithium niobate or other crystals [36].

2.5 Choice of the material platform

According to the section 2.4, there are several keys to enhance nonlinear processes using integrated optics. In addition to dispersion engineering and the reduction of the waveguide loss, the nonlinear parameter given by equation (2.4.9) highlights the need for tightly confining waveguides (low A_{eff}), as well as a material with a high nonlinear response (high n_2). The choice of the material platform is thus critical for producing efficient nonlinear devices, and a trade-off must be generally found between a highly nonlinear material, and the possibility to achieve low loss from this platform. We present and compare in this section the different material platforms that have been investigated for integrated nonlinear optics with a focus on CMOS compatible materials.

Over the last decades and before silicon has appeared as the most mature optical and substrate material, integrated photonics has been developed on a variety of materials and platforms. The first platform proposed for nonlinear optics in the C-band was AlGaAs III-V semiconductors by exploiting the ability to tune the bandgap by varying the alloy composition [16]. A high gamma parameter has been reported (521 $W^{-1}m^{-1}$) [37] and four-wave mixing [38] and wavelength conversion [39] have been demonstrated. Moreover, high nonlinear parameters (136 $W^{-1}m^{-1}$) have been achieved with Chalcogenide glass waveguides [40], while germanium based chalcogenide glasses seem to be promising [41]. As compared with the silicon-photonics toolbox, the photonics components developed in these platforms are not mature enough to fabricate a complex product (e.g. transceiver). Yet, these materials become more relevant when considering the latest developments that have allowed

them to be heterogeneously integrated onto silicon. The fabrication of such materials with a reliability comparable to that of CMOS materials is still elusive.

By using CMOS-compatible materials, we can significantly reduce the cost of integrated photonics by leveraging the mature processing technology of the microelectronics industry. In addition, these materials could enable the close integration of photonics with electronics in a monolithic approach and avoid multi-chip solutions. The CMOS-compatibility ensures the fabrication of photonic products under high volumes, in existing CMOS-fabs, loaded with the production of electronic integrated circuits. In addition, the mature processing technologies allow for the fabrication of high quality optical devices which is determined by the purity of the materials and the fidelity of fabrication.

In CMOS foundries, the dielectric materials that are commonly available are silicon (Si), silicon dioxide (SiO_2), silicon nitride (Si_3N_4), silicon oxynitride (SiON), germanium (Ge) and high-k dielectrics.

The $\chi^{(3)}$ nonlinear susceptibilities are intrinsic properties of the material. The real part of the nonlinear susceptibility defines the nonlinear index and the imaginary part defines the nonlinear absorption. The nonlinear absorption associated with the third order nonlinear susceptibility is two photon absorption (TPA) that takes place when we pump with high intensity above the half bandgap (Fig. 10).

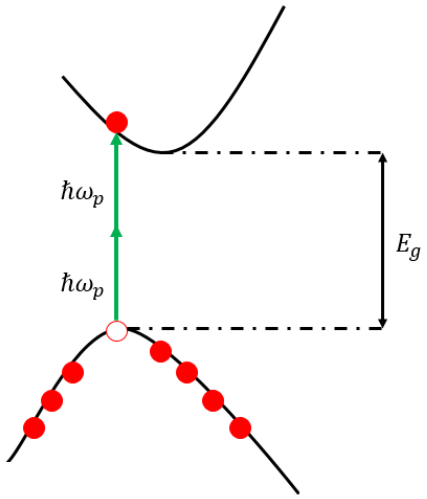

Figure 10- Illustration of two photons absorption

The nonlinear index (n_2) and TPA parameter (β_{TPA}) are related to the third order nonlinear susceptibility as follows [42], [43]:

$$n_2 = \frac{3}{4cn_0^2\varepsilon_0} Re\left(\chi^{(3)}\right) \tag{2.5.1}$$

$$\beta_{TPA} = \frac{3\omega}{2c^2 n_0^2 \varepsilon_0} Im\left(\chi^{(3)}\right) \tag{2.5.2}$$

Often, the relevance of a (transparent) material as a nonlinear material is indicated by a figure of merit (FOM) given by the ratio between the nonlinear index and the TPA parameter. The FOM is useful to assess the nonlinear index with respect to the strength of the TPA and to compare the performance of various nonlinear materials [43] :

$$\text{FOM} = \frac{1}{\lambda}\frac{n_2}{\beta_{TPA}} \tag{2.5.3}$$

A large FOM is preferable to avoid TPA-related limitations. Firstly, TPA is responsible for a loss contribution that increases with the coupled peak power. Secondly, TPA generates free carriers in the conduction band that cause additional dispersion and absorption, which are deleterious for nonlinear processes [27]. Besides, the free carrier lifetime (~1 ns for silicon) imposes a speed limitation on the related nonlinear devices.

In addition to a high nonlinear index, and a low TPA parameter, we already highlighted the need for a tight optical confinement (small A_{eff}) for increasing the nonlinear parameter ($\gamma = \frac{\omega n_2}{cA_{eff}}$) so as to obtain efficient nonlinear processes. This typically imposes a material platform with a high index contrast. At the same time, a low propagation loss is required to get longer effective length (L_{eff}, as per equation 2.4.13) and thus enable stronger nonlinear processes as accumulated across the propagation distance. Finally, making the most of the length is only possible if phase matching is met, which requires the capability to engineer the waveguide dispersion. As discussed in section 2.4, achieving an anomalous dispersion is a condition for some nonlinear phenomena (e.g. degenerate four wave mixing and frequency comb generation). Depending on the material dispersion, specific waveguide dimensions

must be targeted. In silicon nitride for instance, a thick waveguide is typically needed which is challenging to fabricate in the case of this tensile material.

In the following section, we will review the relevant CMOS compatible materials for integrated nonlinear optics and compare them in terms of all these different metrics and characteristics that govern the efficiency of the related nonlinear devices.

Silicon

The prospect offered by the silicon on insulator (SOI) platform to co-integrate photonics and electronics on the same chip, made it an attractive platform for linear photonics and gave it an advance as a ground for the silicon photonic chip industry which aims at replacing the intermediate cards in optical communications. Moreover, the mature manufacturing and the high-index contrast of SOI materials allows for the implementation - over small footprints - of optical functions providing us with the whole silicon photonics toolbox such as optical resonators and laser integration [4], input/output (I/O) couplers [44], high-speed modulators [17], Si-Ge photodiodes [18], as well as filters and wavelength (de)multiplexers [19].

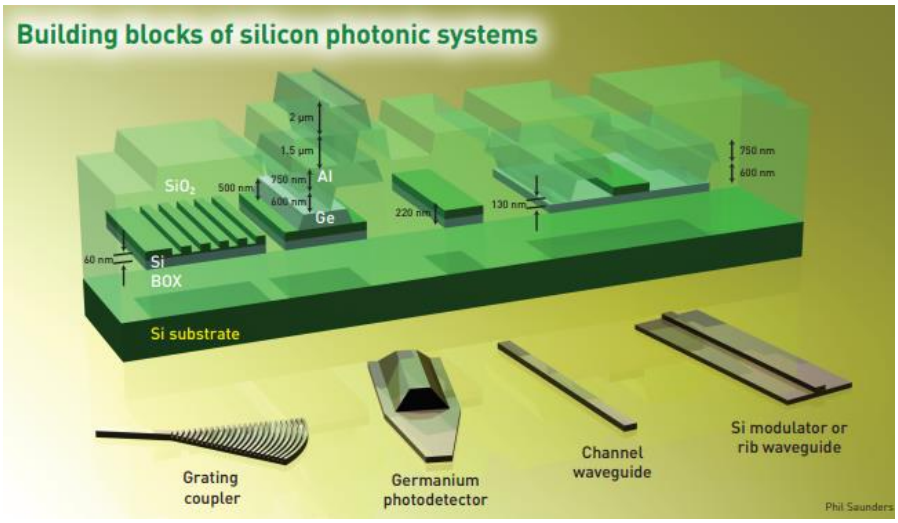

Figure 11- Schematic representation of various building blocks of silicon photonic systems (from [45]).

The high-index contrast of SOI allows for a tight confinement of light, while still providing ultra-low loss (α=0.3 dB/cm) propagation in sub-micrometer waveguides [46].When combined with the high Kerr nonlinearity (n_2) of silicon, the resulting nonlinear parameter γ for single mode silicon waveguides is relatively high (300

$W^{-1}m^{-1}$), and much higher than that of standard silica single mode fibers ($1{,}4.\ 10^{-3}W^{-1}m^{-1}$) for instance.

In addition, dispersion engineering is possible using tightly confining waveguides, which has enabled a wide variety of nonlinear SOI devices such as green light emitters via third harmonic generation [10], light amplifiers by exploiting the Raman effect [47] or four wave mixing [31] and all optical wavelength conversion [48] and demultiplexing [49] via four wave mixing. High Q resonators [50] and photonic crystal structures [51] have also been reported and explored for further increasing the efficiency of nonlinear phenomena.

Effectively, SOI is a very attractive platform for both linear and nonlinear photonics. But the low value of the silicon bandgap (1.12 eV) allows for nonlinear absorption at telecom wavelengths because TPA and TPA-generated free carriers are high at wavelengths shorter than 2 µm. Even though we can reduce the effect of TPA-generated free carriers using, for example, p-i-n junctions to sweep out carriers [52], the silicon FOM is only 0.4 near 1.55 µm [43]. Some studies on hydrogenated amorphous silicon have demonstrated that the FOM can be increased up to 5 [53] but the amorphous silicon tends to suffer from an instability which is not suitable for a product. However, it is probable that beyond 2 µm wavelength where TPA vanishes in silicon making it transparent to both one- and two-photon transitions, silicon will stay a highly attractive platform for nonlinear photonics [54], [55].

Silicon dioxide

Silicon dioxide is widely used in CMOS-foundries. For example, in metal oxide semiconductor field effect (MOSFET) which is used for switching and amplifying electronic signals, the SiO_2 layer forms the gate region. Besides, regarding optics, silicon dioxide is used to fabricate silica optical fibers and thanks to technological advances, the propagation loss has been decreased down to 0.2 $dB.km^{-1}$. On a chip, the first high quality ($Q = 10^8$) 75-µm-diameter resonators have been demonstrated with silica microtoroids [13]. The band gap for SiO_2 is bigger than 9 eV and consequently the two photon absorption parameter is null in the C-band [56], making

silicon dioxide an attractive nonlinear platform. But its nonlinear index is two orders of magnitude smaller than that of silicon [56]. Combined with the low index contrast of the silica (n~1.5 at telecom wavelengths) with the surrounding air, this makes it difficult to realize compact devices in this platform.

As mentioned before, OFC generation has been demonstrated for the first time on a silicon wafer in a fused silica toroidal microcavity [13]. To overcome the low index of silica, the cavity consisted of a free standing disk realized by under-etching the fused silica (see Figure 12).

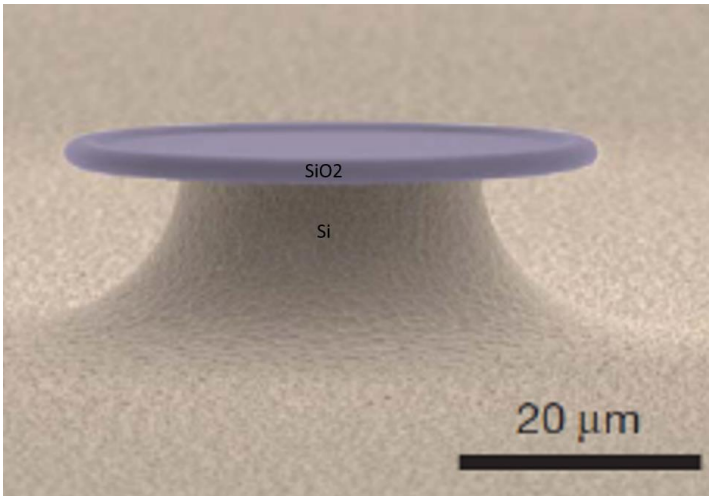

Figure 12-SEM image of a free standing silica torroidal microcavity (from [13]).

Light would otherwise leak into the silicon layer underneath, which has a higher refractive index (3.44). In addition, light is coupled into these resonators by approaching mechanically a tapered fiber which is mounted in a bracket sitting on a piezo translation stage assuring fine positioning of the fiber [13]. This approach is yet very hard to adapt into a robust product.

Silicon nitride

In semiconductor wafer fabrication, a final passivation layer is deposited to protect the die from mechanical damage and corrosion. This process is called glassivation where the silicon nitride is widely used. Besides, the silicon dioxide as well as the silicon nitride are used in electrical isolation and as capacitor dielectric and MOS gate oxides. The silicon nitride represents a trade-off between silicon and silicon

dioxide. The CMOS-compatibility of the silicon nitride combined with its low linear loss, relatively large nonlinearity compared with silicon dioxide (x10) and the absence of any nonlinear loss at 1550 nm (bandgap=5eV) [57] makes this platform highly attractive. Furthermore, the lower thermo-refractive index of the silicon nitride compared with silicon is a significant advantage especially in applications that require high optical power as in the case of LIDARs.

The index of the silicon nitride is around 1.98 at 1550 nm offering an index contrast of 0.5 with the silica-cladding. It thus enables the realization of devices (e.g. waveguides or resonators) that can be co-integrated with other components from the Si-photonics toolbox to get a final product. Moreover, the anomalous dispersion required for some nonlinear phenomena as explained before in the case of FWM is achievable with such refractive index contrast. But due to the lower index contrast for the Si_3N_4/SiO_2 (0.5) with respect to that of the Si/SiO_2 (2) and considering the specific Si_3N_4 material dispersion, anomalous dispersion is achieved with relatively large cross-section waveguides which are thus multimode.

A relatively thick (>700 nm) Si_3N_4 film is required to get anomalous dispersion. Such thick Si_3N_4 films lead to crack formations [16], [56]–[59]. The fabrication of relatively thick Si_3N_4 films with no crack is a technical challenge that has been addressed in this PhD, where a crack-free silicon nitride process has been developed (see chapter 4) [60]. Prior works have demonstrated that trenches could be etched in the buried oxide underneath and be used as crack barriers to get a crack-free area of several cm^2 [57]–[59]. Another solution to get a crack-free stoichiometric silicon nitride is the damascene process from T. Kippenberg's group [24] where the silicon nitride layer is deposited on etched silica and the excess silicon nitride is removed by chemical mechanical polishing. However, this technique reduces the uniformity of the film on the wafer.

Another problem of the stoichiometric silicon nitride is the absorption in the C-band of the N-H dangling bonds [24], [56], [57]. A long thermal annealing step of 1200 °C for three hours in nitrogen atmosphere is adopted in standard LPCVD processes to densify the silicon nitride film, through bringing sufficient energy to break up N-H bonds otherwise causing absorption in the material. These extreme annealing

temperatures would severely degrade the front-end-of-the-line (FEOL) silicon optoelectronic circuits underneath. Specifically, doped optical circuits would be unacceptably affected by the undesirable dopant diffusion in junction-based Si modulators and by the hetero-interface degradation of Ge-on-Si photodetectors. This problem has been also addressed in this PhD and an annealing-free silicon nitride process has been developed with sufficiently low propagation losses (0,6 dB/cm) (see Chapter 5) to generate four wave mixing based frequency combs [61].

The proprietary composition of Hydex waveguides [16] can be an alternative but the nonlinear parameter γ of Hydex is six times lower than that of silicon nitride, thus increasing the required power for nonlinear phenomena, hence the risk of waveguide optical damage. To avoid the absorption in the C-band deuterated, silane (SiD_4) can be used instead of the conventional silane (SiH_4) as a precursor. Deuterated silicon nitride (SiN:D) has been achieved through deposition performed at a lower temperature of 300 °C [26]. However, although being a CMOS-compatible processing building block, it is worth to point out that deuterated silicon nitride can be exclusively used during the back-end-of-the-line (BEOL) fabrication, thus preventing a straightforward monolithic integration with both silicon photonics and sub-100 nm standard CMOS electronics circuitries during a collective FEOL processing [27].

Finally, there has been some studies about engineering the silicon nitride content to increase the nonlinear index without degrading the figure of merit. A so-called silicon rich nitride has appeared as a potential solution to reduce the tensile stress and reduce the fabrication temperature [62], [63]. Even though a high nonlinear index and supercontinuum generation have been demonstrated using this platform, it suffers from relatively high propagation losses (2 dB/cm) due to the presence of Si-H and N-H bonds that absorb at 1.55 µm, making the achievement of optical parametric oscillation elusive. In fact, to the best of our knowledge, no frequency comb has been demonstrated using silicon rich nitride materials without annealing.

Heterogeneous integration of alternative materials onto Si

Because the TPA and the free carrier generation in silicon limit the nonlinear optical functionalities of silicon devices in the C-band, the heterogeneous integration of alternative materials onto silicon has been suggested as a possible solution.

Frequency comb and supercontinuum generation have been demonstrated using AlGaAs on insulator waveguides having propagation losses as low as 1 dB/cm which are fabricated by wafer bonding [64], [65]. This geometry enables the achievement of more tightly confining waveguides, while the associated higher index contrast increases the possibility to achieve dispersion engineering (see Figure 13). However no co-integration with the silicon photonics toolbox has been demonstrated yet.

In addition supercontinuum have been also demonstrated using InGaP on silicon [66]. More recently, electro-optical modulators have been also demonstrated using lithium niobate on insulator platforms [67].

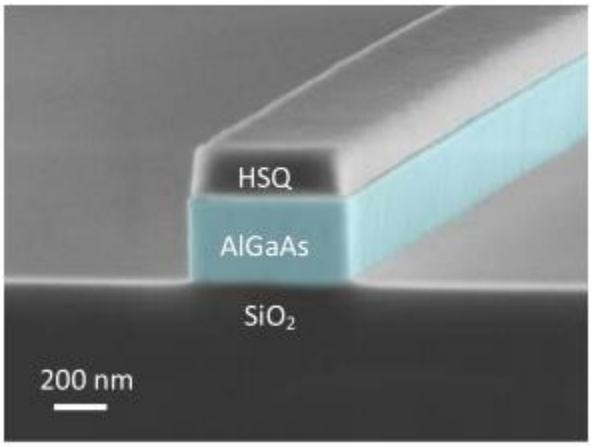

Figure 13-AlGaAs on insulator waveguide fabricated by wafer bonding (from [68]).

Studies have been conducted using the hybrid integration of SOI nanowires with nonlinear organic polymers [69], [70] which usually have a ‘slot’ cross-section.

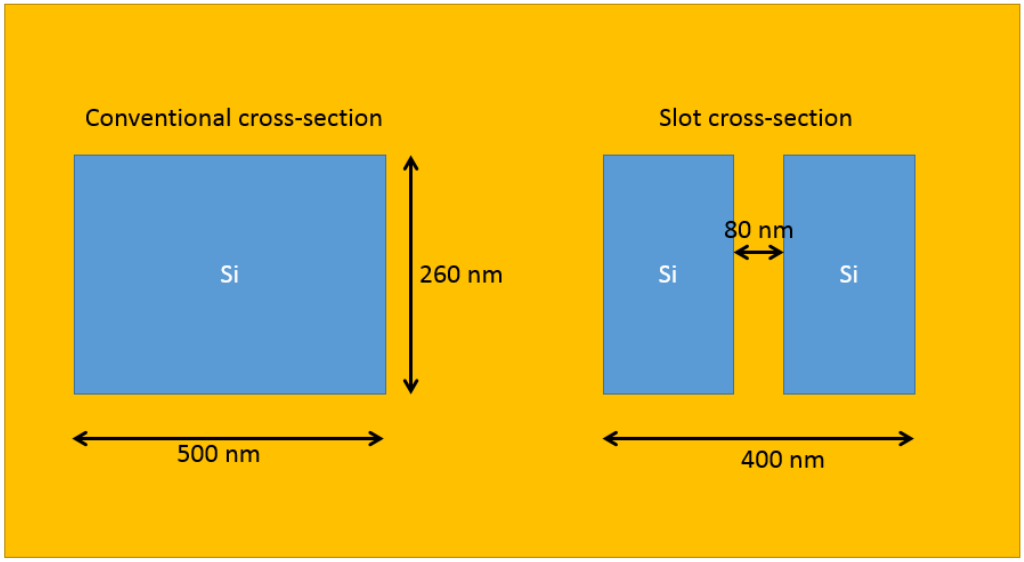

Figure 14- Conventional and slot silicon on insulator cross sections.

The advantage of this approach is to exploit the high nonlinearity and the high FOM of the polymer-filled slot as well as the capability of the SOI platform to realize efficient mode confinement and low loss propagation. This approach also gives an additional degree of freedom for the dispersion engineering [71], even if filling the slot with the right material might be challenging.

To summarize this section, several CMOS compatible material platforms have been investigated for realizing efficient chip-based nonlinear devices, including the hybrid integration approach that enables a suitable nonlinear material to be bonded or combined onto silicon photonic integrated circuits. Each of these platforms has its own advantages and drawbacks, which are reflected by the relevant performance metrics summarized in Table 1. In this thesis, we have focused on Si_3N_4 based integrated circuits which combine a relatively high nonlinearity with respect to that of SiO_2, negligible TPA, the possibility to engineer the dispersion and to achieve long interaction lengths due to low propagation losses at telecom wavelengths.

	c-Si [55]	a-Si [53]	SiO_2 [13]	Si_3N_4	AlGaAs [38]	GaInP [38]
n	3.47	N/A	1.44	1.97	3.3	3.1
$n_2\ [10^{-17}\ m^2/_W]$	0.385	1.54	0.0022	0.03	2.6	0.6
$\beta_{TPA}[^{cm}/_{GW}]$	0.9	0.25	Negligible	Negligible	N/A	0.22
$\gamma[^{W^{-1}}/_{m^{-1}}]$	300	1200	N/A	1.4	660	450
FOM	0.3	5	>>1	>>1	21	1.7
$\alpha\ [dB/cm]$	0.4	4.5	$0.5x10^{-5}$	0.04	1.3	12
$L_{eff-max}[cm]$	10.85	0.96	868000	108.5	3.33	0.36

Table-1: Comparison of linear and nonlinear parameters for different chip-based platforms.

2.6. Conclusion

In this chapter, we briefly described the basic theory of nonlinear optics and presented the key parameters related to the geometry of integrated waveguides that govern the efficiency of different nonlinear phenomena. The underlying material platform must combine a high nonlinearity, low two-photon absorption, low propagation loss, and the possibility to engineer the dispersion. We discussed the dispersion conditions to achieve a four wave mixing based frequency comb (anomalous dispersion) and harmonic generation (equality of the effective indexes at the different frequencies). Adding to this, an overview of different nonlinear platforms has been given, with a focus on the CMOS compatible ones. Following the comparison of these different materials, we have selected, in this PhD, Si_3N_4 as our nonlinear core material. In this work, we have developed the related manufacturing process to decrease the linear loss, while reaching the right (anomalous) dispersion to increase the four-wave mixing efficiency underlying the generation of frequency combs. We present, in the next chapter, the theory and the design of the silicon nitride resonators and waveguides to obtain frequency combs and high-order harmonic generation. The associated experimental results will be presented in chapter 5.

CHAPTER 3

FREQUENCY COMB AND MULTIWAVELENGTH SOURCE DESIGN

Efficient nonlinear phenomena arise when the optical field strongly interacts with the nonlinear material. This can be achieved through enhancing the optical field as in a resonator. An optical resonator can be formed by connecting a bent waveguide to itself along a circular shape. This architecture, known as a ring resonator, was used in this PhD. In this chapter, we present the underlying linear optics theory of ring resonators. More precisely, the resonance condition, the condition to get a critically coupled resonator, the quality factor, the field enhancement and the free spectral range are introduced. Moreover, we present the waveguide cross-section dimensions that are needed to obtain anomalous dispersion using our Si_3N_4 platform. This is the condition to get four wave mixing based frequency combs. Furthermore and as mentioned in chapter 2, a phase matching condition is also required to obtain efficient harmonic generation (third or second harmonic), which we specifically discuss towards the end of this chapter.

3.1. Ring resonator theory

Optical nonlinearities can be enhanced locally within a resonator. The ring resonator is a basic integrated optical structure. The resonator is a looped waveguide which can be accessed evanescently by a (side-coupled) bus waveguide as shown in figure 15. At resonance, very high nonlinear effects can be obtained using low input power thanks to the field enhancement provided by the cavity. We define in this section all the parameters that describe the linear guided-wave optics response associated with such an add-drop filter, and which will be used to design the ring for the intended nonlinear application, in particular frequency comb generation. We assume in this section that the waveguides are single mode, and that, consequently, only the fundamental TE polarized waveguide mode is excited.

From equation 2.3.1, the phase shift associated with an optical wave after travelling a distance d is equal to βd. Thus, at a given wavelength, the phase shift after a round-trip in a ring resonator with a radius R, is:

$$\phi(\lambda) = \beta(\lambda)2\pi R = \frac{2\pi}{\lambda} n_{eff}(\lambda)2\pi R \qquad (3.1.1)$$

where n_{eff} is the effective index at the input wavelength. From the figure 15, the resonance condition is satisfied when there is no phase shift between the fields C_1 and C_2. Consequently, after a round-trip, $\phi(\lambda)$ has to be equal to an integer multiple of 2π and the resonance condition is:

$$m(\lambda_0) = \frac{2\pi}{\lambda} n_{eff}(\lambda_0) R \tag{3.1.2}$$

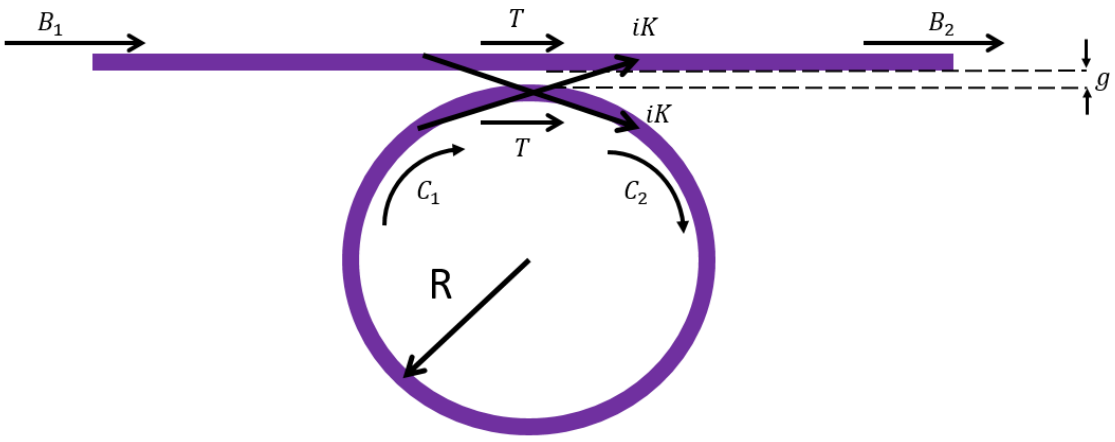

Figure 15- Top-view schematics of an all-pass ring resonator.

where the integer m is the resonant mode number. Supposing that a single clockwise mode of the resonator is excited and the coupling loss is included in the total round trip loss A (defined in amplitude) which is given by:

$$A = e^{-\alpha\pi R} \tag{3.1.3}$$

where $\alpha$is the propagation loss per unit length (defined in intensity), we can describe the interaction between the fields by the matrix relation [72]:

$$\begin{bmatrix} B_2 \\ C_2 \end{bmatrix} = \begin{bmatrix} T & iK \\ iK & T \end{bmatrix} \begin{bmatrix} B_1 \\ C_1 \end{bmatrix} \tag{3.1.4}$$

where B_i and C_i are the field amplitudes in the bus and cavity, respectively, T is the transmission coefficient (in amplitude) and K is the coupling coefficient (in amplitude). The i imaginary value is added for the abrupt phase shift of an ideal coupling regime [73]. Assuming no additional loss (like parasitic out-of-plane-scattering) induced by the coupling, the relation between T and K is:

$$|T|^2 + |K|^2 = 1 \tag{3.1.5}$$

Even if we normalize the input power ($|B_1|^2 = 1$) we cannot extract, from the matrix 3.1.4, the normalized transmitted power ($\left|\frac{B_2}{B_1}\right|^2$) and the normalized circulated power ($\left|\frac{C_1}{B_1}\right|^2$) because we have two equations with three variables. By relating the intracavity fields C_1 and C_2 as:

$$C_1 = C_2 A e^{j\phi(\lambda)} \tag{3.1.6}$$

we can reduce the number of variables to two and get the normalized transmitted power at the output of the bus waveguide and the normalized circulating power in the ring resonator:

$$P_{transmitted}(\lambda) = \left|\frac{B_2}{B_1}\right|^2 = \frac{A^2+T^2-2ATcos(\phi(\lambda))}{1+A^2T^2-2ATcos(\phi(\lambda))} \tag{3.1.7}$$

$$P_{circulating}(\lambda) = \left|\frac{C_1}{B_1}\right|^2 = \frac{A^2(1-T^2)}{1+A^2T^2-2ATcos(\phi(\lambda))} \tag{3.1.8}$$

At a resonant wavelength (λ_0), $\phi(\lambda_0)$ is equal to a multiple integer of 2π and the term $\cos(\phi(\lambda_0))$ is equal to one. The equations of the normalized transmitted power and the normalized power circulating in the ring are thus reduced to, at resonance:

$$P_{transmitted}(\lambda_0) = \left|\frac{B_2}{B_1}\right|^2 = \frac{(A-T)^2}{(1-AT)^2} \tag{3.1.9}$$

$$P_{circulating}(\lambda_0) = \left|\frac{C_1}{B_1}\right|^2 = \frac{A^2(1-T^2)}{(1-AT)^2} \tag{3.1.10}$$

The so-called critical coupling condition is satisfied when the transmission coefficient is equal to the loss in the cavity:

$$A = T \tag{3.1.11}$$

Under this condition, the equation 3.1.10 takes the form:

$$P_{circulating}(\lambda_0) = \left|\frac{C_1}{B_1}\right|^2 = \frac{A^2}{1-A^2} \tag{3.1.12}$$

whereas the transmitted power at resonant wavelengths drops down to zero (Figure 16).

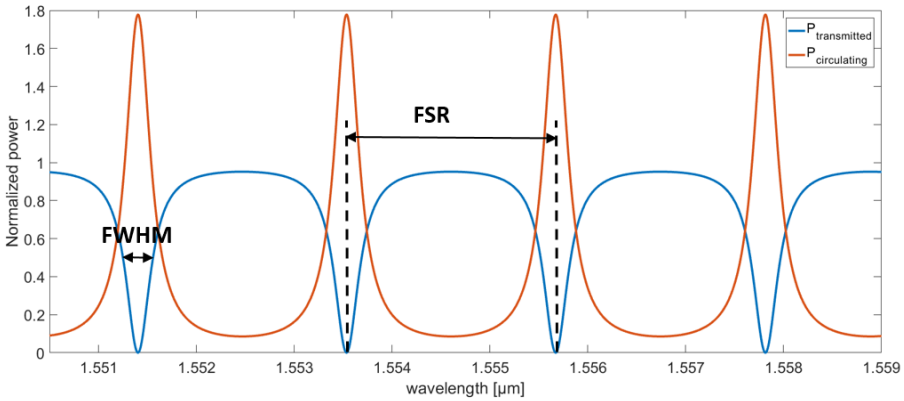

Figure 16- A simulation of the normalized power transmitted (blue) and circulating (red) in a ring resonator. In this simulation, the effective index used is the effective index of a 760-nm-thick Si_3N_4 waveguide and 1.7 μm wide. The round-trip loss factor is A=0.8 which is equivalent to a loaded quality factor of 5100.

Figure 17 shows the normalized circulating power as a function of the propagation loss (i.e equivalently the round-trip loss factor A) for a critically coupled ring. When $A > 1/\sqrt{2}$ (i.e. α<48 dB/cm for a ring with a radius of 100 μm) the circulating power increases and may reach a considerably high level for low losses (when A~1, i.e. α=0.01 dB/cm).

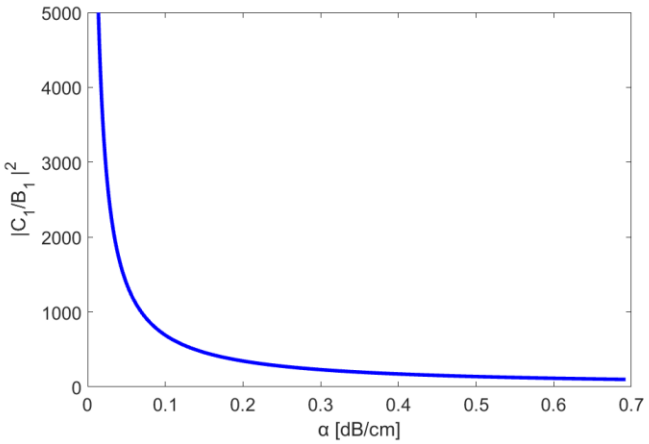

Figure 17- Normalized circulating power as a function of the linear loss of a waveguide forming a ring with a radius R=100 μm.

Critical coupling is desirable since it provides the maximum enhancement of the normalized power circulating in the ring.

This power enhancement defines the Finesse of the resonator. The relation between the maximum of the circulating power and the Finesse allows us to relate the Finesse with the propagation losses of the waveguide forming the resonator as follows:

$$\mathcal{F} = \pi P_{circulating} = \frac{\pi A^2}{1-A^2} = \frac{\pi e^{-2\pi\alpha R}}{1-e^{-2\pi\alpha R}} \tag{3.1.13}$$

Another way to look into the power inside the cavity is through defining the quality factor. The quality factor is the ratio of the total energy stored in the resonator divided by the energy dissipated in a single cycle (one period of oscillation). Experimentally, the quality factor can be also estimated from the transmission spectrum around the resonance by measuring the full width at half maximum $\Delta\omega_{FWHM}$ as follows:

$$Q = \frac{\omega_0}{\Delta\omega_{FWHM}} \approx \frac{\lambda_0}{\Delta\lambda_{FWHM}} \tag{3.1.14}$$

The approximation in the wavelength domain is valid when the quality factor is high. The full width at half maximum ($\Delta\omega_{FWHM}$) is referred to as the resonance linewidth. The relation between the quality factor and the photon lifetime (τ_p) is :

$$Q = \omega_0 \tau_p \tag{3.1.15}$$

This quality factor effectively takes into account the coupling losses and the internal (or intrinsic) losses (radiation, scattering and absorption). This is defined as the loaded quality factor Q_L. Its relation with the intrinsic quality factor (accounting for the internal losses in the ring) Q_i and the coupling quality factor Q_c is as follows [74]:

$$\frac{1}{Q_L} = \frac{1}{Q_i} + \frac{1}{Q_c} \tag{3.1.16}$$

When the resonator is critically coupled ($T = A$), the coupling and the intrinsic quality factors are even, and consequently, each quality factor is equal to twice the loaded quality factor. Moreover, the loaded quality factor of a ring resonator is related to the finesse as follows [74] :

$$Q_L = kRn_{eff}\mathcal{F} \tag{3.1.17}$$

where k is the wavenumber and n_{eff} is the effective index of the associated waveguide forming the ring. Using the equations 3.1.13 and 3.1.17 we can define the relation between the loaded quality factor and the propagation losses which takes the following from:

$$Q_L = \frac{kRn_{eff}(e^{-2\pi\alpha R})\pi}{1-e^{-2\pi\alpha R}} \tag{3.1.18}$$

For high quality resonator (low α<<1), the factor $2\pi\alpha R$ is much less than one. In fact, we can replace $e^{-2\pi\alpha R}$ by the first order Taylor expansion, $1-2\pi\alpha R$, and the equation 3.1.18 becomes:

$$Q_L = \frac{kn_{eff}}{2\alpha} - kRn_{eff}\pi \tag{3.1.19}$$

The equation 3.1.19 is useful to deduce the propagation loss of the waveguide forming the ring from the measured full width at half maximum of the resonance. However, the second term of the equation 3.1.19 is usually neglected because it is typically equal to several thousands, i.e. much lower than the quality factor which is several hundreds of thousands.

The distance between two adjacent resonances is called the free spectral range. Using the equation 3.1.2 we define the free spectral range as follows:

$$FSR(\lambda) = \frac{\lambda^2}{2\pi R n_g(\lambda)} \tag{3.1.20}$$

Note that we replaced the effective index by the group index to take into account the dispersion of the effective index between two resonances using the Taylor expansion of the propagation constant. This equation allows us to infer the group index from the measured spectrum.

3.2. Ring resonator design

As mentioned above, the condition to get a critically coupled ring resonator is that the round-trip loss in the ring must be equal to the transmitted field factor ($A = T$). Using Equations 3.1.3 and 3.1.5 and the first-order Taylor expansion of $e^{-2\pi\alpha R}$, the critically coupled condition can be reformulated as:

$$|K|^2 = 2\pi\alpha R \tag{3.2.1}$$

This implies that the power lost in the ring must be equal to the coupled power. Three design parameters can be changed in the equation to satisfy the critical coupling condition: the radius of the ring (R), the propagation loss (α) that depends on the fabrication quality and the normalized coupled power $|K|^2$ that typically depends on the distance between the ring resonator and the bus waveguide.

To design the ring, we simulated, using full wave 3D-Finite-Difference Time-Domain method, different coupled powers between a straight waveguide and a bent waveguide with a radius R of 100 µm (Figure 18) for different spacing distances between the waveguides. The simulated waveguide has a width of 1.6 µm and a thickness of 740 nm so that it exhibits an anomalous dispersion as we will see later in this section. We assume that only the fundamental mode is excited.

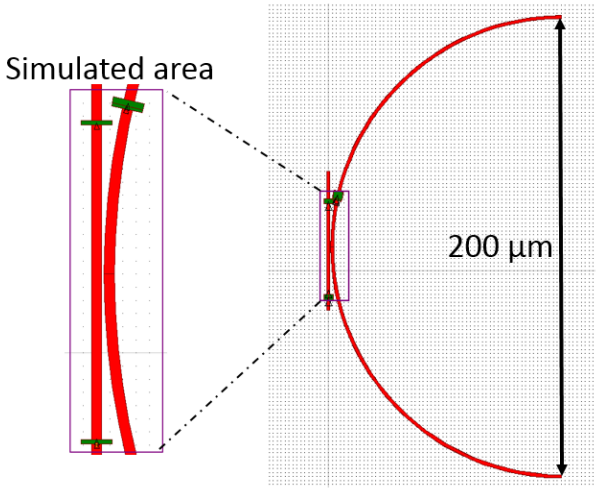

Figure 18- Schematic of the area studied by 3D FDTD Simulation for the coupling between a straight waveguide and a bent waveguide with a radius of curvature R equal to 100 µm.

The coupled power exponentially decreases for increasing spacing between the ring and the waveguides (figure 19). The $|K|^2$ is extracted from the power collected by the monitor placed in the ring during the FDTD simulation.

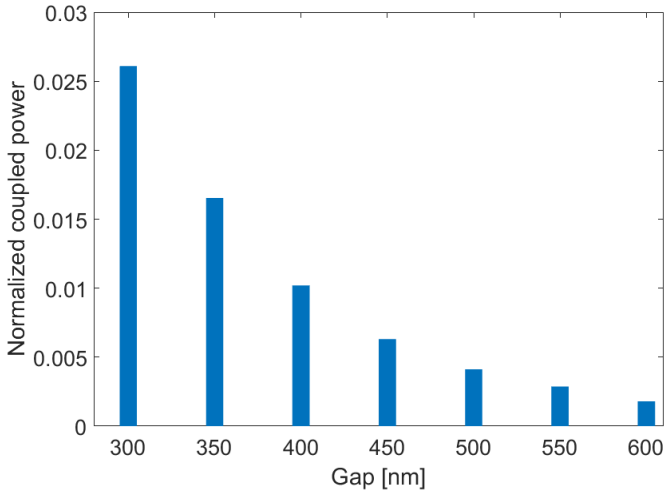

Figure 19- Normalized coupled power $|K|^2$ as a function of the spacing between the bus waveguide and a ring with a radius of 100 µm. The cross-section dimensions of the two waveguides are equal to 1.6umx740nm, and the effective index is equal to 1.8. Only the fundamental TE mode is excited here.

The intra cavity loss ($2\pi\alpha R$) associated with a given combination of propagation losses and ring radius gives the power that has to be coupled ($|K|^2$) in the ring for reaching the critical coupling condition. Assuming that the propagation losses are independent of the ring radius, we present, in the figure 20, the normalized coupled power needed (i.e. equal to the intra cavity losses) to obtain a critically coupled resonator. On this figure, the dashed lines indicate the associated waveguide-ring gaps that allow us to reach the required coupled power for a 100 um ring radius. As expected, the larger the ring and/ or the higher the propagation loss, the lower the gap needed to reach the critical coupling condition.

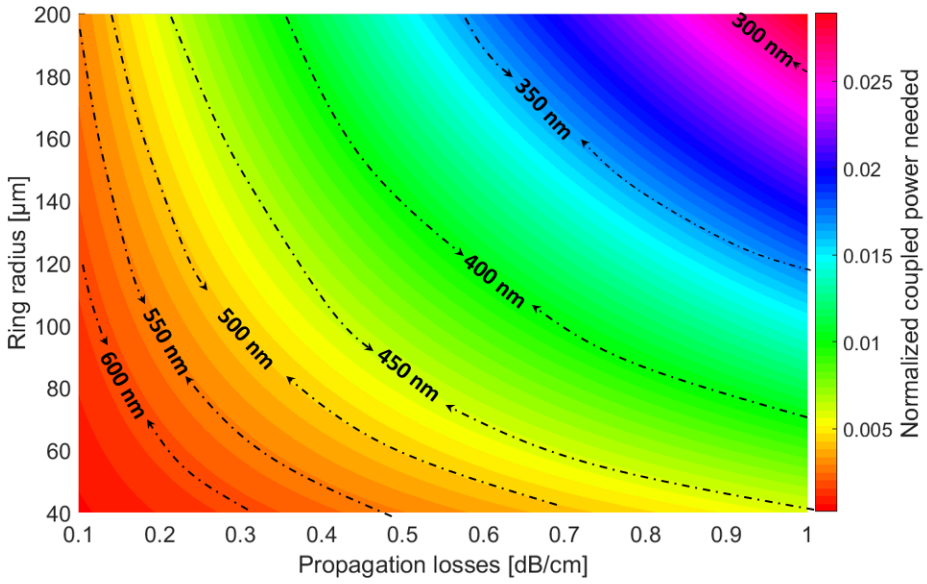

Figure 20- Normalized coupled needed to reach the critical coupling condition for different propagation losses and ring radii. The dashed lines indicate the associated ring-waveguide gaps that enable critical coupling to the fundamental TE mode for a 100 um ring radius. The propagation loss of the ring is considered constant and independent of the ring radius.

From the equation 2.4.15, we can see that the threshold power is proportional to the resonator length. Since the round trip loss increases with the round-trip distance, i.e. the radius of the ring, it is preferable a priori to decrease the ring size. However, when the radius of the ring becomes too small, additional losses, namely bend losses, will occur and increase the total internal losses of the cavity. 3D FDTD simulations are performed to evaluate these additional losses as a function of the bend radius (figure 21). From this, we fixed the minimum radius to 56 µm, so as to avoid any additional contribution from the bending losses (< 10^{-5} per bend) to the intrinsic losses of the ring resonator.

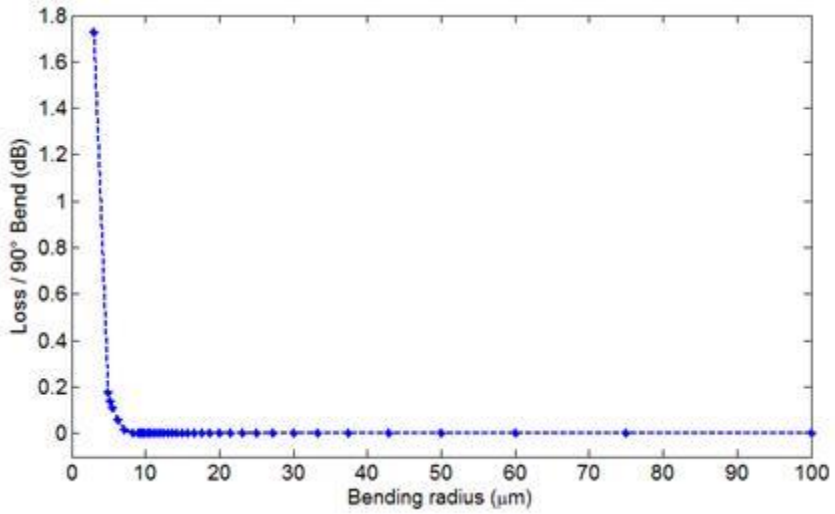

Figure 21- Bend losses of the fundamental TE mode in terms of the bend radius for a (1600 nm × 720 nm) silicon nitride waveguide surrounded by silica

In the absence of any clear value regarding the propagation losses of the Si_3N_4 waveguide at the design stage, we included a range of coupling gaps and ring radius in the lithography mask used for the fabrication of the Si_3N_4 rings, as presented in the table II.

Radius=56 µm	Radius=112 µm	Radius=200 µm
Gap=300 nm	Gap=300 nm	Gap=300 nm
Gap=400 nm	Gap=400 nm	Gap=400 nm
Gap=500 nm	Gap=500 nm	Gap=500 nm
Gap=550 nm	Gap=550 nm	Gap=550 nm
Gap=600 nm	Gap=600 nm	Gap=600 nm

Table-2: The different combinations of the ring radius and waveguide/ ring gap implemented on the lithography mask

Assuming that the coupling efficiency does not depend on the radius of the ring, we expect that by changing the gap and the ring radius between 300-600 nm and 56- 200 µm respectively, we can reach critically coupled ring resonators for a range of propagation loss. This allows us to anticipate variations in the propagation loss of the silicon nitride waveguides.

3.3. Frequency comb related waveguide dimensions

A proper design of the waveguide for frequency comb generation requires the precise knowledge of the material optical properties. It is known that the refractive index of the material changes with the deposition parameters. In this work, the refractive index has been measured after stabilizing the deposition parameters to get sufficiently thick (>700 nm) silicon nitride films, a condition to achieve anomalous dispersion as we will see later in this section. We used the ellipsometry method that analyzes the polarization changes of the light reflected from the sample across the wavelength range of interest to infer the material dispersion (real and imaginary part of the index versus wavelength) of our silicon nitride film. The extinction coefficient lies below the resolution of the measurement. The refractive index extracted from this measurement is fitted with a 12th degree polynom using Matlab (Figure 22). The maximum error between the polynomial fit and the extracted index data is 2×10^{-3}, which is less than the error of the measurement equipment (5×10^{-3}).

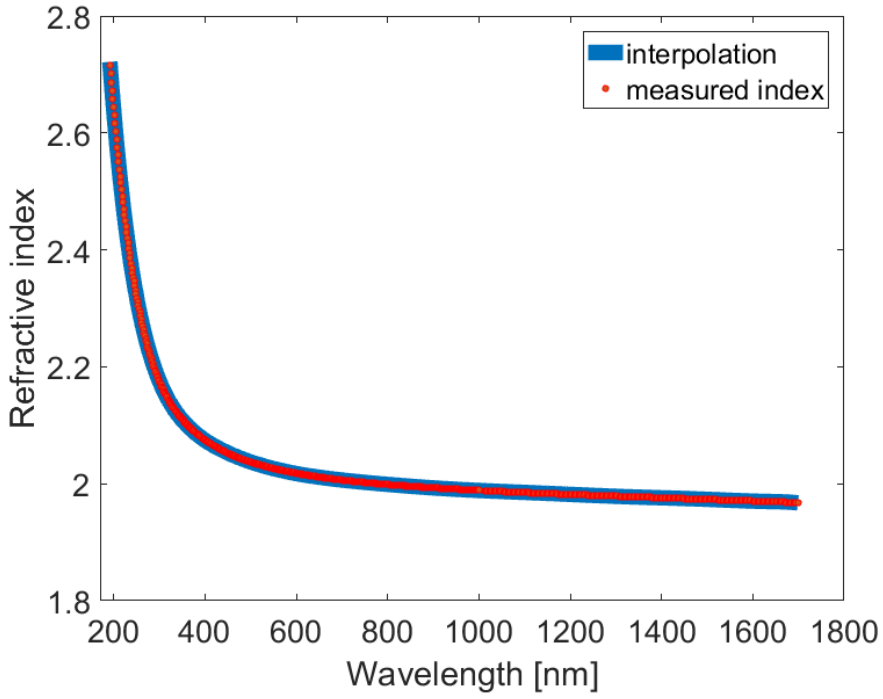

Figure 22- Refractive index dispersion extracted from ellipsometry for our 700nm silicon nitride film (growth conditions of chapter 4), and associated polynomial fit (blue) used for the simulations.

The calculated polynomial dispersion of our silicon nitride material is implemented in a finite difference method solver in order to calculate the waveguide mode

dispersion at 1550 nm (for the fundamental mode) as a function of the waveguide width and thickness. The waveguide is assumed to be fully cladded by silica, for which the dispersion is considered constant.

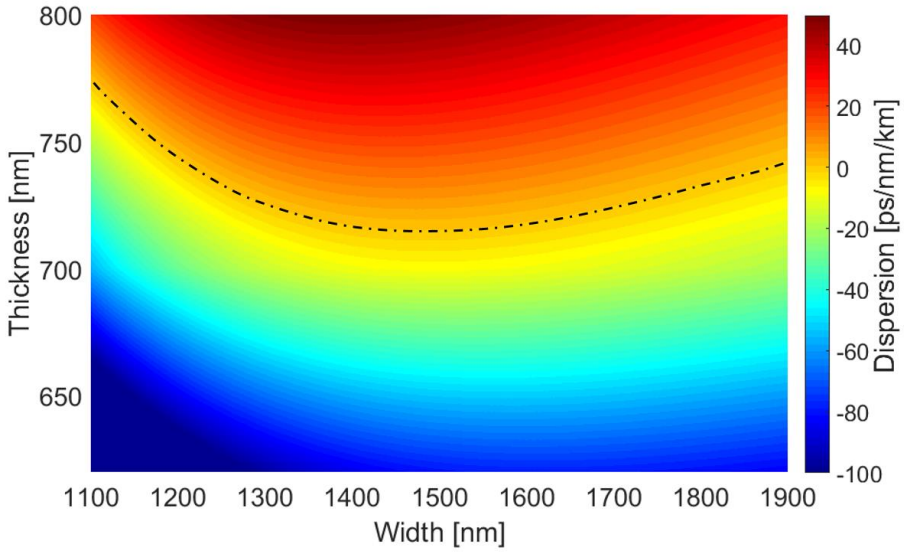

Figure 23- Waveguide mode dispersion for the fundamental TE polarized mode at 1.55um in wavelength as a function of the thickness and the width of the Si_3N_4 waveguide embedded in silica. (n=1.44, and the dispersion of the silica is not taken into account). The dashed line indicate the zero of the group velocity dispersion.

As we can see from the simulations (Figure 23), the dispersion changes drastically with the waveguide cross-section dimensions. Moreover, anomalous dispersion (D>0) can be achieved when the silicon nitride thickness is higher than 700 nm, for a waveguide width around 1500nm.

According to the equation providing the net phase matching condition (2.4.11), the pump power may be used to compensate for a slight (negative) linear phase mismatch, as provided by anomalous dispersion. Consequently, the lower the linear phase mismatch is (i.e. the closer to zero it is), the lower the required pump power for achieving phase matching and, in turn, for maximizing the nonlinear effect. We conclude that it is preferable to operate near the zero group velocity dispersion for observing a nonlinear effect under a lower threshold power, as intended for frequency comb generation.

Furthermore, the dispersion as a function of wavelength changes with the waveguide width, as can be seen on Figure 24. When the waveguide is wider, the dispersion is

flatter, so that the phase matching condition can be satisfied for a wider range of pump wavelengths (Figure 24).

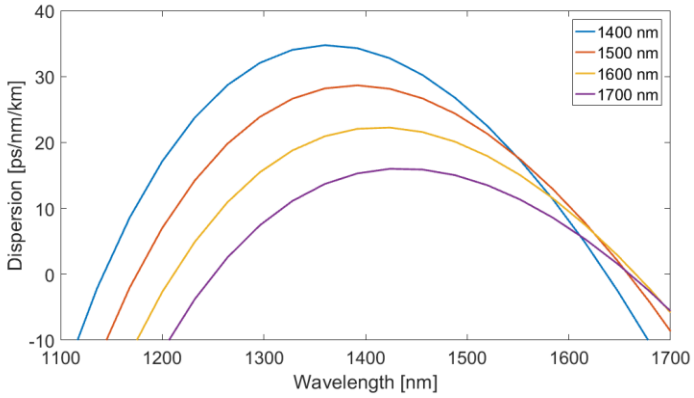

Figure 24- Waveguide mode dispersion for the fundamental TE polarized mode associated with a 720nm thick Si_3N_4 waveguide fully embedded in silica for different waveguide widths.

Considering the need to achieve both a low (anomalous) dispersion with a bandwidth as wide as possible, the chosen waveguide dimensions lie between 1400 nm and 1700 nm with a step of 50 nm. The width of the waveguide is not increased above 1700 nm because a thicker silicon nitride film would then be needed to achieve an anomalous dispersion (see Figure 23) and the gamma parameter would decrease due to a larger effective area. We note that, eventually, considering the dimensions required for reaching the adequate (anomalous) dispersion profile, all the designed waveguides are multimode with four transverse electric modes and four transverse magnetic modes.

3.4. High-order harmonic generation related waveguide dimensions.

In this section, we will discuss the specific design aspects to get efficient second and third harmonic generation in silicon nitride waveguides. As explained in section 2.4, the condition to obtain efficient harmonic generation is the equality between the effective indexes at both the pump wavelength and the high-order harmonic wavelength. The effective index of a given mode (e.g. the fundamental mode) tends to decrease for increasing wavelength. Yet, higher order modes present lower effective indexes since they are less confined in the waveguide core. Thus, phase matching can occur between a high-order mode at the short (harmonic) wavelength and the fundamental mode of the long (pump) wavelength. Moreover, we can see in

figure 22 that the material dispersion at the wavelength of the second harmonic (~775 nm) and the third harmonic (~515 nm) is larger than the dispersion at the pump wavelength (1550 nm). The dispersion variations related to both the wavelength differences and the waveguide dimensions can lead to the crossing (phase matching) between the charts of the effective indexes of high-order modes at harmonic wavelengths and the effective index of the fundamental mode at the pump wavelength.

As in the previous section, the interpolated polynomial fit of the refractive index is implemented in a finite difference method solver. This allows us to accurately simulate the effective index of the fundamental (TE polarized) mode (Figure 25) at the pump wavelength (1520 -1580 nm), as well as the effective index of the higher order modes at the second harmonic wavelength (760 – 790 nm) and at the third harmonic wavelength (506 – 526 nm).

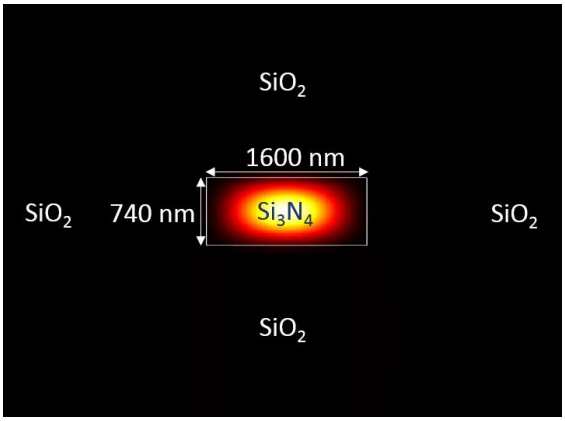

Figure 25- Cross section of the simulated intensity distribution for the TE polarized fundamental mode of a Si_3N_4 waveguide fully embedded in silica at 1550 nm.

The first simulations were performed on a waveguide with a width of 1600 nm and a thickness of 740 nm. The waveguide at the second harmonic wavelength is highly multimode and can guide at least 27 different modes. In this section, the mode order increases for decreasing effective index. The effective index of the fourth TE mode at the second harmonic wavelength is the closest to the effective index of the fundamental mode at the pump wavelength. Yet, the associated effective indexes as shown in Figure 26 do not cross.

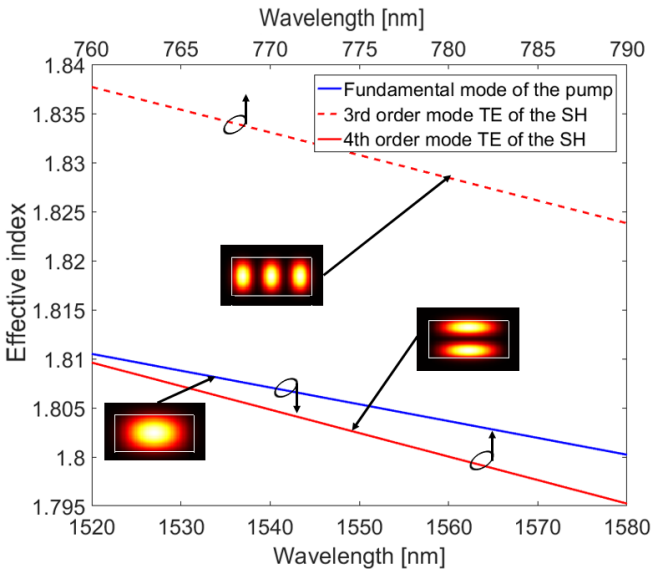

Figure 26- Simulation of the effective index for the fundamental TE mode (blue curve) at the pump wavelength, and for the 3rd and 4th modes (red curves) at the second-harmonic wavelength for a Si_3N_4 waveguide embedded in silica with a cross-section of (1600 nm x740 nm).

Regarding third harmonic generation, the effective index of the 11th TE mode at the third harmonic wavelength is the closest to the effective index of the fundamental TE mode at the pump wavelength. But still, as we can see from figure 27, the effective indexes do not cross in the wavelength range of interest.

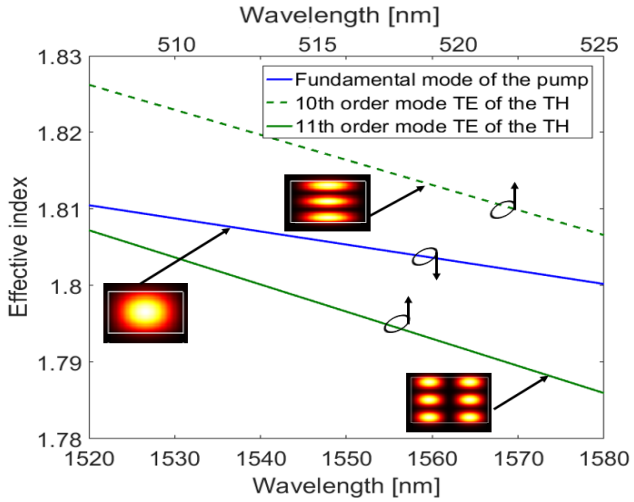

Figure 27- Simulation of the effective index for the fundamental TE mode (blue curve) at the pump wavelength, and for the 10th and 11th modes (green curves) at the third-harmonic wavelength for a waveguide with a cross-section of (1600 nm x740 nm).

By changing the dimensions of the waveguide, we found that for a 1500-nm-wide and 740-nm-thick waveguide, the effective index of the fundamental TE mode at the pump wavelength and the effective index of the 4th order mode (TE polarized) at the

second harmonic wavelength cross. The associated phase matching condition can be achieved at around 1560nm pump wavelength, providing in principle a high conversion efficiency from the pump to the second harmonic (Figure 28).

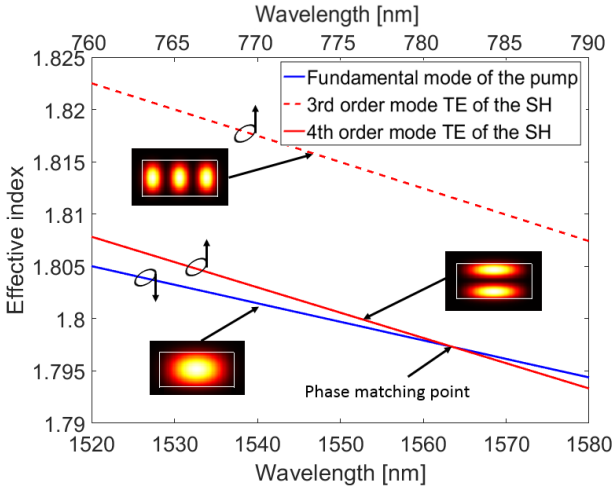

Figure 28- Simulation of the effective index for the fundamental TE mode (blue curve) at the pump wavelength, and for the 3rd and 4th modes (red curves, TE polarized) at the second-harmonic wavelength for a Si_3N_4 waveguide fully embedded in silica with a cross-section of (1500 nm x740 nm).

For a Si_3N_4/ SiO_2 waveguide with a cross section of 1500 nm x740 nm, there is no waveguide mode for which the effective index at the third harmonic wavelength crosses the effective index dispersion curve of the fundamental TE mode at the pump wavelength. However, by reducing the waveguide width to 1400 nm, the phase matching with the third harmonic can be achieved (Figure 29), whereas phase matching with the second harmonic is no longer possible.

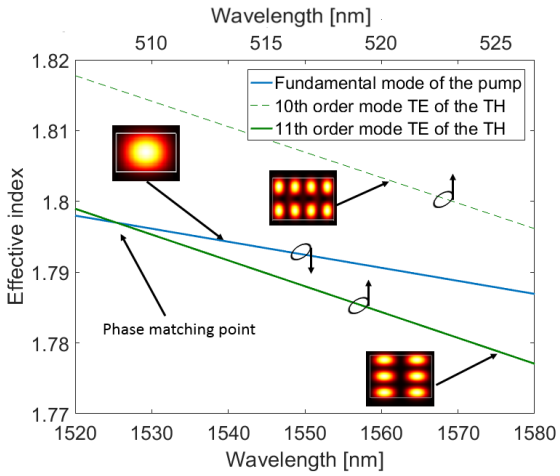

Figure 29- Simulation of the effective index for the fundamental TE mode (blue curve) at the pump wavelength, and for the 10th and 11th modes (green curves) at the third-harmonic wavelength for a Si_3N_4 waveguide fully embedded in silica with a cross-section of (1400 nm x740 nm).

Although we did not study all possible choices for the waveguide width, we think that, providing slight changes in the waveguide dimensions, the phase matching for both second harmonic and third harmonic generation can be achieved simultaneously for the same waveguide, in the targeted pump wavelength range around 1550nm. From this study, we expect that a slight variation of the waveguide width can cause a weak phase mismatch at the pump wavelength for either second or third-harmonic generation.

3.5. Conclusion

In this chapter, we presented the linear guided-wave optics theory of add-drop filters, where a ring resonator is side coupled to a bus waveguide, and the associated parameters that describe the field enhancement in these devices. We then designed the add-drop filter (coupling distance and ring diameter) for reaching the critical coupling condition so as to optimally enhance the optical field, and in turn, the nonlinear processes within the silicon nitride ring. Moreover, the silicon nitride waveguide cross-section dimensions (1500nmx700nm) have been optimized to obtain anomalous dispersion in the telecom band, which is a prerequisite to the generation of four wave mixing based frequency combs. Finally, we investigated the opportunities offered by this platform to provide efficient (second- and third-) harmonic generation. Waveguides of dimensions 1500 nm x740 nm and 1400 nm x 740 nm should be suitable for this, as they can sustain second and third harmonic generation close to the phase matching condition when pumping at telecom wavelengths.

This study points out that the thickness of the silicon nitride required to obtain anomalous dispersion is more than 700 nm. However, the stoichiometric silicon nitride (Si_3N_4) compound is a highly tensed material. This makes it challenging to grow Si_3N_4 films with this thickness. The development of a suitable method to fabricate such films is precisely the focus of the next chapter.

CHAPTER 4

FABRICATION OF Si_3N_4 DEVICES FOR INTEGRATED NONLINEAR OPTICS

The quality factor of ring resonators is mainly determined by the material transparency in the wavelength region of interest (i.e., the C+L bands in our case) and by the scattering loss arising from the sidewall roughness of the waveguide. In the case of ring resonators used for frequency combs generation, a high quality factor alone is not enough. As mentioned before, other conditions apply such as on the waveguide dimensions so as to ensure an anomalous dispersion profile.

In this chapter, we present the fabrication techniques and methods that we have developed to obtain annealing-free and crack-free silicon nitride ring resonators with the right specifications – such as anomalous GVD, high loaded quality factor, and critical coupling conditions – to underpin Kerr frequency comb generation.

4.1. Silicon wafer oxidation

Our fabrication platform uses high-resistivity (i.e., low background doping < 10^{16} cm^{-3}) silicon wafers with 200 mm diameter and 725 µm of thickness. Since the non-intentionally doped refractive index of silicon (3.477) at 1550 nm is much higher than that of stoichiometric silicon nitride (1.983), a thick buried oxide layer is necessary between them. This step is mandatory to isolate the optical mode in the silicon nitride waveguides from the silicon substrate, thus avoiding vertical leakage of light. The electric field energy density of the fundamental optical mode in TE polarization of a silicon nitride waveguide with a thickness of 740 nm and 1500 nm width leaks up to 2.5 µm away from the waveguide boundary in the vertical direction (Figure 30).

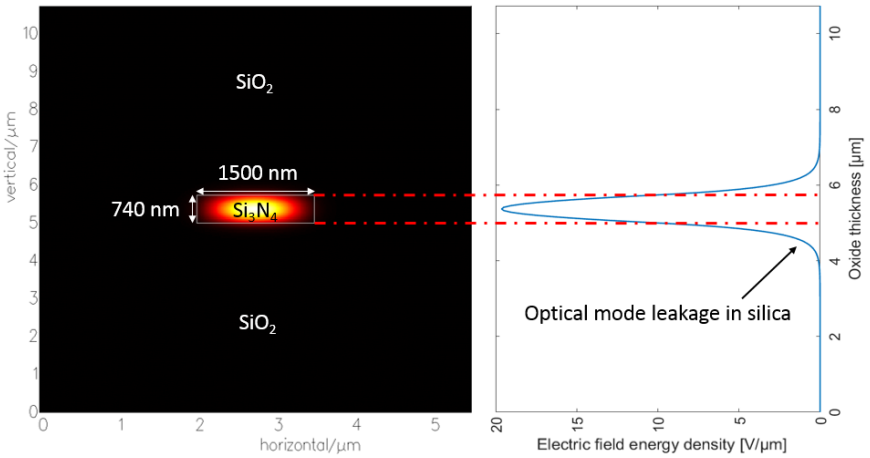

Figure 30- Simulation of the energy density of the electric field for the fundamental TE mode at 1550 nm.

The buried oxide thickness chosen is 3 µm to ensure that there is no leakage in the silicon substrate. The buried oxide can be deposited by plasma-enhanced chemical vapor deposition (PECVD) using tetraethyl orthosilicate (TEOS). However, this silica tends to exhibit impurities. Instead, thermal oxidation has been used in our process to grow 3 µm of buried oxide (SiO_2). Thermal oxidation is carried out in a furnace, which consists of an open quartz tube that is resistively heated to a high temperature (typically > 1000 °C). The wafers are introduced in the chamber horizontally using a quartz wafer boat in order to oxidize several wafers at the same time (Figure 31).

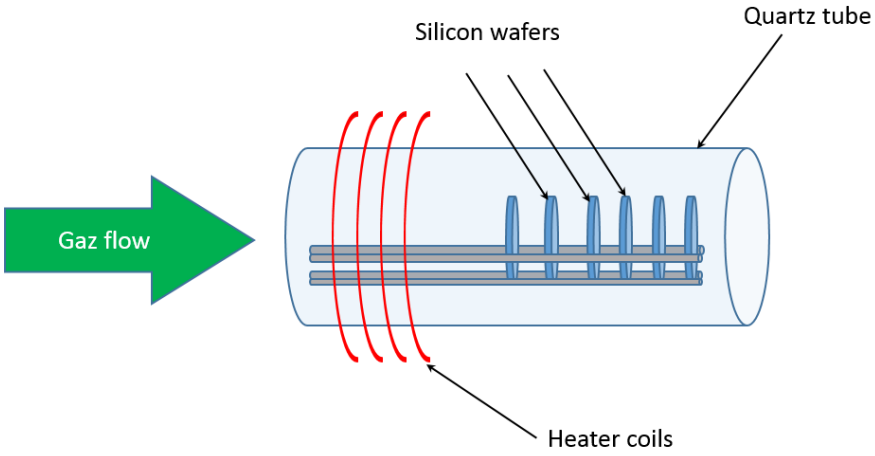

Figure 31- Schematic of the quartz oxidation tube.

There are two ways to thermally oxidize the wafers, either using a dry oxidation or a steam oxidation. The dry oxidation of silicon proceeds according to the chemical reaction:

$$Si + O_2 \rightarrow SiO_2. \quad (4.1.1)$$

This reaction does not require a high temperature and the oxide can be grown in air at room temperature. However, once the formed oxide (called native oxide) is sufficiently thick to a point where the mobility of the oxygen is no longer enough to diffuse through the oxide layer, the reaction stops. In order to grow a thicker silica layer, the silicon wafer must be heated under an oxygen atmosphere. The advantage of this oxidation is that the reaction happens at the Si-SiO_2 interface. In fact, the Si-SiO_2 interface does not see the atmosphere, thus the grown oxide layer is relatively free of impurities. However, this oxidation is only used to grow thin layers of oxide (<300 nm) because it would take a very long time (i.e., several days) to achieve the thickness (3 μm) we need as shown in Fig. 32.

The steam oxidation which we more specifically use in our process to grow the buried oxide is supplied by oxygen from water vapor instead of oxygen gas. The steam oxidation of silicon proceeds according to the chemical reaction:

$$Si + 2H_2O \rightarrow SiO_2 + 2H_2 \quad (4.1.2)$$

Bubbling the oxygen through a source of water allows for the reduction of the reaction temperature and the ability to reach, more quickly, a thick layer of oxide (Figure 32).

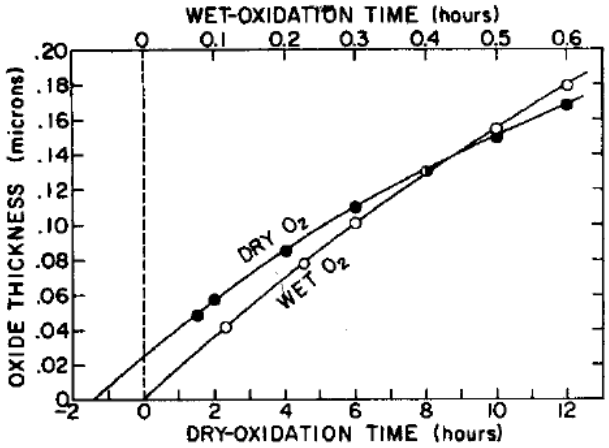

Figure 32- Comparison of initial oxide growth at 920 °C for oxidation in wet (95°C H_2O) and dry-oxygen ambients (from [75]).

The growth time to reach the intended thickness as well as the quality of the resulting oxide depend on the environment, the temperature, the pressure and the characteristics of the silicon wafer (orientation, doping, surface…). However, the thickness of the created oxide does not linearly increase with the oxidation time. To get an estimation of the oxidation time needed to obtain a given thick oxide layer, we can use the Deal Grove model [75] as follows:

$$t\,[hr] = \frac{th_{ox}[\mu m]}{{}^{B}/_{A}\left[\mu\frac{m}{hr}\right]} + \frac{{th_{ox}}^{2}[\mu m]}{B\left[\frac{\mu m^2}{hr}\right]}, \tag{4.1.3}$$

where t is the time required in hours, th_{ox} is the aimed oxide thickness, and ${}^{B}/_{A}$ and B are the linear and parabolic rate constants, respectively. The relations between the rate constants and the temperature ($T[k]$), depending on the oxidation type, are indicated in the table 3.

	Dry oxidation	Wet oxidation
$\frac{B}{A}[\frac{\mu m}{hr}]$	$(3.71\times10^{6}[\frac{\mu m}{hr}])e^{\left(-\frac{2\,[eV]}{\left(8.617\times10^{-5}[\frac{eV}{K}]\right)(T[k])}\right)}$	$(9.7\times10^{7}[\frac{\mu m}{hr}])e^{\left(-\frac{2.05\,[eV]}{\left(8.617\times10^{-5}[\frac{eV}{K}]\right)(T[k])}\right)}$
$B[\frac{\mu m^2}{hr}]$	$(772[\frac{\mu m^2}{hr}])e^{\left(-\frac{1.23\,[eV]}{\left(8.617\times10^{-5}[\frac{eV}{K}]\right)(T[k])}\right)}$	$(386[\frac{\mu m^2}{hr}])e^{\left(-\frac{0.78\,[eV]}{\left(8.617\times10^{-5}[\frac{eV}{K}]\right)(T[k])}\right)}$

Table-3: Deal Grove model linear and parabolic rate constants as a function of temperature.

The atomic volume of silicon is $2 \times 10^{-23}\ cm^3$ against $4.24 \times 10^{-23}\ cm^3$ for wet oxidized SiO_2. Consequently, when we oxidize 1 µm of silicon we obtain 2.12 µm of silica.

Eventually, our wafers have been wet oxidized for 19 hours at 1100 °C to obtain 3.04 µm of buried oxide that effectively isolates the optical mode from the silicon substrate.

Figure 33- Schematic of 3 µm oxidation.

This value is in a good agreement with the value predicted by the Deal and Grove model (18.5 hours). The difference is due to the ramp up and ramp down of the furnace temperature.

4.2. Silicon nitride deposition

The silicon nitride (Si_3N_4) layer can be deposited by plasma enhanced chemical-vapor deposition (PECVD) [76] or low pressure chemical-vapor deposition (LPCVD) [77]. For the deposition reaction, the Si element is supplied by silane (SiH_4) or dichlorosilane (SiH_2Cl_2), and ammonia (NH_3) is used as the nitrogen source. In plasma reactors (Figure 34), the PECVD reaction can take place at relatively low temperature (250 °C <T< 400 °C) with respect to that used in the LPCVD (T>600 °C), thanks to the additional energy supplied by the excited plasma. The reaction chemistry is effectively driven by the plasma, which is a partially ionized gas that can be used to break up molecules, creating chemically-reactive radicals. This avoids the use of high temperatures as a source of activation energy.

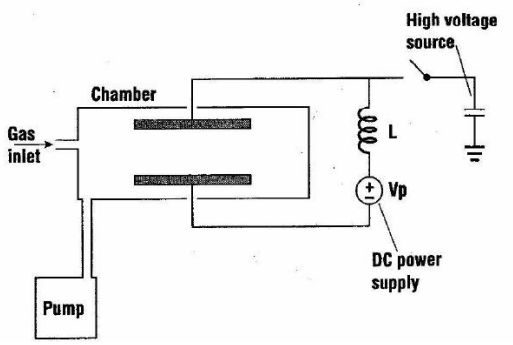

Figure 34- Simple parallel plate plasma reactor [78].

Silicon nitride deposited using PECVD typically contains as much as 20% to 25% of hydrogen [79]. More precisely, in a plasma system, the silicon nitride is formed from the reaction between the silane and the nitrogen discharge according to the reaction formula:

$$2SiH_4 + N_2 \rightarrow 2SiNH + 3H_2 \qquad (4.2.1)$$

The high content of hydrogen in the film is indicated by the H in $SiNH$. The hydrogen content leads to additional losses (Figure 35) in the C-Band due to the N-H bonds [80].

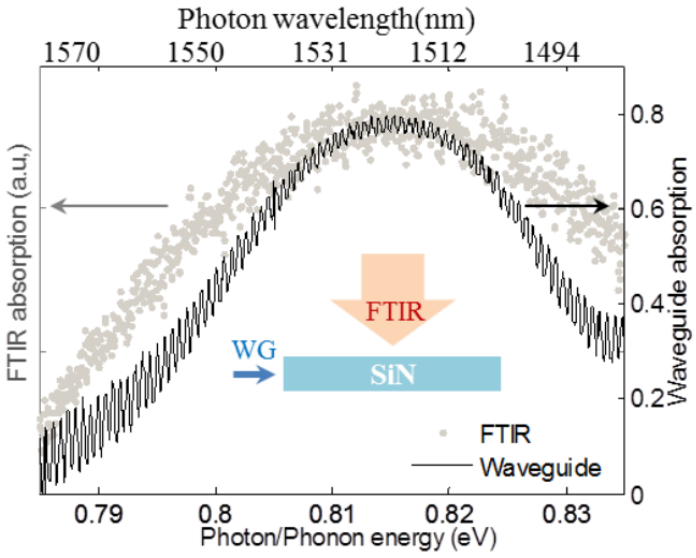

Figure 35- Absorption measurement of PECVD silicon nitride versus wavelength from [81]. The gray dots are the FTIR measurements for a typical as-deposited silicon nitride thin film. The black solid lines are absorption for a related 25 mm long SiN (planar) waveguide [cm^{-1}].

The silicon nitride film deposited by PECVD has a low stress comparing to that deposited by LPCVD, which makes it possible to deposit thick films using the

former technique. However, the additional losses coming from the overtones absorption from the Si-H and N-H bonds preclude the achievement of high quality factor resonators, thus making frequency comb generation using PECVD grown SiN at telecom wavelengths elusive.

In order to minimize the hydrogen content in the silicon nitride film, the LPCVD technique has been used in this PhD instead of the PECVD. The LPCVD reactor is similar to the wet oxidation one, where the wafers are filled vertically in a quartz wafer boat, allowing for the deposition of silicon nitride on several wafers at the same time (Figure 36). The film deposited in a LPCVD reactor coats simultaneously the wafers as well as the internal boundaries of the quartz tube. Therefore, the tube must be periodically cleaned to avoid problems related to particle contamination.

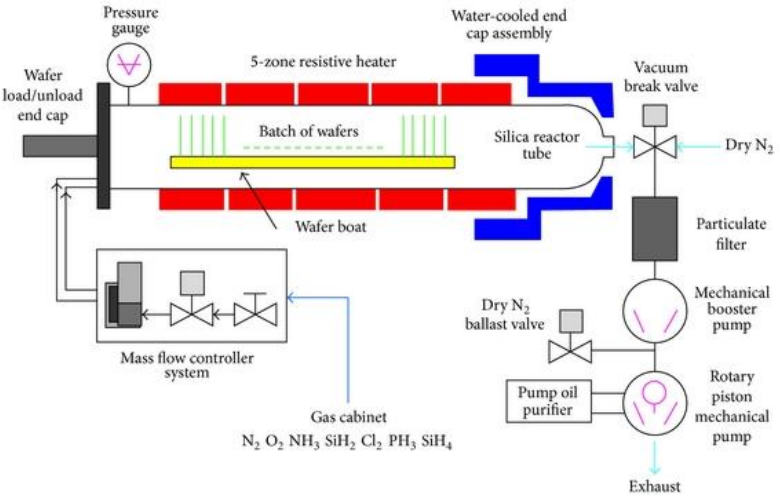

Figure 36- Schematic of a LPCVD reactor (from [82]).

According to FTIR measurements (Figure 37) carried out on LPCVD-grown Si_3N_4 films, there is some evidence of an absorption peak related to the N-H bonds.

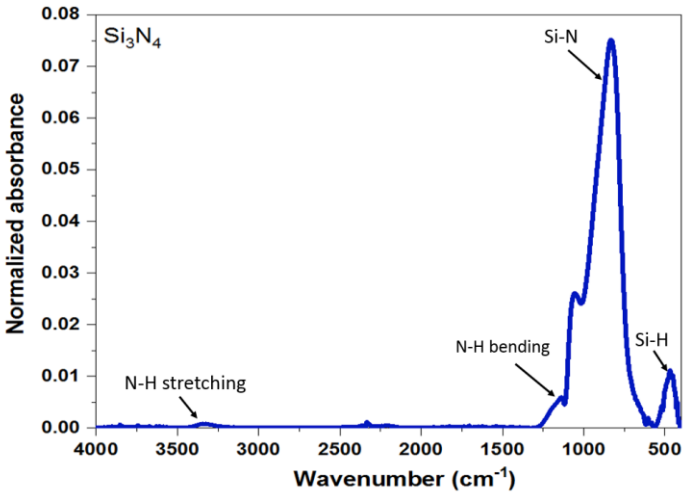

Figure 37- FTIR measurements of the silicon nitride film deposited by LPCVD using the condition described in chapter 4 for a film thickness of 800 nm.

The silicon nitride deposited by LPCVD is not free of hydrogen [83]. In fact, to densify the silicon nitride film through driving out excess hydrogen and break N-H bonds so as to get closer to a stoichiometric Si_3N_4 film and reduce the material absorption loss in the C-band, a long high-temperature annealing (1200 °C for at least 3 hours) is traditionally applied on LPCVD-deposited silicon nitride films [16], [22], [24], [25].

In addition, both the uniformity of the film across the wafer and the film top surface roughness, are two additional important factors to take into account. Accordingly, the initial motivation of our research at the beginning of the PhD project was to deposit silicon nitride films featuring sufficiently low hydrogen content to ensure low loss, a good thickness uniformity across the wafer, crack-free and low surface roughness characteristics, all of this without resorting to the high-temperature annealing step that hinders the co-integration of silicon photonic active and passive devices (see chapter 1).

As mentioned before, in the LPCVD process, the silicon element is supplied by the dichlorosilane precursor and the nitrogen element is supplied by the ammonia precursor. The silicon nitride is then formed from the reaction between the ammonia and the dichlorosilane as follows:

$$3SiCl_2H_2 + 4NH_3 \rightarrow Si_3N_4 + 6HCl + 6H_2 \qquad (4.2.2)$$

The quality and the stress of the deposited silicon nitride film, using the LPCVD technique, depends on the temperature of the deposition, the pressure, the gas ratio (SiH_2Cl_2/NH_3) and the total gas flow.

The deposition rate of the silicon nitride increases (from 2 nm/min to 5 nm/min) with the deposition temperature (from 780 ºC up to 830 ºC), the total gas flow (from 160 sccm to 420 sccm) and the pressure (from 100 mTorr to 300 mTorr).

The reaction 4.2.2 is stoichiometric when 4/3 standard cubic centimeter per minute (sccm) of the ammonia is injected for each 1 sccm of the dichlorosilane. However, when the reaction is stoichiometric, the deposition rate increases, preventing more hydrogen from escaping the silicon nitride film during the deposition. On the contrary, if we decrease the deposition rate to allow more quantity of hydrogen to escape the film, the stress increases and the probability that the film cracks is higher. In order to deposit relatively thick silicon nitride films without cracks occurring, while minimizing the absorption related to the hydrogen content, a trade-off in the deposition rate must be found. After optimizing the process parameters, we found that a deposition rate of 2 nm/min was best suited to our requirements. This rate is obtained at 780 ºC under a pressure of 112 mTorr using NH_3 (200 sccm) and SiH_2Cl_2 (40 sccm) as gas precursors, thus providing a ratio of 0.2 between the two precursors (SiH_2Cl_2:NH3). Critically, under such a low deposition rate, which is 40% lower than that of the standard LPCVD silicon nitride recipes reported in [57] and 30% lower than the deposition rate mentioned in [84], the thermal activation energy enables silicon and nitrogen to dispose at the silicon nitride film surface via atomic surface migration phenomena while compelling hydrogen to escape the film.

That being said, for this set of deposition parameters and low deposition rate, we found that the deposition of more than 500 nm of silicon nitride in a single run was difficult because of the crack formation across the film arising from the cumulated tensile strain. There are two kinds of stress of opposite signs: the tensile and the compressive one (Figure 38).

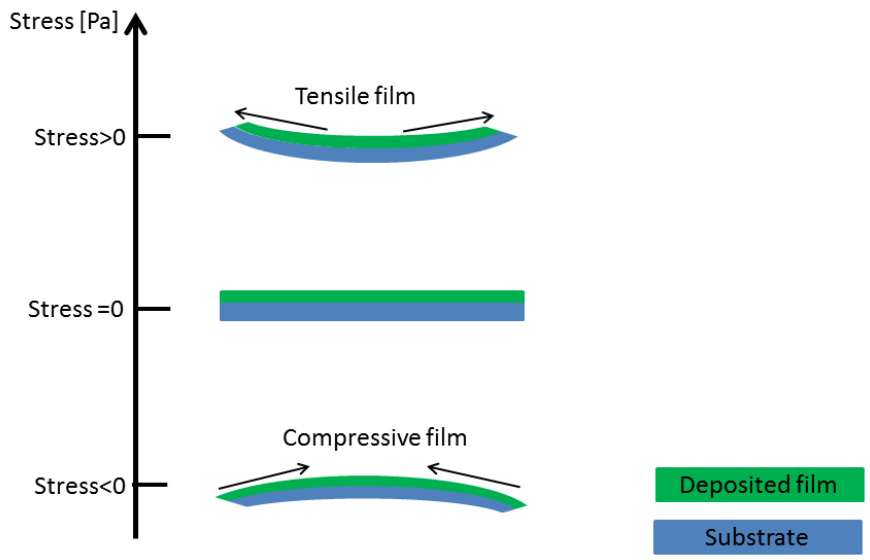

Figure 38- Conceptual diagram of a compressive, balanced and tensile film.

When grown on silica, the silicon nitride deposited following the aforementioned LPCVD parameters acts as a high tensile material where the stress can go up to 1.5 GPa, leading to some cracking film damage when a thick film (> 500 nm in thickness) is deposited (figure 39).

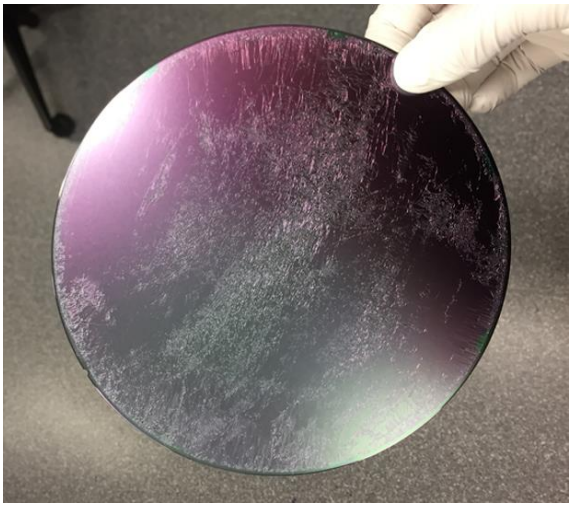

Figure 39- Cracked silicon nitride film (thickness=600 nm) deposited by LPCVD on a 200 mm silicon wafer with 3 um of buried oxide.

As we can see in figure 39, the highly tensed area (where the cracks are concentrated) seems to be uniaxial. In fact, to deposit more than 700 nm of silicon nitride, which is a prerequisite to obtain anomalous dispersion waveguides and frequency comb generation, the deposition is performed in two steps of 370-nm-thick

layer each with the wafer being rotated by 45° between each step in order to distribute the uniaxial strain, thus avoiding film cracks (Figure 40).

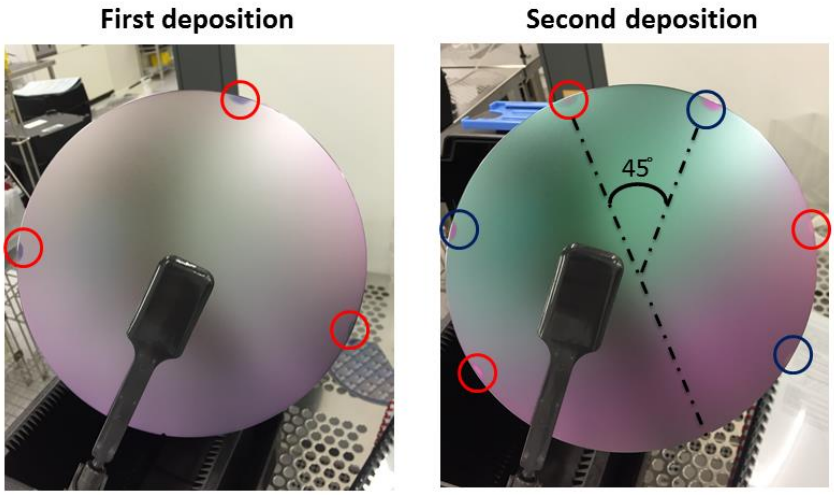

Figure 40- Backside of a silicon wafer after the first deposition (left) and the second (right) deposition of 370-nm-silicon nitride layer by LPCVD. The red circles and the blue ones indicate the positions of the holder during the first and the second deposition respectively.

More precisely, each deposition run is carried out at 780 °C with a post-deposition cooling to around 630 °C for 20 minutes (see Figure 41). Controlled ramp-ups and -downs from/to 780 °C at 10 °C/minute to/from 630 °C are used prior to each deposition. Moreover, the rotation of the wafer is performed at 25 °C because this step is done manually and not automated.

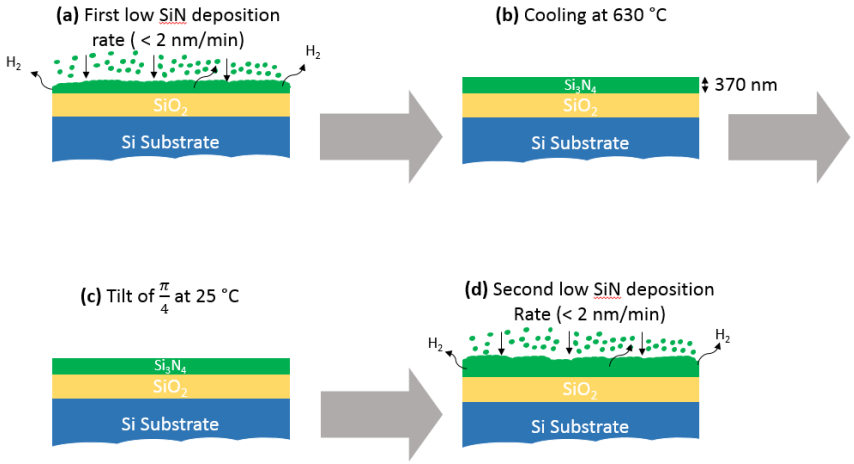

Figure 41- Schematic of the two-step silicon nitride deposition by LPCVD.

For comparison, the deposition of silicon-rich silicon nitride (SRSN) requires a gas ratio (SiH_2Cl_2:NH_3) higher than 2 [57] which typically implies an increase in the SiH_2Cl_2 gas flow and a decrease in the NH_3 gas flow rate. According to [85], a decrease in the NH_3 gas flow inevitably translates into an increase in the deposition rate. Regarding nitride-rich silicon nitride (NRSN) films, the deposition rate is of the order of 17 nm/min [86] which is much higher than our deposition rate.

The long thermal annealing step adopted in standard LPCVD processes for nonlinear photonics enables a high-quality structural reorganization of the physical-chemical architecture of the amorphous film, through bringing sufficient energy to break up N-H bonds, otherwise causing absorption in the material. By reducing the content of residual hydrogen [24], [56] in the silicon nitride film, the high tensile strain is a clear indication of the film stoichiometry [56], [57]. In order to evaluate the stoichiometry of as-deposited films fabricated via our annealing-free LPCVD deposition process and of that deposited by the standard LPCVD process *prior* to the long post-annealing step [24], we compared their respective tensile strains. The stress of our silicon nitride film is inferred by measuring the wafer bow, before and after removing the silicon nitride from the wafer back side using the Stoney equation:

$$\sigma_f = -\frac{E_s}{(1-\upsilon_s)}\frac{h_s^2}{6h_f}\frac{8\,Bow}{\phi^2} \tag{4.2.3}$$

where E_s is the silicon Young modulus (130 GPa), υ_s is the Poisson coefficient (0.28), h_s is the substrate thickness (723.6 μm), h_f is the non-annealed Silicon nitride thickness (500 nm), Bow is the difference of the measured bow before and after removing the silicon nitride from the backside of the wafer and ϕ is the silicon wafer diameter (200 mm).

The material morphological characterization study revealed a tensile strain around 1200 MPa, which is 1.5*x* times higher than the value of 800 MPa reported in [24] and considered, so far, as the state of the art in stoichiometric silicon nitride processing for nonlinear applications and optical parametric oscillators. This clearly indicates the high quality of the silicon nitride film grown via our optimized process, which is very close to the intended Si_3N_4 stoichiometric composition.

Regarding the film thickness uniformity, thickness measurements are performed by ellipsometry on nine different areas for two different 200 mm wafers (figure 42). The measurements are presented in table 4.

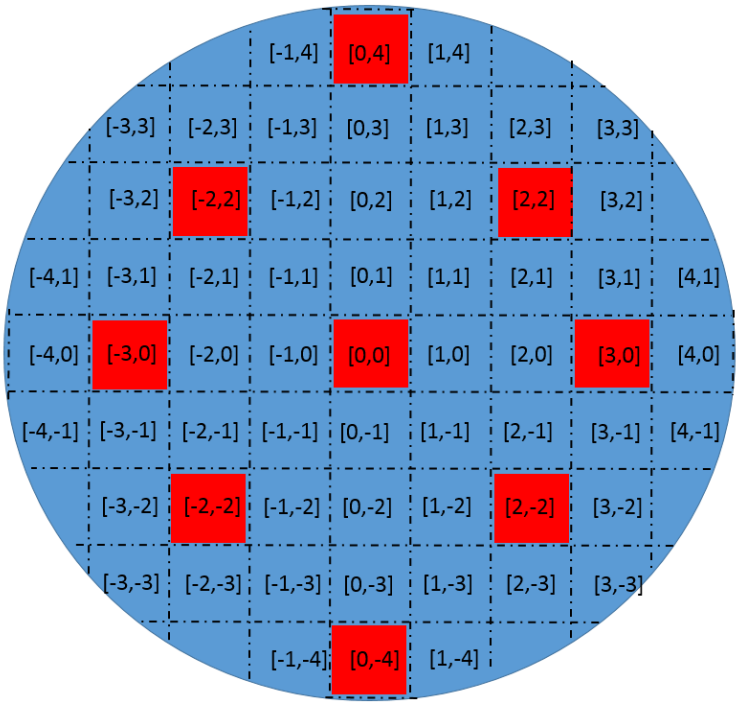

Figure 42- Silicon nitride deposited on a silicon wafer. The red zones are the zones where the thickness measurements are performed and indicated in the Table 4.

	[0,0]	[3,0]	[-3,0]	[0,4]	[0,-4]	[2,-2]	[-2,-2]	[-2,2]	[2,2]
Silicon nitride film thickness on wafer 1 [nm]	775.29	790.03	782.30	798.96	785.74	784.37	779.09	786.22	790.63
Silicon nitride film thickness on wafer 2 [nm]	767.91	783.71	777.63	793.51	786.57	779.61	774.88	780.27	783.25

Table-4: Silicon nitride film thickness measurements on different areas for twodifferent wafers.

We infer from the measured values, that the film is thicker on the wafer side than at the wafer center. In order to calculate the standard deviation of the thickness we used the following formula:

$$\sigma = \sqrt{\frac{\sum(X_i - \bar{X})^2}{N}} \tag{4.2.4}$$

where X_i are the measured values from table 4, $\bar{X}$ is the mean value (785.8 nm for wafer 1 and 780.8 nm for wafer 2) and N is the number of measurements (9). For the 780 nm thick Si_3N_4 films grown using our optimized process, the measurements revealed standard deviations of only 6.5 nm (0.8 %) for the wafer 1 and 6.84 nm for the wafer 2 (0.87 %) across the 200 mm wafer diameter.

The propagation losses are due to the scattering-related process, bulk-related absorption (hydrogen overtone, TPA, MPA, defects and FCA) and absorption caused by impurities that are related to the reactor and the clean-room environment class. On a first approximation, if we consider just the scattering-related processes, the propagation losses of a waveguide depend on the sidewall as well as the top and bottom roughness of the waveguide. To estimate the latter, before patterning the waveguides, we used an atomic force microscope (Figure 43) that provides a measurement of the surface roughness of the as-deposited film. When the surface roughness interacts with the cantilever, the latter is displaced so that the reflection of the incoming laser beam is also displaced on the surface of the photodiode. This magnified displacement is analyzed in order to measure the surface roughness.

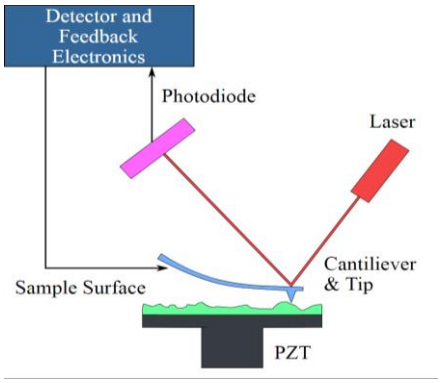

Figure 43- Block diagram of atomic force microscope using beam deflection detection.

The AFM measurement revealed a 0.4 nm surface roughness. To reduce it even further, a *touch* chemical mechanical polishing of 10 nm in thickness is eventually performed on the wafers and the surface roughness is reduced down to only 0.09 nm (Figure 44) which is at the limit of the AFM resolution.

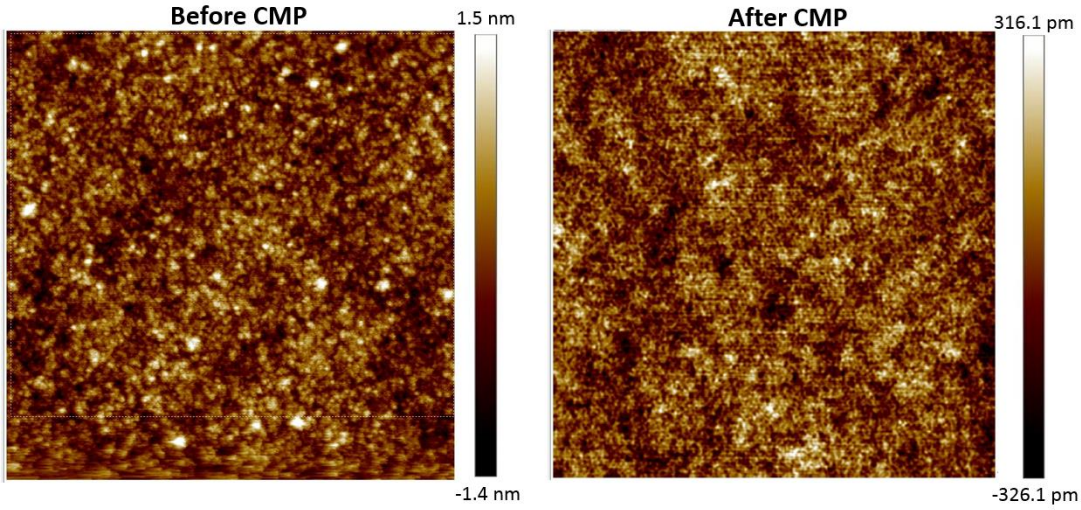

Figure 44- Surface roughness of the Si_3N_4 780 nm thick film deposited by LPCVD, as measured by AFM before and after the chemical mechanical polishing (CMP).

4.3. Patterning of the Si_3N_4 devices

Lithography

After the silicon nitride deposition, the film is patterned and etched to remove the undesired silicon nitride according to the waveguide and resonator design. Etching the silicon nitride film is performed with directive plasma applied on the wafer. Prior to this, the areas where the silicon nitride film must be preserved on the wafer have to be protected. For this, the silicon nitride is coated with a 780-nm-thick M78Y photoresist (positive tone photoresist), a light-sensitive organic material that changes from insoluble to soluble when exposed to 248-nm-light using a Krypton fluoride (KrF) excimer laser with subsequent annealing at 100 °C for one minute. After the lithography step, the soluble photoresist is selectively removed from the exposed area by an aqueous solution (developer). The key polymer for the 248 nm lithography is the poly(4-hydroxystyrene) and the industrial standard developer is aqueous tetramethylamoniumhydroxide solution [87]. In order to selectively expose the photoresist with 248-nm-light, the lithography uses a chromium mask that contains the patterns to be realized so as to hide the photoresist that has to stay on the wafer and keep it insoluble to protect, in these areas, the silicon nitride from the chemical-physical action of the etching plasma (Figure 45).

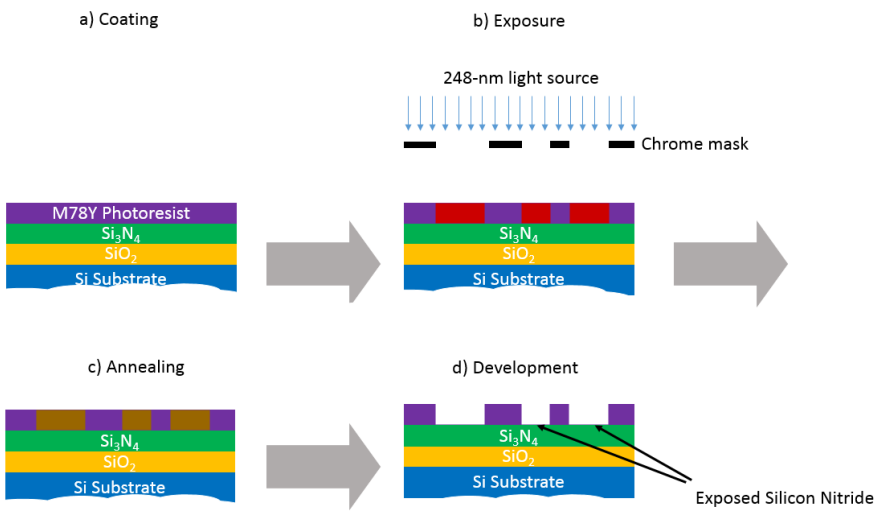

Figure 45- Schematic of the photolithographic process using a positive-tone resist.

Note that if a negative tone photoresist is used, the unexposed parts of the photoresist will stay after the development. Consequently, the chromium mask for a negative resist exhibits the complementary patterns to that of the chromium mask designed for a positive tone photo resist (figure 46).

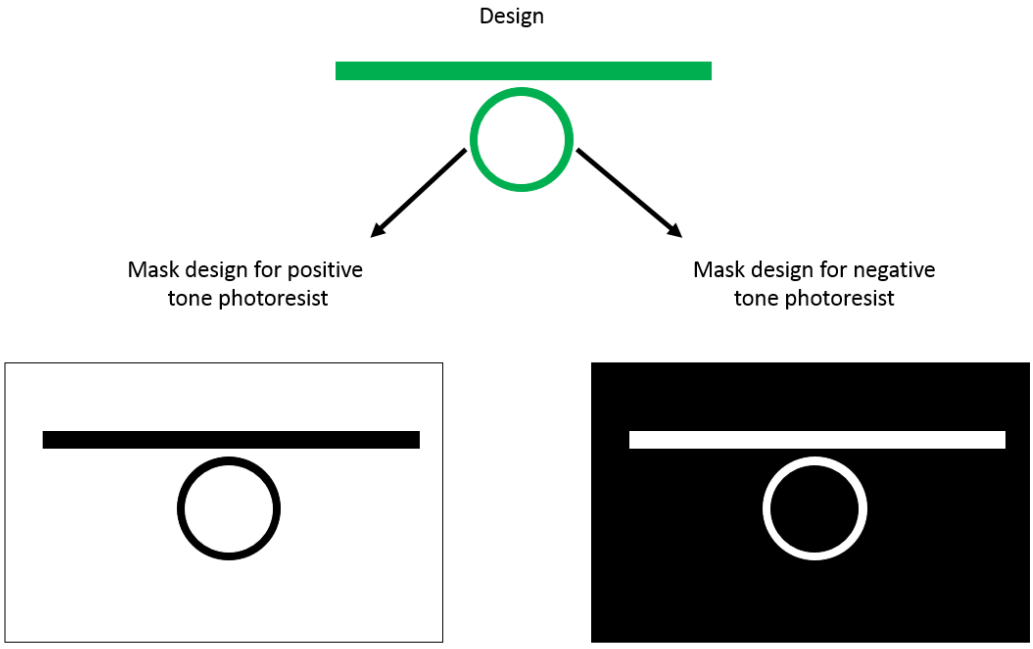

Figure 46- Intended design, mask design for positive and negative tone photoresist.

The photoresist reaction to UV-light depends on its intensity. In order to properly expose the photoresist, the resist exposition dose of the 248-nm-light [expressed in

mJ/cm^2] must be optimized. When the dose changes, the width of the developed pattern changes as well. Generally, in the case of a positive tone photoresist, when the dose is higher, the width of the developed photoresist is smaller and the space between two neighboring patterns is wider. Furthermore, the light used for the photo-lithography tends to be reflected on the interface between the resist and the film stack, so that interferences take place between the incident and the reflected light, which degrades the reliability of the lithography. To minimize these parasitic reflections, a 49 nm thick bottom anti reflection coating (BARC) is spin-coated to the stack prior to the photoresist spinning. Note that the bottom anti reflection coating is not removed when the photoresist is developed and it has to be etched selectively via a $Ar/Cl_2/O_2$ plasma process.

The actual features contained on the chromium mask are 4X bigger than the designed features on the gds mask file. A converging lens is used to get the desired dimensions on the wafer (Figure 47). Moreover, the wafer is not exposed as a whole at the same time, but subsequent 2.2 cm x 2.2 cm (DUV field) field areas are lightened at once for each exposure step (Figure 47) in a typical step-and-repeat lithographic approach.

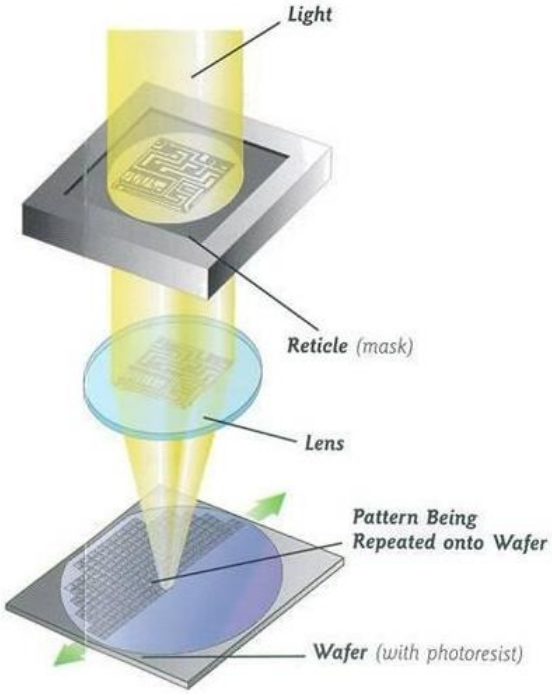

Figure 47- Principle diagram of the lithography machine (From [88]).

After the aforementioned wafer coating by the 49nm BARC and 780nm thick M78Y resist, a deep-UV (DUV) lithography was performed on a ASML-300 stepper using 248-nm DUV. The suitable dose to obtain the critical dimension features as designed in the gds file mask was 26 mJ/cm^2. A scanning electron microscope image of a feature designed to be 400-nm-wide as well as a 200-nm-tip is presented in the figure 48.

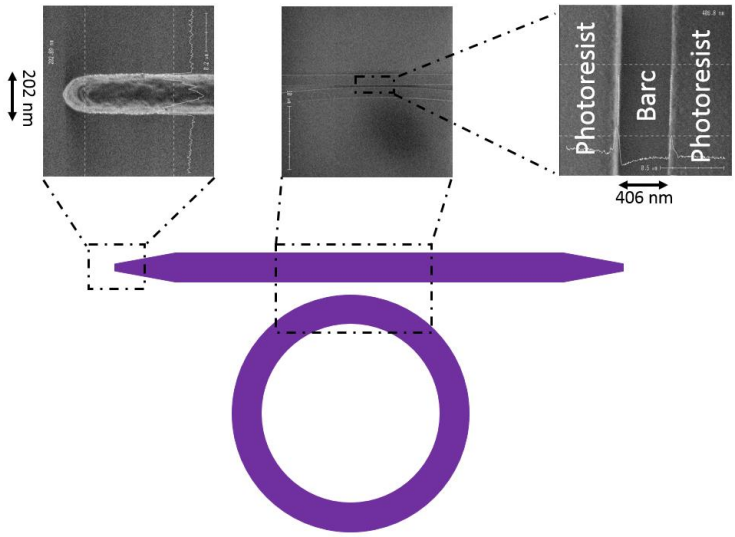

Figure 48- Top view scanning electron microscope image of a 400-nm-gap pattern and a 200-nm-tip after DUV lithography and development.

Another parameter that can affect the dimensions of the patterns obtained after the lithography is the focus. This parameter is very useful especially when a non-flat topology is present on the wafer. As this was not our case, the focus was kept to a neutral (zero) nominal setting.

Etching

The etching of the film is finally a key step to get high quality factor resonators and low propagation loss waveguides because the etching process defines the roughness of the sidewalls and the related device scattering losses.

The silicon nitride can be selectively removed by a wet etching step using a selective wet-etchant. In this case, the resulting roughness can be very low or even negligible. However, this etching approach is isotropic, thus making it extremely difficult to properly control the etching so as to preserve the desired opto-geometrical characteristics of the desired optical components (*i.e.*, the waveguide dimensions,

aspect ratio, and a void-free encapsulation). This is the reason why a plasma-assisted dry etching is more suitable to get vertical waveguide sidewalls. Various plasma etching reactors exist such as a chemically assisted ion beam etching reactor, reactive ion etching, inductively coupled plasma reactor and electron cyclotron resonance reactor. In our fabrication process, we used inductively coupled plasma reactors (Figure 49).

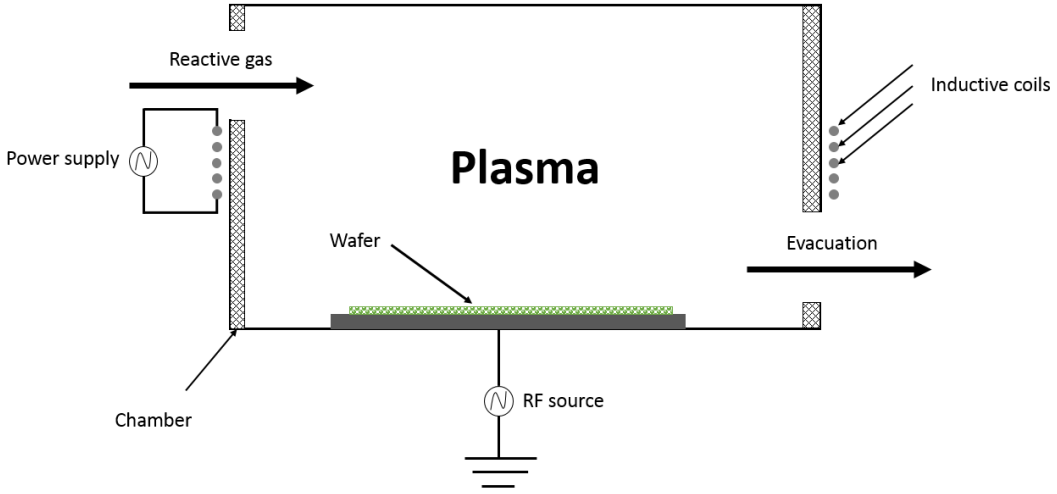

Figure 49- Schematic of an inductively coupled plasma etching reactor.

The uniformity, directivity, as well as the etching rate depend on the temperature, the pressure, the DC and RF powers, and the chemical environment, the latter resulting from the chosen rate and chemical composition of the gases introduced in the reaction chamber. The silicon nitride film reacts with the fluorine atoms according to the following chemical reaction:

$$Si_3N_4 + 12F \rightarrow 3SiF_4 + 2N_2. \quad (4.3.1)$$

In the plasma reaction, *Tetrafluoromethane* CF_4 is used as a source of fluorine [89]. Fluorine can be split from CF_4 by adding oxygen according to the chemical reaction:

$$2CF_4 + O_2 \rightarrow 2COF_2 + 2F_2 \quad (4.3.2)$$

The fluorine molecule (F_2) is then split into two atoms of radicals fluorine (F) by the plasma. However, once F_2 molecules are split into $2F$ atoms, the latter can react with

the CF_4 under the plasma and leads to C_xF_y polymers through diffusion and a repeated secondary reaction according to [90]:

$$F + CF_4 \rightarrow CF_3 + F_2 \quad (4.3.3)$$

$$CF_3 + CF_4 \rightarrow C_2F_5 + F_2 \quad (4.3.4)$$

Moreover, small particles of solids are also formed and can have undesirable consequences such as affecting the plasma properties and the structure. In fact, H that reacts with CN atoms has to be added to form HCN and reduce the polymer thickness [91]. The reaction may occur as follows:

$$H + CN \rightarrow HCN \quad (4.3.5)$$

$$Si_3N_4 + H + CF_4 \rightarrow HCN + SiF_4 \quad (4.3.6)$$

$$Si_3N_4 + CHF_x \rightarrow HCN + SiF_x \quad (4.3.7)$$

The reduction of etching-related polymer formation on the surface has been proven by Park et al. [92]. Another advantage of adding hydrogen in the reaction is to allow the formation of HCN which effectively removes nitrogen (N), one of the major limitations for Si_3N_4 etching [93]. The hydrogen is added by reacting the difluoromethane (CH_2F_2) with oxygen. According to [91] when O_2 is added in hydrogen-containing fluorocarbon plasma, the following reaction will occur:

$$CH_xF_y + O \rightarrow H + CO \text{ or } COF_2 + F. \quad (4.3.8)$$

Eventually, the chemistry used for the dry etching in order to pattern the different architectures on the Si_3N_4 film shown previously is: CF_4-CH_2F_2-O_2 where the combination of CF_4/O_2 is the source of the fluorine (reaction 4.3.2) to etch the silicon nitride (reaction 4.3.1). And the combination of CH_2F_2 /O_2 is the source of hydrogen (reaction 4.3.8) to reduce the polymer thickness and remove the N atoms from the substrate surface.

At the beginning, we used silicon dioxide as a hard mask for the etching, thus an additional layer of silicon dioxide was deposited on top of the silicon nitride prior to the resist spin-coating and photolithography. This silica layer was etched using the

resist as a hard mask before stripping it and etching the silicon nitride film using the silica as a hard mask (Figure 50).

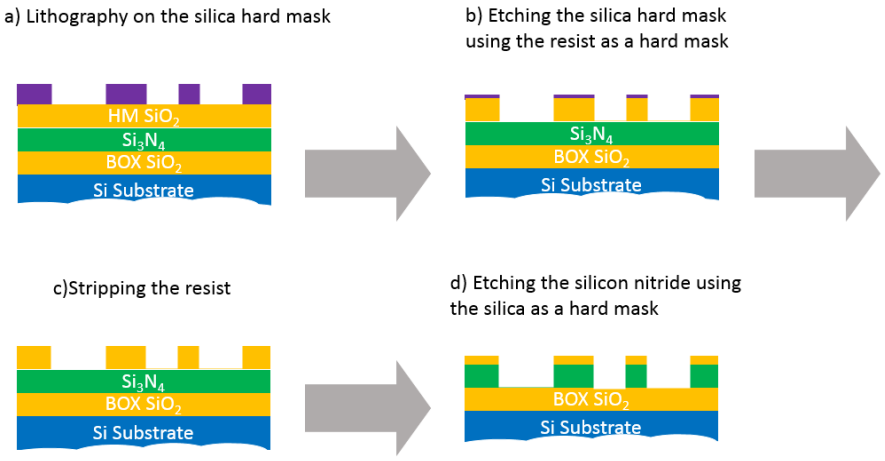

Figure 50- Silicon nitride etching process with a silica hard mask.

Even if the silica hard mask was used in order to increase the selectivity of the etching process, the sidewalls of the resulting waveguide appeared to be extremely rough (10 nm) according to the SEM picture analysis (Figure 51).

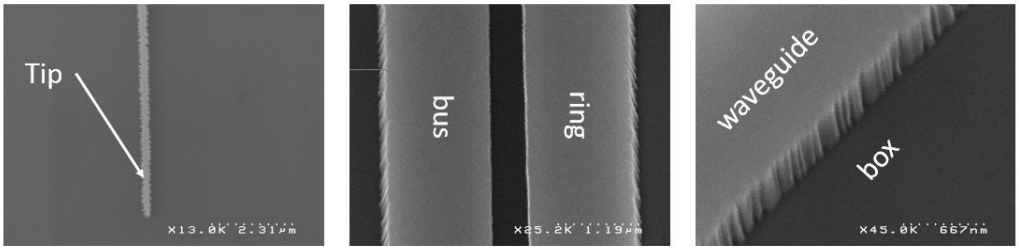

Figure 51- Scanning electron microscope of a (left) 200-nm-wide inversed coupler tip, (middle) 400-nm-space and (right) waveguide edge etched with a silicon dioxide hard mask. The observed structures consist of Si_3N_4 with a residual SiO_2 hard mask.

The roughness of the waveguide scatters the light and decreases the quality factor of the Si_3N_4 resonators. For this reason, we then tried to directly etch the silicon nitride using the photoresist as a hard mask. As we can see in the figure 52, the roughness has been reduced dramatically by at least a factor of 3.

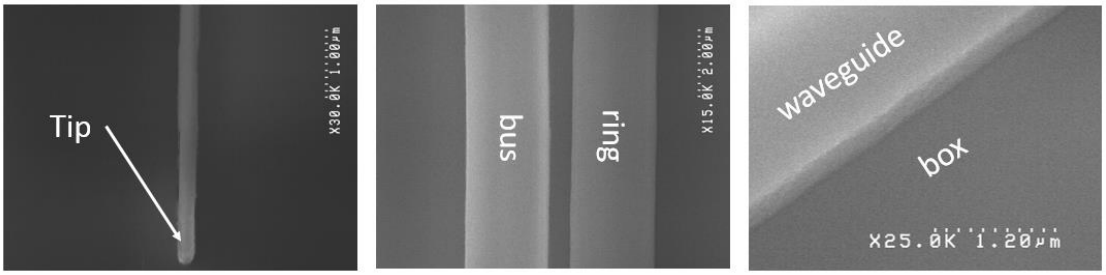

Figure 52- Scanning electron microscope of a (left) 200-nm-tip, (middle) 400-nm-space and (right) waveguide edge etched with the resist as a hard mask. The patterns consist of Si_3N_4 after stripping the resist.

Before encapsulation, focused ion beam (FIB) milling is used to etch the waveguides in the coupling region of a resonator to check the cross section of the waveguide using a scanning electron microscope (Figure 53) and measure the sidewall angle. An acceptable sidewall slope of 5° is found.

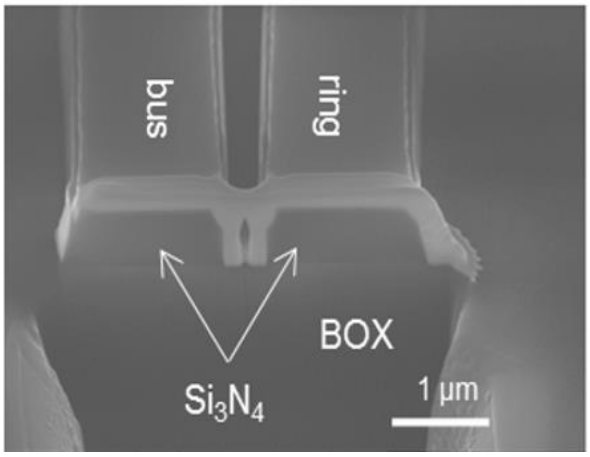

Figure 53- Scanning electron microscope of a focused ion beam etched silicon nitride waveguides.

A 20-second SiO_2 overetch was estimated to consume between 20 nm and 30 nm so as to ensure that the silicon nitride has been totally removed across the 200-mm-silicon wafer. The Si_3N_4 etch rate was estimated to be 110 nm/minute, while the etching selectivity of the resist against the nitride layer is 1:1.5. Hence, a residual 300 nm resist was still present on the Si_3N_4 devices after the etching process, and was subsequently removed by an O_2 plasma.

4.4. Encapsulation of the Si_3N_4 devices

The quality of the interface between the silicon nitride waveguide and the cladding is critical to obtain low propagation losses, resonators with high quality factors and

mitigate the risk of device failure under high power optical test. In fact, the conformity of the encapsulation is key to avoid the void formation in the coupling region, which is one of the main causes of device failure. The silica can be deposited by either plasma enhanced chemical vapor deposition (PECVD) or high density plasma enhanced chemical vapor deposition (HD-PECVD). Thanks to its inherent physical-chemical process providing concurring phases of etch/passivation/deposition, HD-PECVD has the capability to fill the small gaps very well, and the quality of the silica is closer to that of thermal oxide. Nevertheless, the high-density plasma may damage the top surface of the waveguide due to incoming ion bombardment, thus increasing the propagation losses. Consequently, after stripping the resist and before the HD-PECVD encapsulation, a thin layer of silica, typically in the order of a few tens of nanometers, is deposited by low rate PECVD (140 nm/min) so as to provide a proper physical layer protection from the bombardment of the high-density plasma (Figure 54).

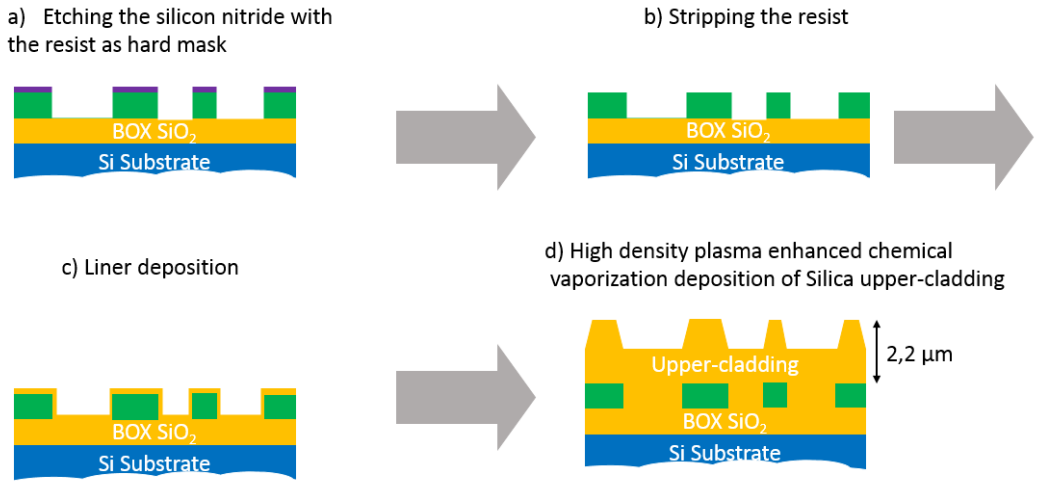

Figure 54- Silicon nitride etching, stripping, and encapsulation process.

First, a 40 nm-liner of silica is deposited at 400 °C by using tetraethyl orthosilicate (TEOS) with nitrogen as a carrier to protect the top of the silicon nitride from the subsequent HD-PECVD silica deposition. The reaction occurs as follows:

$$Si(OCH_2CH_3)_4 \rightarrow SiO_2 + 4C_2H_4 + 2H_2O \qquad (4.4.1)$$

Note that the TEOS ($Si(OCH_2CH_3)_4$) is stored as a liquid but used as a gas phase reactant.

After the liner deposition, a 2.2-µm-thick layer of silica is deposited via HD-PECVD at 400 °C with silane and oxygen as precursors. The reaction occurs as follows:

$$SiH_4 + 2O_2 \rightarrow SiO_2 + 2H_2O\ . \tag{4.4.2}$$

Note that the carrier used in the HD-PECVD is the argon (Ar) and the deposition reactor is an inductively coupled plasma reactor.

As a summary, the complete process of the annealing- and crack-free silicon nitride process for high-power nonlinear photonics is presented in figure 55.

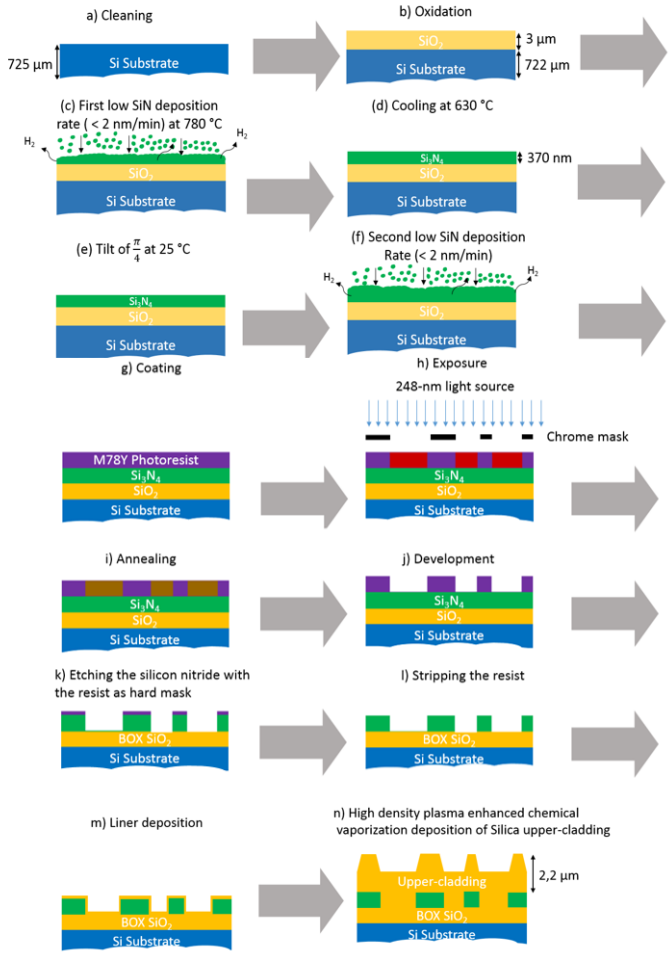

Figure 55- Complete process of the annealing-free and crack-free 800 nm thick silicon nitride.

This full deposition/ patterning/ etching/ encapsulation process of Si_3N_4 devices allowed us to produce high quality, crack-free devices, with limited material

absorption loss, relatively smooth and close to vertical sidewalls, and void-free encapsulation so as to mitigate device failure under test.

4.5. Conclusion

In this chapter, we described the process flow to obtain crack-free silicon nitride films without resorting to a long high-temperature annealing step, while still featuring sufficiently low hydrogen content. More specifically, all the different main technological steps that have been developed and optimized, including the oxidation, the silicon nitride deposition, the silicon nitride patterning, and the encapsulation have been reviewed in details in this chapter, providing the reader with the accurate and reliable methodology of our fabrication process flow. By using this process, silicon nitride devices with low propagation losses suitable for frequency comb generation could be achieved, as will be discussed in the next chapter.

In the next chapter, the linear and nonlinear characterization of the devices, the design of which was presented in chapter 3 and fabricated as detailed in this chapter 4 will be analyzed and discussed.

CHAPTER 5

LINEAR AND NONLINEAR CHARACTERIZATION OF SI_3N_4 INTEGRATED OPTICAL DEVICES

We presented in chapter 4 a method to grow high quality Si_3N_4 films and subsequently realize optical devices such as waveguides and microring resonators. We assess in this chapter both the linear and nonlinear optical properties of these devices. The first parameter that needs to be critically controlled for efficient nonlinear devices is the effective length. The latter, which determines the distance along which the nonlinear interaction effectively occurs in the waveguide depends on the propagation losses. We first present the propagation losses and the quality factor measurements performed at CEA-LETI of our components as well as the waveguide linear dispersion measurements performed at Denmark technical university (DTU). Then, we report the measurement of the nonlinear index via self-phase modulation and four mixing experiments performed at DTU and Lyon nanotechnology institute (INL) on our Si_3N_4 waveguides. Finally, we present and discuss the generation of frequency combs as well as high-order harmonic generation in Si_3N_4 microring resonators performed at DTU. Concerning the optical test I took part in all the aforementioned measurements.

5.1. Propagation loss measurements

There are several ways to measure integrated waveguide propagation losses. In the first place, the cut-back method is used to measure the total insertion losses (including both coupling losses and propagation losses) on a series of waveguides with different lengths. The propagation losses are inferred by dividing the difference of the total insertion losses by the difference of the lengths. The cut-back method considers that the coupling losses are the same for all the measured waveguides. Consequently, to average out the impact of all kinds of defects which may influence the loss of each individual waveguide, it is necessary to undertake the measurements on a high number of waveguides (5 waveguides in our case).

Alternatively, the propagation losses can also be inferred from the quality factor of the resonator as shown in the equation 3.1.19. This method is eligible when the ring radius is large enough so that the bending losses can be ignored. Another method is to measure the scattered light from the top of the waveguide by an infrared camera

and infer the propagation losses from the intensity decay slope of the scattered light [94].

We first present the propagation loss measurements using the cut-back method. An automated prober station is used to test different waveguides across the whole 200 mm wafer. In this set-up, light was injected via 1-dimensional grating couplers with -7 dB coupling losses per coupler (figure 56).

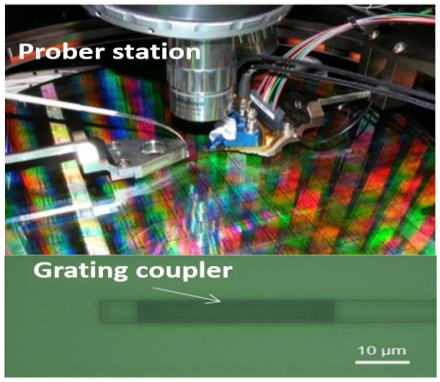

Figure 56- Automated prober station (Top). Tov view optical microscope image of a grating coupler (bottom).

We derived an average propagation loss of 1.7 dB/cm at 1550 nm for waveguides with cross-section dimensions (w × h) of 750 nm × 730 nm, which correspond to a single-mode waveguide (normal dispersion). The total insertion losses of several waveguides with different lengths were measured according to the cut-back method and the propagation loss of the fundamental transverse electric polarized mode was inferred from the slope of the total insertion loss (in dB scale) as a function of the waveguide length (see examples of these measurements for different dies on Figure 57).

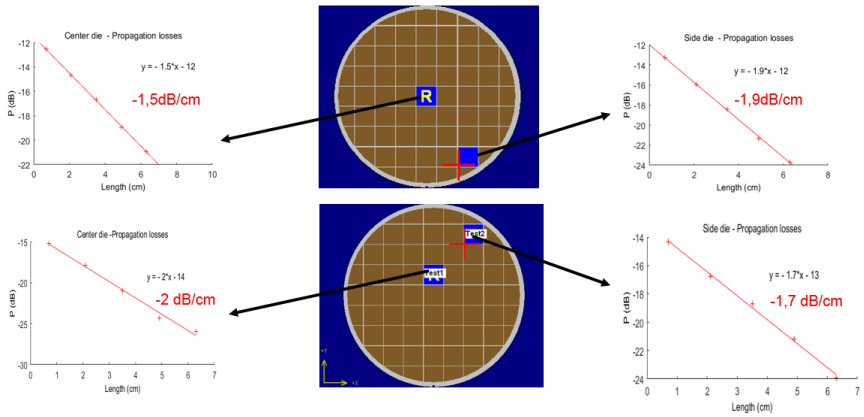

Figure 57- Cross-die and cross wafer propagation loss measurements with the automated prober via the cut-back method for the waveguide of 740 nm *x* 750 nm cross-section dimensions at 1550 nm and for TE polarized light.

These loss measurements were performed on randomly chosen dies and wafers to ensure that the film is crack-free everywhere on each of the 200 mm wafers. The measurements were averaged out across 20 dies of different wafers.

Concerning the waveguide with anomalous dispersion (i.e. larger widths), we did not have different lengths available on the chip, so that the propagation losses were inferred from the quality factor measurement of the micro-ring resonators instead. The spectral transmission was recorded for 112 um radius microring resonators with a precision of 1 pm while scanning across the resonances (Figure 58). The power used in our experiments was 1 mW (200 µW in the bus waveguide) and the light was collected via a photodetector, using for the laser and detection an Agilent 8614B equipment.

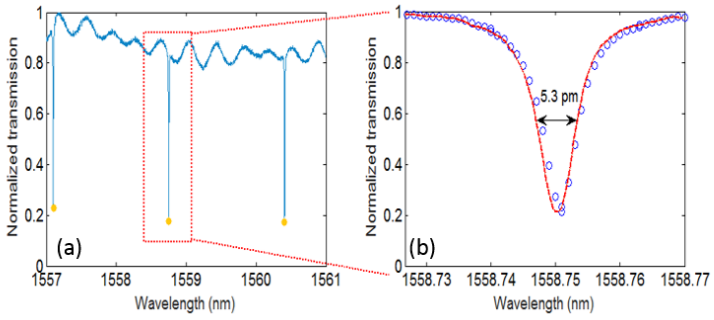

Figure 58-Normalized transmission of a 112-µm radius silicon nitride ring with a cross section of 1500 nm x740 nm. (the space between the ring and the bus waveguide is 300 nm)

The loaded quality factor for the ring formed from a waveguide with a cross section of 1500 nm x740 nm (the space between the ring and the bus waveguide is 300 nm) was measured to be 3×10^5 at around 1558nm which is equivalent to a propagation loss of 0.5 dB/cm (according to the equation 3.1.19 by replacing by replacing Q_L with $Q_i/2$ and Q_i is calculated according to the eauqtions 5.2.1 or 5.2.2 depending if the resonator is under-coupler or overcoupled.).

As mentioned in chapter 4, the LPCVD grown silicon nitride film is not free of hydrogen. The absorption caused by the residual N-H bonds is provided by the spectral dependence of the intrinsic quality factor (Q_i) (see figure 59) inferred from the measured loaded quality factor for a Si_3N_4 micro-ring resonator with 1.4 µm waveguide width (and ring/ bus waveguide gap of 300 nm). The intrinsic quality factor is calculated following the equation:

$$Q_i = \frac{2Q_L}{1+\sqrt{T_{min}}} \text{ for under-coupled resonators} \quad (5.2.1)$$

$$Q_i = \frac{2Q_L}{1-\sqrt{T_{min}}} \text{ for over-coupled resonators} \quad (5.2.2)$$

where T_{min} is the transmission at the resonances. In figure 59 the equation 5.2.1 is used since the resonator is under-coupled. The coupling regime is determined depending on the extinction ratio variation with space between the ring resonator and the bus waveguide. More precisely, if the extinction ratio increases with the space between the resonator and the bus waveguide, we can deduce that the resonator is over-coupled (approaching critical coupling when the space increases). Moreover, if the extinction ratio decreases with the space between the resonator and the bus waveguide this means we are moving away from the critical coupling and we are in the under-coupled regime. The intrinsic quality factor roughly increases by a factor of 2 while moving away from the N-H overtone absorption peak (near 1520 nm), indicating the presence of residual N-H bonds in our film. The difference between the losses at 1550 nm (where $Q_i = 350{,}000$) and those at 1520 nm (where $Q_i = 190{,}000$) can thus be estimated to be 0.9 dB/cm (according to the equation 3.1.19 by replacing Q_L by $Q_i/2$ and using the eqution 5.2.1 to deduce Q_i from the measured Q_l because we are in the under-coupled regime).

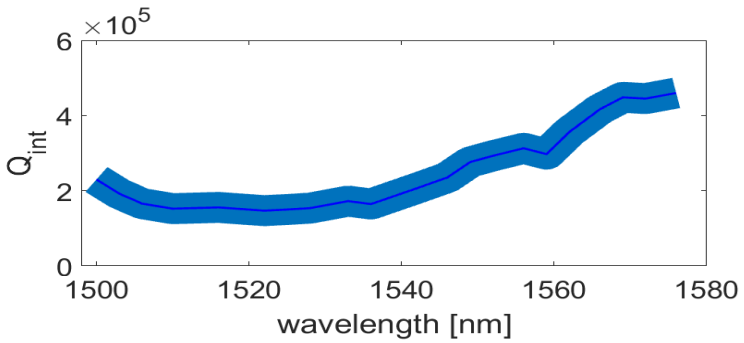

Figure 59- Intrinsic quality factor as a function of wavelength for an annealing-free silicon nitride microring resonator (waveguide width equal to 1.4 µm, and bus-ring gap equal to 300 nm). The darker colored line shows the mean value and the brighter shadowed areas illustrating the standard deviation of the measurements.

This additional loss due to the residual N-H absorption for our annealing-free Si_3N_4 growth process is comparable to the value (0.6 dB/cm) inferred for high-temperature annealed Si_3N_4 waveguides [57], and, as shown below, it does not preclude the generation of frequency combs in the C-band.

5.2. Dispersion measurement of Si_3N_4 waveguides

As mentioned in chapter 3, the dispersion of the waveguide constituting the resonator has to be anomalous for sustaining the generation of frequency combs. From the equation 2.4.14, we can see that the free spectral range depends on the dispersion and consequently changes with the optical frequency. According to [95], [96] the relation between the dispersion, the free spectral range and the resonance frequency is as follows:

$$\omega_\mu = \omega_0 + D_1\mu + \frac{1}{2}D_2\mu^2 + \frac{1}{6}D_3\mu^3 + \frac{1}{24}D_4\mu^4 + \cdots \qquad (5.2.1)$$
$$= \omega_0 + D_1\mu + D_{int}(\mu).$$

where ω_μ is the $\mu - th$ resonance angular frequency relative to the resonance frequency ω_0 and $D_1/2\pi$ is the free spectral range around ω_0 (similar to that given by equation 3.1.20, but defined here in frequency). The second order element D_2 is the dispersion parameter of the resonator (see equation 2.3.10) around ω_0 and is anomalous when $D_2 > 0$. D_{int} is the integrated dispersion of the microcavity, which includes all the higher-order terms in the Equation 5.2.1. Using the equation 5.2.1, the dispersion can be inferred from the spectral transmission of the resonator but a

high precision is needed. In fact, the dispersion of a resonator with a cross section of 1.5 µm-wide × 730 nm-thick is measured for our devices by scanning the wavelength of an external cavity diode laser (ECDL) light while recording the device transmission and two calibration traces from a fiber loop cavity and a high-finesse free space cavity with a free spectral range of 171MHz and 175MHz, respectively (Figure 60).

In the dispersion measurement, light from the ECDL is coupled into the microresonator. The ECDL wavelength is swept continuously and the resonator transmission is recorded by a photodiode. In order to achieve high accuracy in measuring the resonator FSR, the laser wavelength must be calibrated. This is achieved by using a high-Finesse free-space cavity which provides one marker every 100 MHz of the laser scan. The analog signal from each photodiode used is sampled by an oscilloscope. Each trace contains 100 million points, thereby providing very good resolution. Simultaneously, a part of the laser signal passes through a fiber cavity which is made of a loop of standard single-mode fiber. For each microresonator dispersion measurement, the dispersion of the fiber cavity is measured and compared to the known value of standard single-mode fibers. In this manner, the measurement accuracy is verified every time the measurement is performed.

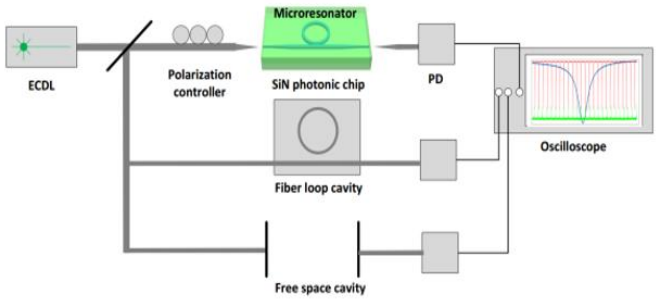

Figure 60- Experimental setup used for the dispersion measurement

When the dispersion is anomalous, the free spectral range increases with the frequency (i.e. decreases with the wavelength). Figure 61 depicts the dispersion D_{int} measured relatively to the central angular frequency (wavelength) of 192 THz (1560 nm) for a Si_3N_4 300µm radius ring resonator with a 1.5µm width. A fit of the

measured dispersion gives an anomalous dispersion value of $\frac{D_2}{2\pi} = 511\ KHz$ at 1580 nm which is equivalent to a dispersion of 29 ps/nm/km.

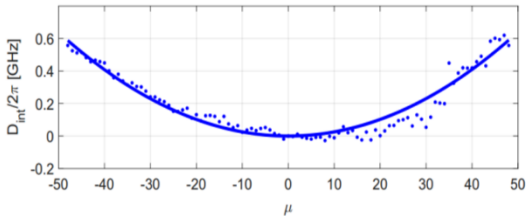

Figure 61- Dispersion measurement of the TE mode of a ring resonator with 200 µm radius and 1.5 µm width.

This value compares well with our finite element modeling of the dispersion which gave us an anomalous dispersion estimate of 18 ps/nm/km at the same wavelength (Figure 24). Note that the values of simulated and measured dispersion are in agreement with the simulated dispersion of similar annealed Si_3N_4 waveguides (1.65-µm-wide × 730-nm-thick) presented in [16], [22].

5.3. Nonlinear index measurements

The nonlinear parameter of a single mode silicon nitride waveguide with a cross-section of $750\ \text{nm} - \text{width}\ \times\ 730\ \text{nm} - \text{heigth}$ is measured by performing four-wave mixing measurements between slightly spectrally detuned continuous-wave pump and probe signals injected into a 7 mm-long single-mode Si_3N_4 waveguide via grating couplers (Figure 62).

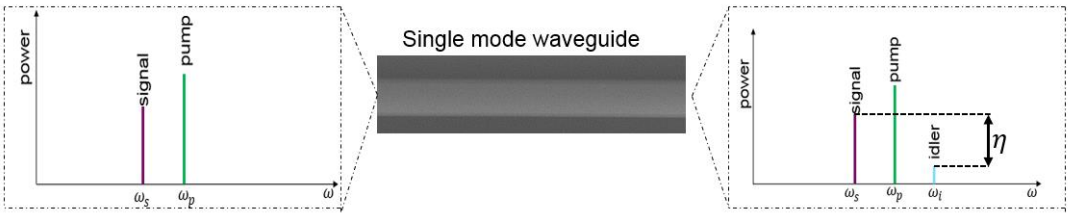

Figure 62- Degenerate four-wave mixing experiment in a single mode silicon nitride waveguide.

For phase matched signals (which is a correct assumption when the two signals are close in wavelength and/ or the waveguide length is relatively short), the four-wave mixing conversion efficiency within our waveguide follows the equation:

$$\eta = \frac{P_{idler}}{P_{signal}} = (\gamma P L_{eff})^2 \qquad (5.3.1)$$

where P is the coupled pump power and γ is the nonlinear waveguide parameter. The latter is related to the nonlinear index n_2 through the expression $\gamma=\frac{\omega n_2}{cA_{eff}}$, where ω is the angular pump frequency, c is the speed of light and A_{eff} is the mode effective area. The effective length L_{eff} is given by $L_{eff} = \frac{1-e^{-\alpha.L}}{\alpha}$. Depending on the linear propagation loss α, L_{eff} converges towards $L_{max}=1/\alpha$ as a function of the waveguide length (L). In our experiment, the dispersion effects can be neglected 5.3.1due to the small pump-probe detuning (1 nm) and dispersion of the waveguide (-315 ps/nm/km by finite element calculations). More quantitatively, by taking into account only the second order dispersion, the phase mismatch can be calculated following the equation:

$$\Delta\beta = -\frac{1}{2\pi c}\lambda_p^2 D(\lambda_p)\Omega^2 \qquad (5.3.2)$$

where $\Omega = \omega_s - \omega_p$ is the frequency difference between the signal and the pump and λ_p is the pump wavelength. In our case, the phase mismatch ($\Delta\beta \times L$) at the end of the waveguide is equal to 4.4×10^{-5}.

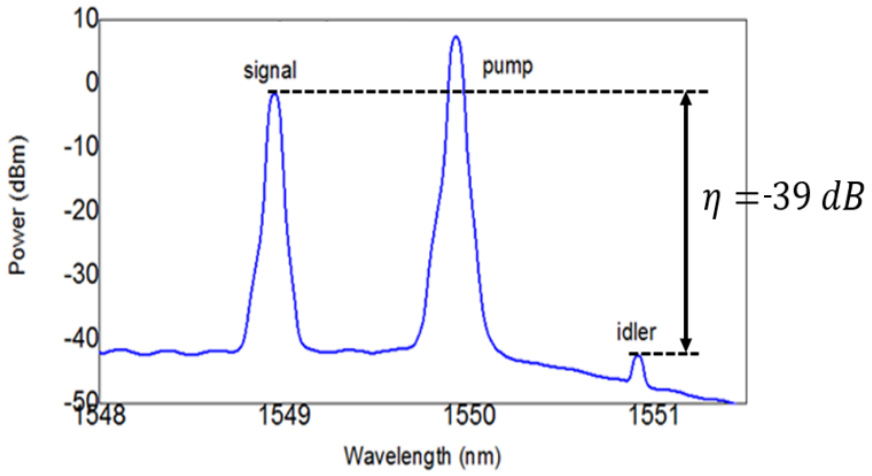

Figure 63 - Idler-signal degenerate continuous-wave four-wave mixing obtained in the 7mm long silicon nitride waveguides for a coupled pump power of 28dBm.

From the experiment presented in figure 63, we can infer that the continuous wave conversion efficiency is of -39 dB (difference between signal and idler) for $L_{eff} = 0.63$ cm (provided by a 7mm long straight single mode Si_3N_4 waveguide) and a coupled pump power of 28 dBm. Note that a 20 dB attenuator is added at the output

of the waveguide before recording the spectrum of Figure 63, in order to protect the optical spectrum analyzer. The spectrum is normalized with respect to the input/output grating coupler losses. From these measurements and Equation 5.3.1, we can derive the nonlinear parameter γ, which is equal to 2.8 $W^{-1}m^{-1}$ and deduce the nonlinear index, which is equal to $3.6 \times 10^{-15} cm^2.W^{-1}$ (taking $A_{eff} = 750\text{ nm} \times 730\text{ nm}$). The probe and pump signals are multiplexed in a short-length (1 meter) single-mode fiber before entering into the silicon nitride waveguide, hence we can consider that the contribution of the fiber in the four-wave mixing is negligible. The nonlinearity of the silicon nitride obtained using the process presented in chapter 4 is slightly higher than the one obtained when a 1200 °C annealing is applied ($2.5 \times 10^{-15}\ cm^2.W^{-1}$) as in reference [22].

5.4. Continuum generation by self-phase modulation in Si_3N_4 waveguides

Supercontinuum generation has given rise to a wide variety of research, regarding both the approaches to generate it as well as its target applications such as chemical sensing, medical imaging, or high-throughput telecommunications [97]. For selected applications, even moderate-bandwidth (of 60 nm) supercontinua are enough. We refer to these as continuum sources. The intensity-dependent refractive index in nonlinear waveguides leads to self-phase modulation upon the propagation of short optical pulses and the generation of spectral continuum via its Kerr nonlinearity. As long as there is no nonlinear absorption loss in the waveguide, the maximum nonlinear phase shift accumulated by a pulse of peak power P, after its propagation along a waveguide with a nonlinear parameter γ and an effective length L_{eff} is as follows:

$$\Delta\varphi_{max} = \gamma P L_{eff} \tag{5.4.1}$$

By using the measured propagation losses, we estimate L_{eff} to be 1.43 cm for our 2.1 cm-long single-mode waveguides, i.e., 56% of L_{max} (2.55 cm), meaning that by using longer waveguides we could get more self-phase modulation and a wider spectral broadening. The efficiency of the continuum generation is naturally limited by linear and nonlinear losses. In our case, the latter such as two- or three-photon

absorption are negligible, as attested by the linear transmission of our waveguides as a function of pump power, even at high power values.

The phase constant of a wave propagating in the z direction is given by:

$$\varphi(t) = 2\pi f t - kz \tag{5.4.2}$$

where the carrier frequency f of the pulse is just the derivative of the phase constant in the case of a continuous wave or an un-chirped pulse. If the incident optical power changes in time, the refractive index takes the form:

$$n = n_0 + n_2 I(t) \tag{5.4.3}$$

and the propagation constant takes the form:

$$k = \frac{2\pi}{\lambda} n = \frac{2\pi}{\lambda} n_0 + n_2 I(t) \tag{5.4.4}$$

When a pulse passes through the silicon nitride waveguide, the derivative of the phase constant is no longer f but the term $-\frac{n_2}{\lambda}\frac{\partial I}{\partial t}$ has also to be added. In fact, the material intensity-dependent nonlinear index produces a chirp in the pulse, which is associated with blue-shifted spectral components on the trailing edge and red-shifted spectral components on the leading edge of the optical pulse envelope.

As the process accumulates along the waveguide, the pulse gets spectrally broadened, giving rise to a frequency continuum that can be measured at the waveguide output.

The grating coupler bandwidth is around 40 nm so edge-coupling (1.2 dB coupling loss per facet) via inverted tapers was used in order to perform extensive nonlinear optical characterization over a large wavelength span in the 1.55 μm region (Figure 64). To obtain clean facets and a high coupling efficiency, the silica was etched one micron away from the reversed taper. Moreover in order to avoid that the lensed fiber touches the substrate when the fiber is approached to the chip, the silicon substrate was also etched by 100 μm in depth over 850 μm from each side before dicing the wafer. The facet is tilted by 8° to avoid the back-reflections while butt-coupling light in the bus waveguide.

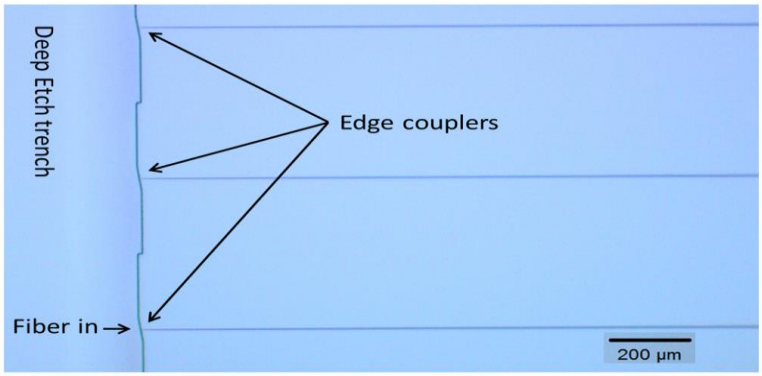

Figure 64- Edge-coupling via inverted tapers tips of 160 nm in width ensuring coupling over a wide spectral window for nonlinear tests. Deep-etch trench profiles (including 8° off-normal coupling facets) are used to reduce back-reflections

Using an external fiber-based laser followed by an erbium-doped fiber amplifier (EDFA), TE-polarized optical pulses of 2 ps duration with peak powers ranging from a few to hundreds of Watts at a repetition rate of 20 MHz were injected into the single-mode 2.1 cm-long silicon nitride waveguides (750 nm × 730 nm cross-section, α=1.7 dB/cm). No fusing of the waveguides nor degradation of the spectral broadening over time was observed. The output spectrum thus measured experimentally for increasing coupled peak power is plotted in Figure 65 (a).

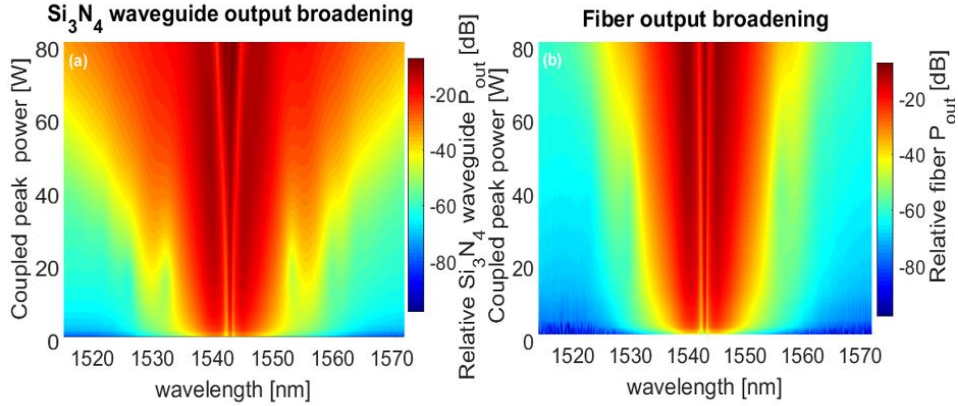

Figure 65- Spectral broadening of picosecond pulses via Kerr self-phase modulation (SPM) leading to the generation of a frequency continuum between 1515 - 1575 nm. (a) Spectral broadening at the Si_3N_4 waveguide output. (b) Spectral broadening measured at the fiber output (i.e., before the Si_3N_4 waveguide input).

As shown on this figure, by increasing the coupled peak pump power, the Kerr nonlinearity can be leveraged into a SPM process capable to generate a wide-spanning continuum of new optical frequencies around the 1543 nm pump wavelength. Note that on this plot, there is a non-negligible contribution of SPM arising in the EDFA used to amplify the pulsed laser signal as well as in the

subsequent 7 m-long silica fiber crossed by the pump pulses before they reach the waveguide under test. The contribution of the EDFA to the spectral broadening is independent of the pump power though, since the latter is varied through the use of an attenuator placed after the amplifier. To clarify the relative contribution of the 7 m-long input fiber and the Si_3N_4 waveguide to the overall self-phase modulation response, we also measured the spectrally broadened spectrum at the end of the input fiber for the same range of pulse peak power, before injection into the waveguide as shown in Figure 65 (b). The pulse goes through seven-meter-long single-mode silica fiber with a nonlinear refractive index $n_2 = 2.52 \times 10^{-16} cm^2.W^{-1}$. To calculate the contribution of the optical fiber in the continuum generation, the normalized spectral broadening as a function of the coupled peak power is calculated from the experimental spectra measured both before and after the waveguide (see Figure 66) as per:

$$\Delta\lambda = \left(\frac{\int S(\lambda)(\lambda-\lambda_0)^2 d\lambda}{\int S(\lambda) d\lambda}\right)^{\frac{1}{2}} \tag{5.4.5}$$

where $S(\lambda)$ is the spectrum intensity as a function of wavelength and λ_0 is the central wavelength of the pulse.

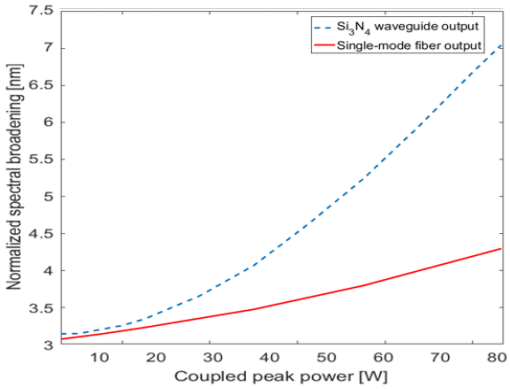

Figure 66 - Comparison between the normalized spectral broadening at the silicon nitride output and the single-mode fiber output (i.e. before the silicon nitride waveguide).

By taking the ratio (for 80 W) of the differences between the maximum and the minimum of the two curves we found that 29% of the broadening effect is in the fiber, which is consistent with the difference (×10) between the nonlinear index of the silicon nitride and silica, the effective area difference of the fiber and waveguide geometries, considering also that a long fiber (7 meters) is used before entering in the

silicon nitride waveguide. Indeed, to correlate the measured fiber contribution in the spectral broadening to that theoretically expected, we can estimate, as per equation (5.4.6) below, the ratio of the two SPM induced maximum phase shifts arising from the 7-meter-long fiber and from the silicon nitride waveguide, respectively:

$$\zeta = \frac{\gamma_{SiO2} P L_{eff\_SiO2}}{0.758 \times \gamma_{SiN} P L_{eff\_SiN}} \quad (5.4.6)$$

The factor 0.758 in the denominator is used to take into account the edge coupler loss (-1.2 dB) that decreases the maximum phase shift arising from the Si_3N_4 waveguide, whereas no power loss is considered across the propagation in the fiber (P is taken as the same value at the numerator and denominator). Similarly, we assumed that the effective length $L_{eff\_fiber} = L_{fiber}$ because of the almost negligible propagation losses of the single mode fiber. Considering gamma_SiO2, and gamma_SiN equal to 5.10^{-4} $w^{-1}.m^{-1}$ and 2.8 $w^{-1}.m^{-1}$, the ratio of equation 5.4.6 is 31 % which is consistent with the spectral broadening ratio inferred from the measurement of figure 66.

These measurements show that the Kerr nonlinearity of Si_3N_4 waveguides could be used to produce SPM in such waveguides so as to generate a 60 nm-spanning wavelength continuum across the C-band capable to provide hundreds of new available optical frequencies, for high data transmission, for instance.

5.5. Frequency comb generation in silicon nitride microrings

The combination between the four-wave mixing processes within the nonlinear resonator and the optical parametric oscillation results in the generation of Kerr frequency combs, as reported in this section.

The top view images recorded by an optical and a scanning electron microscope for an annealing-free silicon-nitride-on-insulator microring with a 56-µm radius are shown in Figure 67.

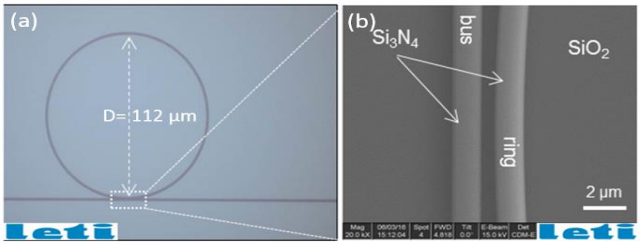

Figure 67- (a) Optical microscope and (b) scanning electron microscope images of the ring and coupling region.

The cross-section dimensions (1.5 µm-wide × 730 nm-thick) of the ring waveguide ensure that GVD is anomalous at the 1569 nm pump wavelength. The intrinsic quality factor of the microring, which is here separated by a 350 nm gap from the bus waveguide, exceeds 580,000 (Q_I=300000). A relatively smooth native line spacing (~406 GHz) frequency comb spanning across about 800 nm between 1300 nm - 2100 nm is obtained for ~1 W TE-polarized continuous-wave power (Pin) coupled in the bus waveguide (Figure 68).

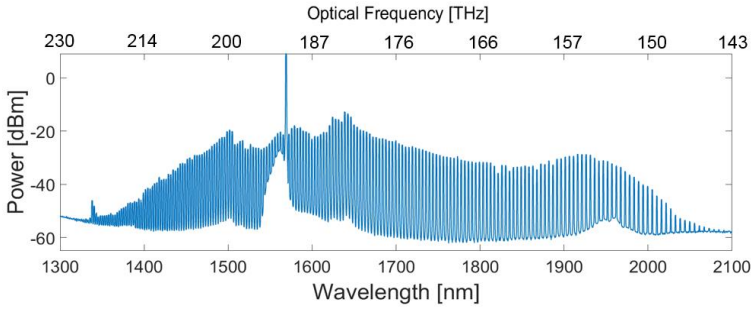

Figure 68- Comb generation using annealing-free silicon nitride on insulator. A 800-nm-spanning comb generation using a 56-µm-radius Si_3N_4 microresonator for coupled cw power P_{in} ~ 1 W.

This power value is comparable to the power required (2 W) to fill the entire comb span using high-temperature annealed Si_3N_4 rings with a loaded quality factor of 100,000 (an intrinsic quality factor of 200,000) [16] and to the pump power (3 W) used to generate an optical frequency comb in annealed Si_3N_4 ring resonators that have similar quality factor and cross-section dimensions [98]. A spectrum recorded for a lower power, Pin ~300 mW, i.e., well above the oscillation threshold, is also shown in Figure 69.

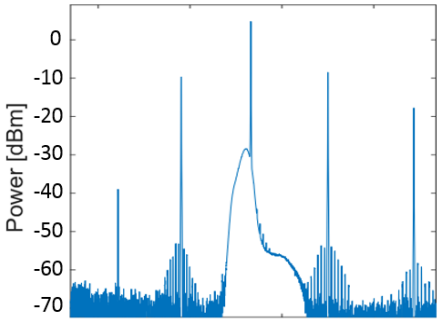

Figure 69- Comb spectrum for P_{in} ~ 300 mW.

The comb spacing is wider in this case, as dictated by the spectral gain of degenerate four-wave mixing imposed by the device GVD.

In order to measure the threshold power for optical parametric oscillation (OPO), the device was pumped with increasing power levels coupled to the bus waveguide. The laser wavelength was scanned across a resonance at 1570 nm. The chip output light was passed through a short pass filter with a cut-off wavelength of 1560 nm that blocks the pump light with an extinction ratio of 60 dB and was then detected by a photodiode.

The peak power of the filtered short wavelength OPO signal at each power coupled to the bus waveguide shows that the measured signal exceeds the noise floor (of -50 dBm) above a threshold power of ~ 83 mW. The threshold power in the bus waveguide can be roughly estimated (Neglecting the influence of the coupling non-ideality and considering being under the phase-matching condition) using the equation 2.4.15, where L and λ_p, are the cavity length (350 μm) and pump wavelength (=1565 nm), and Q_c and Q_L are the coupling ($5.8x10^5$) and loaded ($2.9x10^5$) quality factors of the micro-resonator, respectively. The calculated threshold power is 73 mW, which is comparable with the measured one.

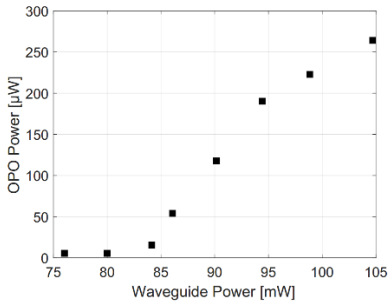

Figure 70- Plot of short-wavelength OPO power with input power in the bus waveguide

5.6. High-order harmonic generation in silicon nitride microrings

Third harmonic generation is a third-order nonlinear phenomenon and second harmonic generation is a second order nonlinear phenomenon. Since the silicon nitride is an amorphous material, the second order nonlinearity is normally forbidden, but second-harmonic generation can still occur at the interface between the silicon nitride waveguide and the silica cladding. As mentioned before, efficient harmonic generation takes place when phase matching between the fundamental and the high-order harmonic wave is achieved. Moreover, a slight variation of the

waveguide dimension can shift the phase matching condition away from the pump wavelength. In our experiments, we used optical amplifiers that operate in the C-band (1535 nm- 1565 nm) and the L-band (1565 nm-1625 nm) in order to find the phase-matched fundamental and harmonic wavelengths by spectrally tuning the pump within these bands.

The light associated with the generated high-order harmonics is collected by a multi-mode fiber from the top of the chip (Figure 71) because the coupling region of the resonator and the output reverse taper at the chip end-facet are optimized for the 1550 nm wavelength, leading to an insufficient coupling in the visible region (i.e. where the high-order harmonics lie). Consequently, the collected power shown in the spectra plotted in this section corresponds to the scattered light circulating in the ring. However, because it is hard to evaluate accurately the collection efficiency under these conditions, the conversion efficiency has not been quantified for the second- nor the third harmonic generation.

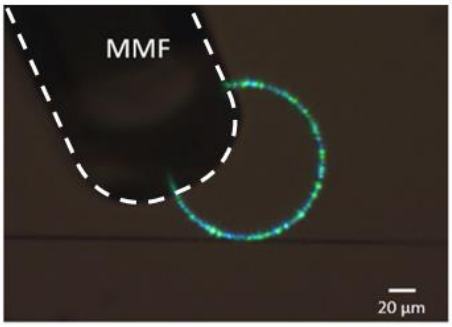

Figure 71- Top-view photograph image of the ring taken by a visible camera with a multimode fiber (MMF) collecting the light scattered from the top of the chip in the surrounding of the ring. Blue and green light is scattered around the ring while a near-IR continuous-wave signal (λ =1570 nm, P=850 mW) is injected into it.

The phase matching condition derived in chapter 3 for the second- and third-harmonic generation is strictly speaking adequate when a single pump is coupled to a waveguide. In the case of a resonator, when a frequency comb is generated, not only third or second harmonic generation but also other wave-mixing processes can take place such as:

$$\omega_{VG} = \omega_{IR1} + \omega_{IR2} + \omega_{IR3} \tag{5.6.1}$$

for the third-order processes where ω_{VG} is the green visible light frequency and $\omega_{IR1,2,3}$ is any of the frequency of the generated comb lines in the infrared range.

Many combinations of $\omega_{IR1,2,3}$ are possible and can lead to the creation of a resonant visible signal at ω_{VG}. This relaxes the constraint that is typically related to third-harmonic generation, where only a single monochromatic light can be generated, which frequency ω_{VG} must exactly match the triple of the pump frequency. Similarly, second-order processes can produce a visible signal at ω_{VR}, close to the second-harmonic frequency, but from the mixing of two different lines at slightly detuned frequencies (ω_{IR1} and ω_{IR2}) of the generated comb such as:

$$\omega_{VR} = \omega_{IR1} + \omega_{IR2} \tag{5.6.2}$$

Some signal close to third harmonic generation is observed in a Si_3N_4 ring resonator with a cross section of 1500 nm × 730 nm. The pump wavelength is scanned across several resonances and the light scattered from the ring is recorded using a visible charged coupled device (CCD) camera. The ring with a radius of 56 µm lights up in green when the pump is matched with a resonance at 1560 nm with 800 mW on chip coupled pump power (see figure 72). The associated spectrum measured with the multimode fiber shows a wavelength of 543nm, which likely corresponds to a third order sum frequency generation from three slightly different wavelengths of the generated comb.

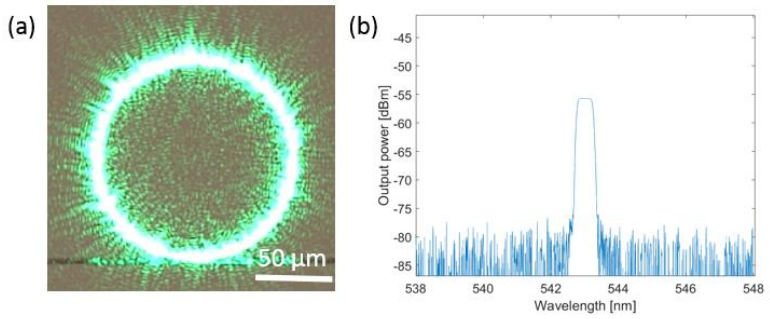

Figure 72- Green light generation (a) photograph of the ring exhibiting green scattered light as taken by a visible camera. (b) Corresponding output spectrum as recorded by a visible OSA from the multimode fiber placed on top of the ring. Here the 56 um radius Si_3N_4 ring is excited by 800 mW coupled pump power at 1560 nm.

Using another ring, when the pump is tuned to a resonance at smaller wavelength (1543 nm) with 900 mW coupled power, a blue light (495 nm) is generated by a third-order nonlinear interaction between different comb lines (Figure 73). The ring radius in this case is 200 µm and the waveguide cross sectional dimensions are 1550 nm ×760 nm. Note that different peaks appear in the spectrum (figure 73-b) because

there is different third order sum frequency events between the generated frequencies in the infrared (figure 73-c).

Note that the pump source is not spectrally pure because the amplified spontaneous emission.

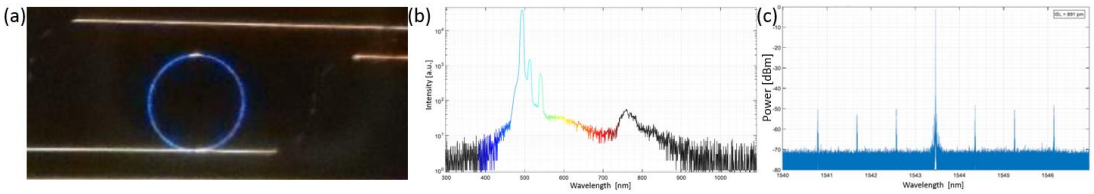

Figure 73- Blue light generation (a) photograph of the ring with 200 µm radius exhibiting blue scattered light taken by a visible camera. (b) Corresponding output spectrum as recorded by a visible OSA from a multimode fiber placed on top of the ring.(c) spectrum of the infra-red frequency comb generated simultaneously with the visible light. The Pump power is 900 mW and the wavelength of the pump is 1543.5 nm.

When the pump matches with a resonance at longer wavelengths (1568 nm) with 800 mW of on-chip coupled pump power, the ring shows red scattered light. However, from the spectrum recorded close to the second harmonic wavelength (Figure 74), assuming that the collection efficiency and the scattering efficiency are the same as for the third-order processes (on Fig. 72 and 73), we can infer that the conversion efficiency of the red light generated is smaller than that of the green light generated. This is rather expected for a centro-symmetric material. The ring radius is 56 µm and the cross section of the waveguide forming the resonator is 1450 nm × 730 nm.

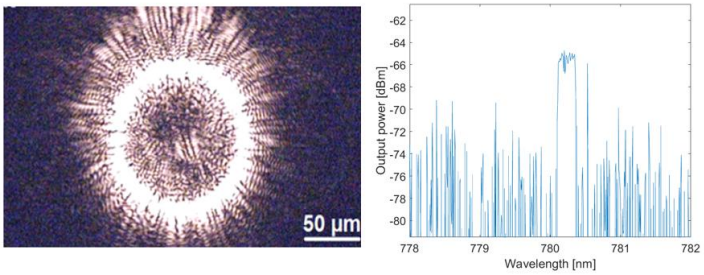

Figure 74- photograph of the ring with 56 µm radius exhibiting red scattered light taken by a visible camera. (b) Corresponding output spectrum as recorded by a visible OSA from a multimode fiber placed on top of the ring. The input power is 1 W and the wavelength of the pump is 1560 nm

Since the tensile strain of our silicon nitride is the highest tensile strain reported with respect to all silicon nitride platforms published in prior works [24], it likely presents the widest bandgap, offering the possibility to effectively guide shorter wavelengths than green visible light (532 nm). In fact, the generation of ultraviolet light (at 392

nm) was also observed during our measurements (Figure 75) when the ring was pumped at 1565 nm wavelength and a dense frequency comb is generated. Note that the ultra violet light wavelength is four times the pump wavelength.

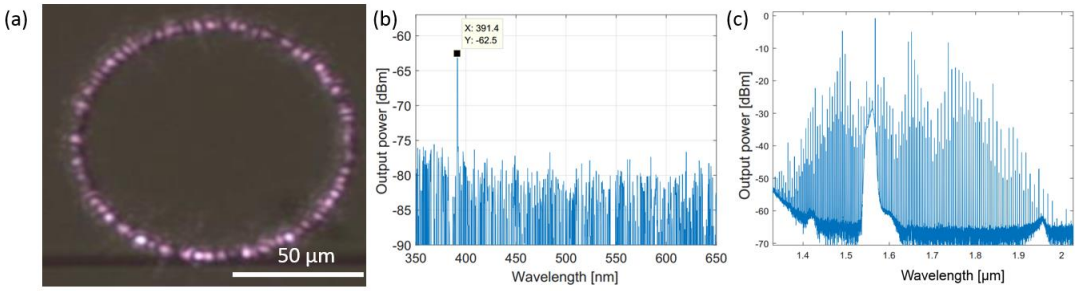

Figure 75- photograph of the ring with 56 µm radius exhibiting UV scattered light taken by a visible camera. (b) Corresponding output spectrum as recorded by a visible OSA from a multimode fiber placed on top of the ring. The input power is 1 W and the wavelength of the pump is 1565 nm. (c) Spectrum of the infra-red frequency comb generated simultaneously with the UV light.

The ultraviolet light signal can be, in principle, generated by a cascaded third-order nonlinear process between the pump at telecom wavelength and its second-order harmonic light (see Figure 76). In all prior works, to the best of our knowledge, the generation of short wavelength signals using silicon nitride or any other integrated material pumped at telecom wavelengths has been limited to third harmonic generation, mostly due to the transparence of the related material [100].

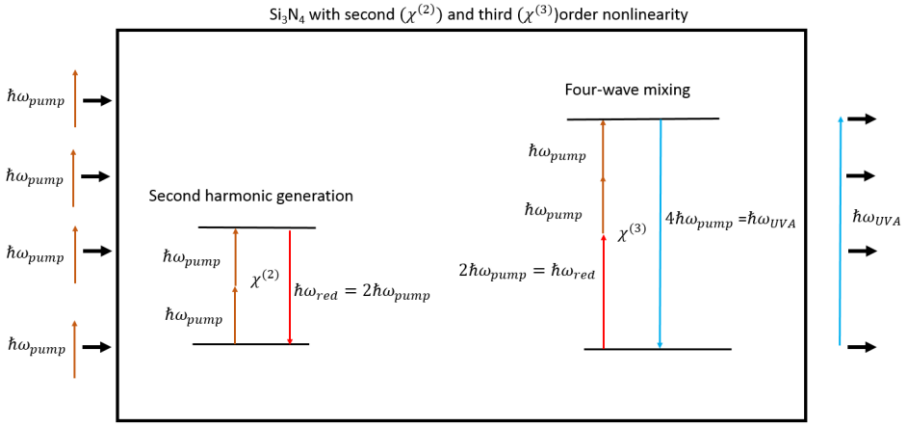

Figure 76- Energy level diagram of the cascaded phenomena (second-harmonic generation and four-wave mixing) for the emission of ultraviolet light by pumping the microring at telecom wavelengths.

The conversion efficiency of the ultraviolet light generation can be increased by reducing the propagation losses and increasing the intrinsic quality factor of our

resonator (Q_i=600,000) by applying high-temperature annealing steps (1200 °C) or by reducing the roughness of the waveguide via a tailored subtractive patterning process. These future process developments will be the subject of the next chapter.

5.7. Conclusion

In this chapter, we presented the linear properties of crack-free and annealing-free silicon nitride circuits, i.e. the waveguide propagation losses and dispersion, as well as the quality factor measurements of micro-ring resonators. More precisely, the propagation losses of our crack-free and annealing-free silicon nitride waveguides with a cross-sectional dimension of 1500 nm x 730 nm are 0.5 dB/cm (Q_i=6x10^5). Thanks to our deposition method we were able to deposit thick silicon nitride films so as to achieve anomalous dispersion (29 ps/nm/km) and generate an octave spanning frequency comb with a measured threshold of 83 mW. We measured the gamma parameter of our silicon nitride waveguides via two methods, i.e. self-phase modulation and four mixing, which provided a value of 2.8 $W^{-1}.m^{-1}$ for 750 nm × 720 nm cross-section dimensions. The associated nonlinear index of our Si_3N_4 material (n_2=3.6 × 10^{-19} $m^2.W^{-1}$ at 1550 nm) seems to be slightly higher than the nonlinear index of other LPCVD silicon nitrides in the literature. Finally, we have also shown that these devices could provide high-order harmonic (second and third) generation along with the generation of ultraviolet light that most likely results from the interplay between the second and the third order processes.

In order to fully unleash the potential of this material platform for nonlinear integrated optics by drastically reducing the propagation losses through eliminating the residual hydrogen and the related absorption in the C-band, high temperature annealing is applied. This will be studied in the next chapter. Even though this annealing detriment the CMOS compatibility, since the hydrogen content in our silicon nitride as deposited is low, after the annealing we achieve a record low losses for the waveguide with the same dimension.

CHAPTER 6
RECORD-LOW LOSS SILICON NITRIDE DEVICES AND FULLY INTEGRADTED FREQUENCY COMB SOURCES

We reported in the previous chapter how our Si_3N_4 chip-based platform could result in the demonstration of various nonlinear phenomena, including the generation of frequency combs. However, the propagation loss associated with these devices was not as low as the record values published in the literature by the EPFL group, for instance (5 dB/m in [107]). Consequently, we had to use relatively high pump powers to observe these nonlinear processes. By carefully optimizing the device fabrication process, we subsequently managed to achieve record-low loss Si_3N_4 integrated waveguides and micro-ring resonators, as presented in this chapter.

The propagation losses in a waveguide depend on the sidewalls roughness and the absorption of the material. The sidewall roughness itself depends on the lithography and the etching process, while the absorption of the material depends on the material composition, bulk absorption, surface-state passivation, mid-gap states, and the presence of contaminants. In this chapter, we present our achievements on record-low loss high confinement silicon nitride waveguides that are fabricated via a tailored patterning etching process, using a combined hydrogen/nitrogen annealing. By using this ultra-low loss technology, we demonstrate a fully integrated Kerr frequency comb source. The latter is achieved by butt-coupling a III-V DFB pump laser into a very high-Q silicon nitride microresonator.

6.1. Fabrication of record-low loss silicon nitride devices

Low propagation losses are crucial for power-efficient high-performance on-chip optical waveguides in several applications such as quantum photonics [101], integrated gyroscopes [102], and narrow linewidth lasers [103].

Recent studies published in 2018 based on large highly-multimode waveguides (2.5 µm -10 µm in waveguide widths) have shown ultra-high quality factors (37×10^6 and 67×10^6) [104]–[106]. However, such large waveguides limit the ability to engineer accurately the dispersion, which is a condition for broadband frequency comb generation. In particular, tightly confining waveguides with widths ranging from 1.5µm to 2 µm and heights between 0.75-0.85 µm are necessary for broadband Kerr frequency combs at telecom wavelengths [107]. Another advantage of using high-confinement waveguides is that the nonlinear parameter ($\gamma[W^{-1}m^{-1}]$), which is

inversely proportional to the optical mode dimension, is higher in smaller cross-section waveguides. Finally, the mode crossing in large waveguides is more important, which is problematic for the generation of low-noise dissipative Kerr soliton-based (DKS) frequency combs.

For tightly confining (1.6-μm-wide) waveguides, high quality factors in the order of 8.2×10^6 at 1560 nm have been achieved by using the proprietary Damascene reflow process [31]. However, the cross-wafer film thickness uniformity that can be achieved for a typical Damascene process is intrinsically limited by the chemical mechanical polishing (CMP) used for removing the silicon nitride layer using the etched silica trenches as a CMP self-stopper. Such cross-wafer film thickness variation (±20 nm) [108] is much higher than the non-uniformity induced by the low-pressure chemical vaporization deposition (±12 nm). Adding to that, typical waveguides fabricated following the Damascene process suffer from a high sidewall slope angle well above 8°, which can affect both the waveguide dispersion and, most importantly, the design reliability of the ring/ bus waveguide coupling section.

In this chapter, we show that by using a tailored process combined a new etching recipe and a refined hydrogen/nitrogen high-temperature annealing, we achieved quality factors well exceeding 8.5×10^6 for a ring resonator formed by a highly confined waveguide with a width of 1.7 μm and a height of 820 nm following a fully subtractive process. Moreover, as we can see in figure 77, the silicon nitride waveguide cross-sectional profile obtained in our process is strongly anisotropic is 88.2° (less than 2° of sidewalls slope angle).

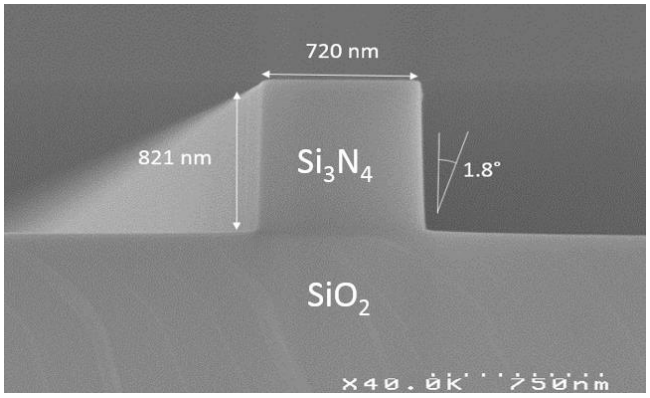

Figure 77- Scanning electron microscope image of a single-mode silicon nitride waveguide fabricated under the optimized process. (before the annealing and before encapsulation)

As compared with the process described in Chapter 4, the main changes lie in (1) the etching recipe of the Si_3N_4 devices; which has been improved dramatically towards the very end of this PhD and (2) the use of an additional multi-step annealing treatment performed after the etching process. More precisely, the Si_3N_4 film is etched with a CF_4-CHF_3-Ar plasma instead of CF_4-CH_2F_2-O_2, while a pure hydrogen annealing (900 °C for 5 min) followed by a pure oxygen (1200 °C for 20 minutes) and a pure nitrogen annealing (1200 °C for 3 hours) are applied on the wafer before the silica layer PECVD encapsulation. The line edge roughness (LER) of our waveguides at different stages of the process is measured by atomic force microscopy (Figure 78). The as-etched Si_3N_4 waveguides present a mean square left/right sidewall roughness in the range of 1.2-1.3 nm, confirmed by AFM and CD-SEM morphological observations. The waveguide sidewall roughness and the morphology are only slightly impacted by the annealing (1 nm after the annealing instead of 1.2 nm before). Instead, the beneficial impact of the annealing resides in an almost complete elimination of the few remained N-H bonds, responsible for the residual absorption losses. Eventually, our deposited silicon nitride exhibits a low hydrogen content so as to enable frequency comb generation without a post-annealing step (see chapter 5), but this additional nitrogen annealing allows us to achieve very low propagation losses, which translates into a decrease of the pump power needed to observe the frequency comb, as will be presented in section 6.3.

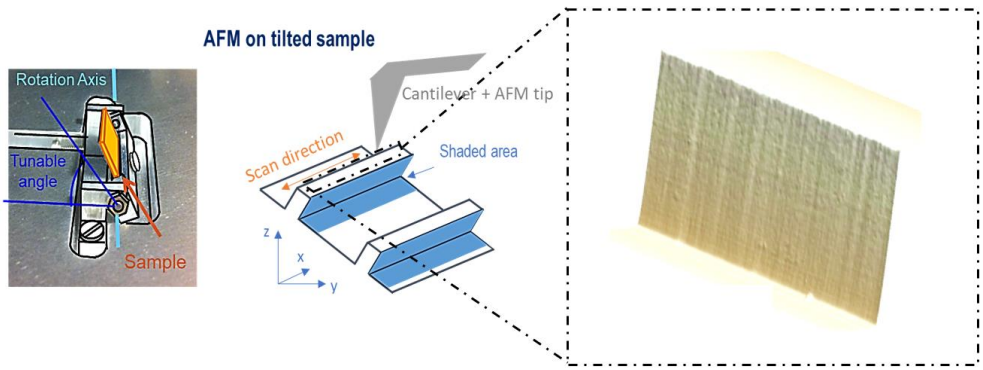

Figure 78- Line edge roughness measurement by atomic force microscopy (after the etching And before the encapsulation).

Regarding the etching recipe, in our previous process, the $CF_4/CH_2F_2/O_2$ plasma used to pattern the Si_3N_4 waveguides systematically resulted in the presence of polymer residues on the silicon nitride sidewalls and at the bottom of critical high-aspect ratio regions, such as the coupling gap between the bus waveguide and the microresonator. Polymer residues then inevitably bring in an increase in the line edge roughness and organic contamination in critical regions of such architectures. A proposed solution has been to increase the flow of oxygen to reduce the polymer thickness [22]. However, in this case, the oxygen would thin down the photoresist, leading to a selectivity (photoresist versus Si_3N_4) decrease, resulting in a larger sidewall roughness. This would also impose limited sub-micrometric waveguide thickness, trapezoidal waveguide profiles, thus causing the unpredictability of the extrinsic loss rate (i.e., the power loss from the resonator to the bus waveguide). To overcome these limitations associated with the $CF_4/CH_2F_2/O_2$ plasma etching, we advantageously moved towards the use of a less polymerizing plasma chemistry based on CHF_3 instead of CH_2F_2.

Concerning the annealing, in order to reduce the attenuation coefficient to the lowest possible value, we developed a multiple-step chemical physical in-situ high-temperature annealing sequence using H_2, O_2, and N_2 following the waveguide patterning (Figure 79). We detail the different steps of this optimized annealing sequence in the three paragraphs below.

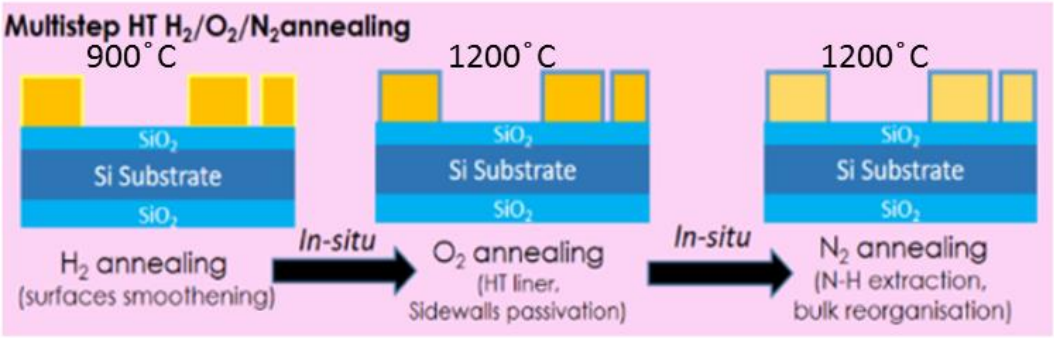

Figure 79-Multistep $H_2/O_2/N_2$ in-situ annealing of patterned core Si_3N_4 waveguides

Recent studies have shown the pure hydrogen streams capability to smoothen out the sidewall roughness of single-mode silicon waveguides for TE-operation to record-low values, when operating such H_2 annealing at particular pressure,

temperature, and time exposure conditions [46]. By following the same rationale, we first applied a flash (i.e. a few minutes long) 1100 °C hydrogen based annealing in order to induce morphological modification of the waveguide.

As a second operation, the waveguides are exposed to a full O_2-based 1200 °C annealing for a few minutes. This step is aimed at reducing surface states through the effective passivation and mechanically-robust encapsulation of the waveguide core via a dense, high-temperature, native oxidation of the silicon nitride surface, precluding the formation of intra-gap scattering absorption centers.

Finally, the silicon nitride film should be densified through driving out the hydrogen excess and breaking N-H bonds in order to get closer to a stoichiometric Si_3N_4 film, reducing, in turn, the material absorption loss in the C-band. A pure nitrogen annealing is applied on the un-cladded waveguides (1200 °C for 3 hours) in order to drive out the residual hydrogen and break the residual N-H. This provides sufficient activation energy to reorganize the bulk structure of the waveguide in order to minimize the presence of bulk defect states, otherwise causing detrimental bulk absorption. We note that although this annealing treatment is done to the detriment of the CMOS compatibility that was maintained with the process flow of chapter 4, it allows us to push the loss down to very low values and study the full potential of our material platform for linear and nonlinear optics, as described in the next two sections.

6.2.Linear characterization of low loss Si_3N_4 devices

The optical characterization of the ring resonators fabricated following our optimized etching/ annealing process is performed via grating couplers on a 300 mm prober station using a tunable laser source for direct resonance scanning. The wavelength tuning range is 1560-1562 nm at a 0.1 pm resolution step, which is the minimum wavelength-sampling step of our Agilent 8640 source. A statistical analysis on the probed resonances was also conducted on the wafer in order to estimate the reproducibility of the optical losses and the quality factor of the micro-ring resonators with a cross-section of 1650 nm x 800 nm. In this study, the ring resonator radius is 112 μm and the critical coupling condition is achieved for a ring/

bus waveguide gap of 550 nm. Without annealing, the quality factor of our resonators is $Q_i = 6 \times 10^5$ which is comparable to the value obtained with the process described in chapter 4. Note that after the roughness reduction the propagation losses don't decrease drastically because the absorption.

In order to evaluate the attenuation coefficient of the resonator via the intrinsic quality factors, we measured resonators operating in the under-coupled regime, so as to minimize the contribution from the excess losses caused by coupling non-ideality, and thus have the internal (intrinsic) loss rate $\kappa_0/2\pi$ dominating the total loss rate. In detail, the analysis is performed by measuring the resonance linewidths from the transmission spectrum. This provides the resonator total loss rate $\kappa/2\pi = (\kappa_0 + \kappa_{ex})/2\pi$ (or equivalently the loaded Q-factor Q_L), which is the sum of the coupling loss rate $\kappa_{ex}/2\pi$ from the bus to the microring (Q_c) and the intrinsic microresonator loss rate $\kappa_0/2\pi$ (Q_i). Under-coupled resonators were found only for the maximum available ring-waveguide gap on the maskset (i.e., a gap width of 600 nm). As shown in Figure 80, resonance doublets could be easily observed all across the wafer for such coupling rate. This mode splitting is typical of highly confined resonators with high quality factor [108]. Any small fabrication imperfections can easily induce coherent backscattering in the micro-resonator, leading to a splitting of the resonance as shown in figure 80 [114]. By using a resonant doublet line shape fitting model, an intrinsic loss rate $\kappa_0/2\pi$ of 24 MHz could be extracted from the measurements, corresponding to an intrinsic quality factor $Q_i \sim 8.4 \times 10^6$ at 1560 nm wavelength (C-band), and a fitted splitting rate $\Omega/2\pi = 56$ MHz.

The intrinsic quality factors are extracted by fitting the measured resonance transmission with the following doublet model:

$$T = \left[1 - \frac{\kappa_{ex}/2\pi}{2\left(i(f-f_1) + \kappa_{01}/2\pi + \kappa_{ex}/2\pi\right)} - \frac{\kappa_{ex}/2\pi}{2\left(i(f-f_2) + \kappa_{02}/2\pi + \kappa_{ex}/2\pi\right)}\right]^2 \quad (6.2.1)$$

where $\kappa_{01}/2\pi$ and $\kappa_{02}/2\pi$ are the intrinsic linewidths of the clockwise (CW) and counter-clockwise (CCW) modes in the resonator, while f_1 and f_2 are the resonant frequencies of the two modes in the resonator.

The statistical study performed on 22 nominally identical microrings that belong to 22 different dies on the 200 mm wafer shows a cross-wafer variability of the Q_i values of 0.8% only, which proves the high reproducibility of the fabrication process.

Using the relation $Q_i = \frac{k_0 n_{eff}}{\alpha}$ this high Q_i quality factor is equivalent to propagation losses of just 3.8 dB/m against 4 dB/m for the state-of-the-art damascene process [109] and 0.5 dB/cm for the devices of chapter 4. Note that the theoretical optical parametric oscillation power threshold for such high quality factor Si_3N_4 ring resonator is sub-milliwatt, which is easily achievable with the existing III-V on Si laser technology [4].

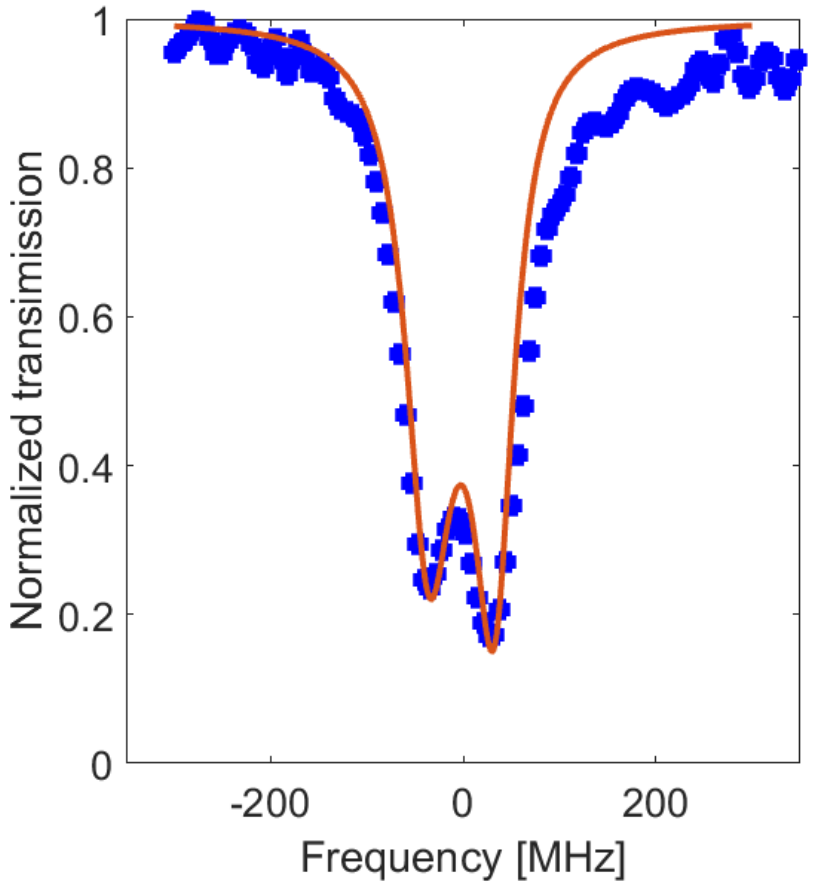

Figure 80- Resonance doublet at λ =1560 nm with an extracted fitted intrinsic linewidth $\kappa_0/2\pi$ of 24 MHz corresponding to an intrinsic $Q_i \sim 8.4 \times 10^6$, and fitted splitting rate $\Omega/2\pi = 56$ MHz

In order to highlight the potential of the ultra-high quality factor and the tight-high confinement waveguide, we demonstrate a full comb with the native line spacing (2 nm) with 4.3 mW of on-chip optical power at 1560 nm wavelength (pumped by an

Agilent 8614B). The microring radius is 112 µm radius (gap= 550 nm) and the output optical spectrum is shown in Figure 81 (a).

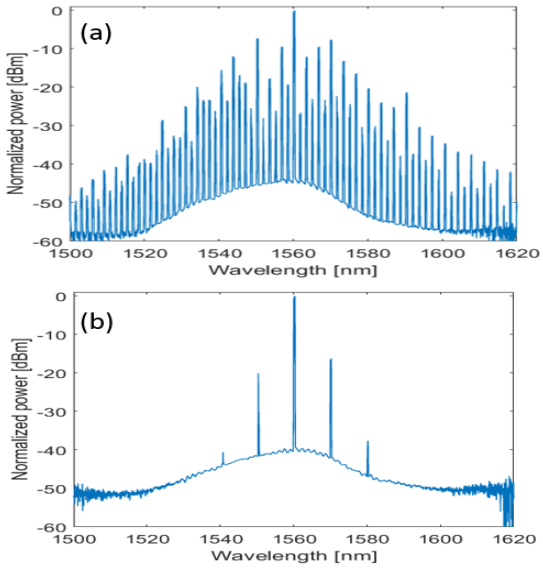

Figure 81- Frequency comb generation. (a) A comb generation with the native spacing using a 112-µm-radius microring (gap= 550nm) for coupled power of 4.3 mW (b) Comb spectrum for coupled Pin ~ 1.8 mW. The laser used is an Agilent 8614 B.

For an on-chip optical power of 1.8 mW, which is above the optical parametric oscillation threshold, the associated spectrum is shown in figure 81 (b). Note that the light is coupled and collected via a 1-D grating coupler with 10 dB of coupling losses. In fact the frequency comb generated might be larger but we are limited by the 40 nm at 3 dB bandwidth of the grating coupler.

The table 5 summarizes the performance associated with the relevant studies on Si_3N_4 micro-ring resonators using highly multi-mode waveguides and tightly confined waveguides. Our results thus appear well within the state-of-the-art in terms of the low loss reported on this material platform for highly nonlinear waveguides, making it well-suited for the realization of fully integrated frequency comb sources.

	Tightly confined waveguide		Highly multi-mode waveguides
	Our work	[107]	[104]
$\gamma[{}^{W^{-1}}/_{m^{-1}}]$	0.64	0.64	0.14
Q_i	$8.4x10^6$	$8.2x10^6$	$67x10^6$
α [dB/m]	3.8	4	0.4
#TE mode	4	4	>20
Ring radius [µm]	112	230	369
A_{eff} [µm^2]	1.2	1.2	0.55

Table-5: Comparison between tightly confined and highly multimode silicon nitride waveguides performance obtained in this work and the state-of-the-art.

6.3. Compact frequency comb sources with a DFB butt-coupled to a Si_3N_4 microresonator

The early demonstrations of soliton based frequency combs started by using bulky and complicated setups where an external laser had to be accurately tuned into the resonance to achieve the soliton states [110]. Subsequently, soliton based frequency comb generation has been demonstrated by butt-coupling a reflective semiconductor optical amplifier (RSOA) to a silicon nitride resonator [111]. This solution requires on chip filtering as well as integrated heaters for thermal stability management, which add some complexity in both the fabrication process and the achievement of soliton generation. Recently, soliton based frequency comb generation has been demonstrated by the self-injection locking of a multi-frequency Fabry-Perot on-chip laser with MgF_2 bulk crystalline resonators [105], [112]. Such demonstration facilitates the otherwise complicated soliton generation method. The same demonstration has been also made by butt coupling a multi-frequency Fabry-Perot on-chip laser (100 mw output power) with a silicon nitride resonator [108] but the silicon nitride circuit is air-cladded due to dispersion constraints limited by the available Si_3N_4 thickness, which makes it hard to fully package the system (pump and silicon nitride chip), increasing the device failure probability.

In this section, we will present one the most topical results of this PhD work, notably the prototype demonstration of an integrated Kerr frequency comb source based on the butt coupling between a III-V DFB laser and a silicon nitride (Si_3N_4) microresonator (Figure 82). This measurements are performed in III-V Lab at Palaiseau.

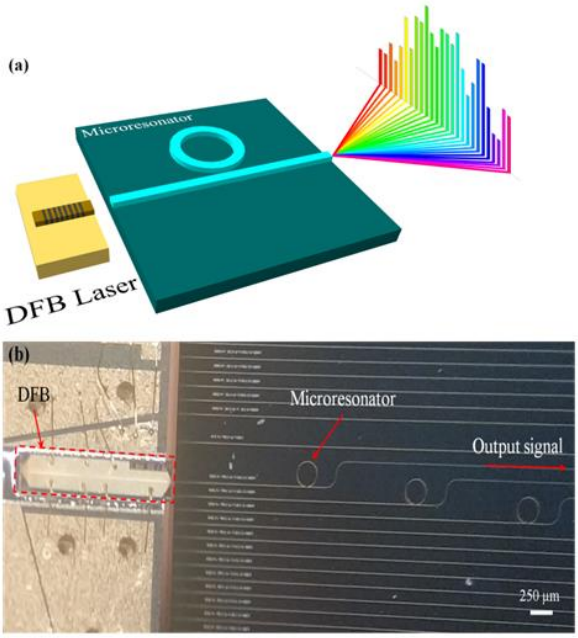

Figure 82-a) Schematic of optical frequency comb generation by pumping the nonlinear Si_3N_4 microresonator with the DFB laser. b) Top view microscope image of the butt-coupling between the two chips. The output signal is extracted with a lens fiber at the right of the passive waveguide (not visible on the picture). The two chips are moved independently, and by the translation of the passive Si_3N_4 chip, various ring microresonators can be easily tested.

The InP/InGaAsP DFB laser is designed to guarantee a single-mode laser emission able to provide a sufficient pomp power (above 100mW, see Fig. 83) for the generation of an optical comb in the ring resonator. The DFB laser is fabricated using a dual channel shallow ridge structure as described in [113] by III-V lab/Thales. The laser cavity length is 1.75 mm. To ensure maximum output power and an optimal coupling with the Si_3N_4 passive chip, the back facet of the laser is coated to be highly reflective and the output facet anti-reflective. The DFB laser threshold is 81 mA and the output power reaches up to more than 200 mW, as shown in Figure 83. An advantage of this laser is that its wavelength can be precisely tuned by changing the bias current (1.5 pm/mA for a temperature set around 25°C), which allows for an easy scan across the microring resonance spectrum.

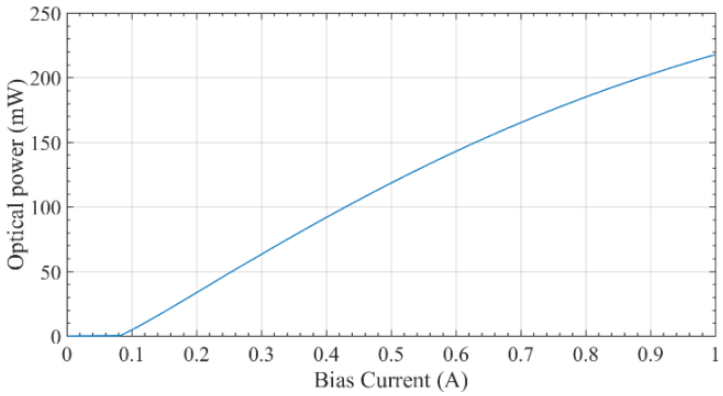

Figure 83- Optical power measurement at 25°C from the DFB laser at 1576 nm.

The DFB laser output mode has an elliptic shape: we measured a total angle at $1/e^2$ of 20° × 60° (horizontal × vertical). This non-circular beam is due to the specific design of the laser [113]. We point out that the laser divergence should be as close as possible to the divergence of the passive chip spot size adapter (3.5 µm) to maximize the coupling efficiency.

As shown in Figure 84, the measured spectrum laser exhibits a good side-mode suppression ratio (SMSR) of 57 dB, which circumvents the possible perturbations of the frequency comb generation during the pumping of the microresonator.

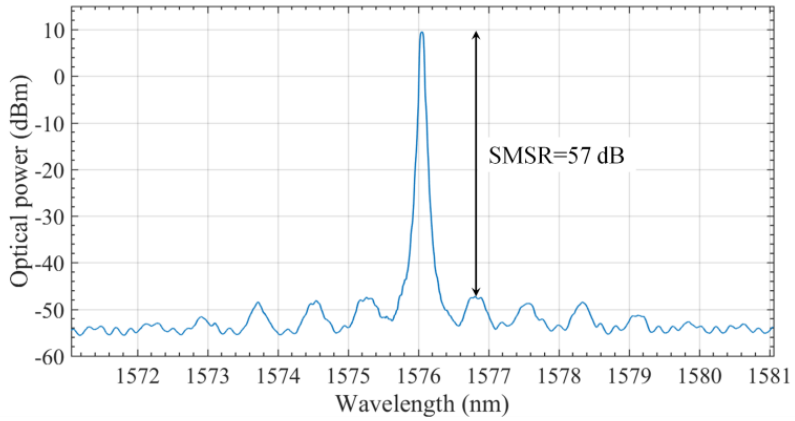

Figure 84- Optical spectrum from the DFB laser chip recorded for a 823 mA bias current and a 25.6°C temperature.

The microresonator used for the first demonstration of the compact DFB/Si_3N_4 butt-coupled frequency comb source was a 56-µm radius Si_3N_4 ring fabricated using an intermediate process (i.e. an intermediate quality factor) between that described in chapter 4 and the latest optimized one as described at the beginning of this chapter. In particular, it included just one annealing step for 3 hours under nitrogen

atmosphere performed after the silica layer encapsulation of the devices. Some tests are ongoing for butt-coupled prototypes using new samples realized according to the latest optimized process that exhibit waveguide propagation losses down to 4 dB per meter and ring resonator quality factors up to ten millions (>6 *x* 10^6).

The cross-sectional dimensions of the present ring waveguide (1.5 µm-wide × 800 nm-thick) ensure that the dispersion is anomalous at the pump wavelength across the C band, which greatly eases the frequency comb generation. Moreover the gap between the ring and the bus is 500 nm that corresponds to an under-coupled regime. We measured the reflectivity and the transmission spectrum of the ring by using a high-resolution optical spectrum analyzer (OSA) from APEX Technologies (AP2043B model) with an integrated tunable laser source. We only probed transverse electric (TE) resonances since the DFB laser used as a pump is TE polarized.

The measured resonance close to 1576nm (Figure 85) shows a mode splitting as in Figure 80. Both resonances have a 1.56 pm (188 MHz) linewidth, meaning, according to equation 6.1.1, an intrinsic quality factor Q_i of ~1×10^6. Considering this value, the theoretical threshold to generate a frequency comb using such a ring resonator pumped by a butt-coupled DFB laser should be 12 mW. The 33 pm periodic oscillation superimposed on the reflectivity spectrum is due to the waveguide back-end facet reflection that forms a parasite and longer cavity.

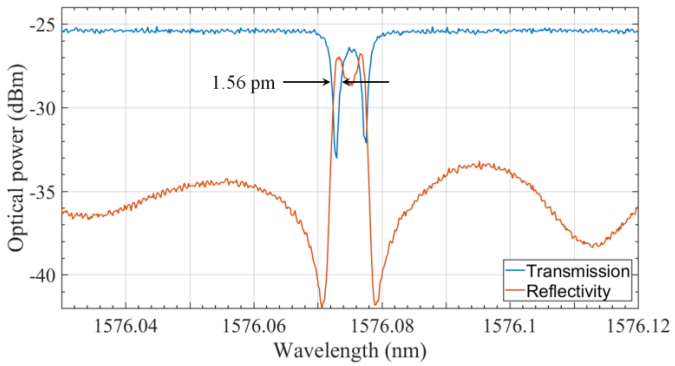

Figure 85- Spectral response (TE polarized) of the 56 µm radius Si_3N_4 microring, measured by a 1.12 pm resolution OSA (including a tunable cw laser source). The gap between the ring and the resonator is 500 nm.

To perform the butt-coupling test between the DFB laser and the passive chip (as shown on Fig. 82), we used a dynamical alignment system with micrometric

translation stages. Consequently, mechanical vibrations slightly affect the performance of our device. By first injecting a test signal in the bus waveguide, we measure the far-field at the output of the edge coupler, where light will be injected from the DFB. The related full angle divergence at $1/e^2$ is 22° × 34° (horizontal × vertical).By computing the overlap of the measured far-field from the DFB laser and the edge coupler, we estimate a 0.6 dB coupling loss at best.

The operating output power of the DFB laser was set at 187 mW. If we subtract the coupling loss due to the mode mismatch and the propagation losses in the bus Si_3N_4 waveguide before the ring, we estimate a maximum coupled power of 150 mW to the Si_3N_4 chip where the ring lies, with an OPO threshold of 12 mW on-chip estimated power. The power actually injected is lower though due to the misalignment between the two chips. By tuning the DFB current, the wavelength of the pump is scanned across a resonance. When the pump wavelength matches with the resonance of the ring, a frequency comb is generated through cascaded parametric degenerated Four Wave Mixing (FWM) [115], as shown in Figure 86.

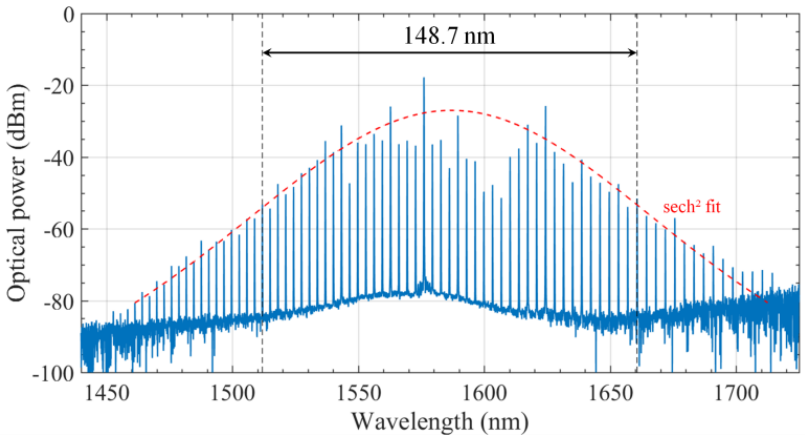

Figure 86-Spectral measurement of an optical frequency comb generated by the pumped microresonator. The bias current of the DFB laser was 813 mA, meaning a 187-mW laser power at the 1576.08 nm DFB wavelength.

Here the wavelength pump laser was set at 1576.08 nm to match a particular resonance of the microresonator. The microresonator design provides anomalous group velocity dispersion [6], which greatly facilitates Kerr comb generation. As shown on Figure 86, the 30-dB bandwidth of the Kerr comb with a native line spacing is measured to be 148.7 nm (18 THz), which is the largest value for a fully compact system to the best of our knowledge. The spectrum is collected via edge

coupler at the output .This comb spectrum has a spectral shape characteristic of the single dissipative Kerr soliton (DKS) state. Other measurements are yet necessary to prove the existence of the DKS state: autocorrelation amplitude noise measurements should be used to confirm the soliton regime.

The butt coupling experiences show the full potential of the silicon nitride technology to obtain a fully packaged comb source that can be used for several applications such as telecommunication, spectroscopy, atomic clock, etc…

If we compare this result with the literature, the only fully packaged demonstration [111] where a RSOA was butt coupled to a silicon nitride chip demanded spectral filtering which hinders the prospects for integration . The demonstration using a Fabry Pérot laser butt coupled to an air cladded silicon nitride chip suffers from a big failure probability since the silicon nitride is exposed to air. Moreover, the bandwidth of the frequency comb in the last demonstrations was limited to 100 nm. In contrast, in our demonstration, the silicon nitride chip and the DFB pump laser could be easily packaged. This is made possible thanks to the deposition of a thick silicon nitride film (>800 nm) achieving high anomalous dispersion regime (a condition to obtain soliton-based frequency comb at low pump power) while the silicon nitride waveguides are fully embedded in silica. Finally, we note that frequency combs generated with a further reduced pump power could be achieved by leveraging the latest technological developments presented at the beginning of this chapter (the best intrinsic Q-factors being 8 times larger than that of the devices used in the above demonstration).

6.4. Conclusion

We have developed a Si_3N_4 on silicon fabrication platform that allows for the fabrication of tightly confining microresonators featuring highly competitive quality factors (Q_i~$10x10^6$) for 1.7 um×800 nm cross-sectional dimensions. In addition, we have demonstrated a compact optical frequency comb source formed by butt-coupling an InP DFB laser that delivers ~200 mW, and a Si_3N_4 microresonator with an intrinsic Q of ~10^6. We succeeded to measure a 148.7 nm (18 THz) broadband

frequency comb with a native line spacing, which is so far, the largest span ever measured on an ultra-compact source. Such compact power-efficient prototype offers a short-time perspective for a wide variety of applications relying on precise frequency comb based metrology, non-classical states of light and quantum emitters, photonic communications.

CHAPTER 7
OVERVIEW AND PERSPECTIVES

Continuous and rapid growth of the internet data traffic in the telecommunication infrastructures imposes higher transmission rates as well as bigger data centers. In fact, the development of new technologies is necessary to meet these needs as the integration of more and more lasers on the same chip along with a more-Moore path would be at stake in the very end. In this context, nonlinear frequency combs, providing a dense array of optical lines emitted by a single device, is a potential game changer to overcome the bottleneck of today's transceivers.

Resonators with high quality factors are crucial for on-chip efficient frequency comb generation. Today, the highest quality factors are achieved in whispering gallery modes resonators in silica wedges. However, the low refractive index of the silica requires an air cladding, making integration elusive. At telecom wavelengths, silicon nitride (Si_3N_4) is a trade-off material that provides, at the same time, relatively high nonlinearity, low propagation losses, no two-photon absorption as well as the ability to obtain high confinement waveguides.

Silicon nitride is a standard low-cost CMOS material that benefits from the mature electronic manufacturing. However, the LPCVD silicon nitride that is traditionally grown is not free of hydrogen, which causes high losses in the C-band because of the N-H bond overtone absorption. Consequently, other groups have not been able to generate frequency combs without applying a long time high temperature annealing step to extract the residual hydrogen content in the Si_3N_4 film.

From this starting point, we aimed, during this PhD, to develop as-deposited silicon nitride thin films with sufficiently low hydrogen content to reduce the material bulk absorption in the C-Band. Nevertheless, silicon nitride is a highly tensile strain material, making it challenging to grow relatively thick (typically > 700 nm) silicon nitride films, as required to obtain anomalous dispersion, a condition to generate broadband frequency combs.

During this PhD work, we fabricated annealing-free and crack-free silicon nitride micro-resonators with a sufficiently low hydrogen content, sufficiently thick films and high quality factor resonator (6×10^5) so as to allow for the generation of a frequency comb at reasonably low threshold pump power (83 mW). This demonstration opens the way towards monolithically integrated frequency comb

sources with silicon photonics components for different applications, such as optical telecommunications, absorption spectroscopy, and integrated quantum optics.

By taking advantage of the high quality and low hydrogen content of our as-deposited silicon nitride films, we further developed and optimized the Si3N4 device fabrication process, in particular the etching step. In addition, to study the full potential of our Si_3N_4 material platform for nonlinear optics, we developed a carefully tailored multistep chemical-physical annealing which resulted in devices with record-low loss (of 3 dB/m, and equivalently intrinsic Q of 10^7) in the C band. These were achieved in tightly confining waveguide geometries (1.7 μm*800 nm cross-section dimensions), thus associated with relatively high nonlinear gamma parameters (γ~0.64 $W^{-1}m^{-1}$).

Using such high quality technology, a frequency comb could be generated by butt-coupling a DFB laser with a silica cladded high-*Q* silicon nitride micro-resonator constituting an electrically driven and compact fully integrated comb sources ready to be packaged.

In summary, during this thesis we developed novel technological building blocks aiming at decisive key breakthrough in perspective applications notably as quantum optics and quantum photonics computing, energy-efficient nonlinear optics and frequency combs generation for telecommunications, optical metrology, on-chip spectroscopy, and biosensing. In addition, enhanced Kerr optical nonlinearity and an integrated passively mode-locked laser is considered using hybrid graphene/Si_3N_4 circuits [116]. Moreover, lidars for the autonomous cars require a high optical power levels which is problematic in the case of III-V/Si lasers because the two photons absorption of the silicon. Consequently, a III-V/Si_3N_4 or III-V/Si/Si_3N_4 can be a solution for such application.

Bibliography

[1] "Cisco Visual Networking Index: Global Mobile Data Traffic Forecast Update, 2017–2022 White Paper - Cisco." [Online]. Available: https://www.cisco.com/c/en/us/solutions/collateral/service-provider/visual-networking-index-vni/white-paper-c11-738429.html. [Accessed: 30-May-2019].

[2] C. Cole *et al.*, "Techno-Economic Comparison of Silicon Photonics and Multimode VCSELs," *J. Light. Technol. Vol. 34, Issue 2, pp. 233-242*, vol. 34, no. 2, pp. 233–242, Jan. 2016.

[3] C. Sun *et al.*, "Single-chip microprocessor that communicates directly using light," *Nature*, vol. 528, no. 7583, pp. 534–538, Dec. 2015.

[4] B. Ben Bakir *et al.*, "Electrically driven hybrid Si/III-V Fabry-Pérot lasers based on adiabatic mode transformers," *Opt. Express*, vol. 19, no. 11, p. 10317, 2011.

[5] T. Maiman, "Stimulated optical radiation in ruby," 1960.

[6] P. A. Franken, A. E. Hill, C. W. Peters, and G. Weinreich, "Generation of Optical Harmonics," *Phys. Rev. Lett.*, vol. 7, no. 4, pp. 118–119, Aug. 1961.

[7] Woodbury, E.J. and Ng, W.K., "Ruby laser operation in near IR.," *Proc. IRE*, vol. 50, no. 11, pp. 2365–2383, 1962.

[8] G. Eckhardt, R. W. Hellwarth, F. J. McClung, S. E. Schwarz, D. Weiner, and E. J. Woodbury, "Stimulated Raman Scattering From Organic Liquids," *Phys. Rev. Lett.*, vol. 9, no. 11, pp. 455–457, Dec. 1962.

[9] H. Kildal and J. C. Mikkelsen, "Efficient doubling and CW difference frequency mixing in the infrared using the chalcopyrite CdGeAs2," *Opt. Commun.*, vol. 10, no. 4, pp. 306–309, Apr. 1974.

[10] C. Monat *et al.*, "Green light emission in silicon through slow-light enhanced third-harmonic generation in photonic-crystal waveguides," *Nat. Photonics*, vol. 3, no. 4, pp. 206–210, 2009.

[11] A. A. Savchenkov, A. B. Matsko, V. S. Ilchenko, I. Solomatine, D. Seidel, and L. Maleki, "Tunable optical frequency comb with a crystalline whispering gallery mode resonator," *Phys. Rev. Lett.*, vol. 101, no. 9, 2008.

[12] I. S. Grudinin, N. Yu, and L. Maleki, "Generation of optical frequency combs with a CaF_2 resonator," *Opt. Lett.*, vol. 34, no. 7, p. 878, 2009.

[13] P. Del'Haye, "Optical Frequency Comb Generation in Monolithic Microresonators," Munchen University, 2011.

[14] N. Izhaky *et al.*, "Development of CMOS-compatible integrated silicon photonics devices," *IEEE J. Sel. Top. Quantum Electron.*, vol. 12, no. 6, pp. 1688–1697, 2006.

[15] A. Alduino and M. Paniccia, "Wiring electronics with light," *Nat. Photonics*, vol. 1, no. 3, pp. 153–155, 2007.

[16] D. J. Moss, R. Morandotti, A. L. Gaeta, and M. Lipson, "New CMOS-compatible platforms based on silicon nitride and Hydex for nonlinear optics," *Nat. Photonics*, vol. 7, no. 8, pp. 597–607, 2013.

[17] L. Liao *et al.*, "High speed silicon Mach-Zehnder modulator," *Opt. Express*,

vol. 13, no. 8, p. 3129, 2005.
[18] L. Vivien *et al.*, "High speed and high responsivity germanium photodetector integrated in a Silicon-On-Insulator microwaveguide," *Opt. Express*, vol. 15, no. 15, p. 9843, Jul. 2007.
[19] W. Bogaerts *et al.*, "Silicon-on-Insulator Spectral Filters Fabricated With CMOS Technology," *IEEE J. Sel. Top. Quantum Electron.*, vol. 16, no. 1, pp. 33–44, 2010.
[20] G. T. Reed, "The optical age of silicon," *Nature*, vol. 427, no. 6975, pp. 595–596, Feb. 2004.
[21] M. Asghari and A. V. Krishnamoorthy, "Energy-efficient communication," *Nat. Photonics*, vol. 5, no. 5, pp. 268–270, May 2011.
[22] J. S. Levy, A. Gondarenko, M. A. Foster, A. C. Turner-Foster, A. L. Gaeta, and M. Lipson, "CMOS-compatible multiple-wavelength oscillator for on-chip optical interconnects," *Nat. Photonics*, vol. 4, no. 1, pp. 37–40, 2010.
[23] K. Luke, A. Dutt, C. B. Poitras, and M. Lipson, "Overcoming Si3N4 film stress limitations for high quality factor ring resonators," *Opt Express*, vol. 21, no. 19, pp. 22829–22833, 2013.
[24] M. H. P. Pfeiffer *et al.*, "Photonic Damascene process for integrated high-Q microresonator based nonlinear photonics," *Optica*, vol. 3, no. 1, p. 20, Jan. 2016.
[25] S. Kim *et al.*, "Dispersion engineering and frequency comb generation in thin silicon nitride concentric microresonators," *Nat. Commun.*, vol. 8, no. 1, p. 372, Dec. 2017.
[26] J. Chiles *et al.*, "Deuterated silicon nitride photonic devices for broadband optical frequency comb generation," *Opt. Lett.*, vol. 43, no. 7, p. 1527, Apr. 2018.
[27] Y. Vlasov, "Silicon CMOS-integrated nano-photonics for computer and data communications beyond 100G," *IEEE Commun. Mag.*, vol. 50, no. 2, pp. s67–s72, Feb. 2012.
[28] R. W. Boyd, *Nonlinear optics*. Academic Press, 2008.
[29] J. Hansryd, P. A. Andrekson, M. Westlund, J. Li, and P. Hedekvist, "2002QE_Invited cited by 228 MINHA REF.pdf," *IEEE J. Sel. Top. Quantum Electron.*, vol. 8, no. 3, pp. 506–520, 2002.
[30] R. K. W. Lau *et al.*, "Continuous-wave mid-infrared frequency conversion in silicon nanowaveguides," *Opt. Lett.*, vol. 36, no. 7, p. 1263, 2011.
[31] M. Foster, A. Turner, J. Sharping, B. S.- Nature, and U. 2006, "Broad-band optical parametric gain on a silicon," *Nature*, vol. 441, pp. 960–963, 2006.
[32] R. H. Stolen and J. E. Bjorkholm, "Parametric Amplification and Frequency Conversion in Optical Fibers," *IEEE J. Quantum Electron.*, vol. 18, no. 7, pp. 1062–1072, 1982.
[33] A. B. Matsko, A. A. Savchenkov, D. Strekalov, V. S. Ilchenko, and L. Maleki, "Optical hyperparametric oscillations in a whispering-gallery-mode resonator: Threshold and phase diffusion," *Phys. Rev. A*, vol. 71, no. 3, p. 033804, Mar. 2005.
[34] Y. R. Chen, "Surface properties probed by second-harmonic and sum-frequency generation," *Nature*, vol. 337, no. 9, p. 519, 1989.

[35] J. Sipe, D. Moss, H. V. D.-P. R. B, and U. 1987, "Phenomenological theory of optical second- and third-harmonic generation from cubic centrosymmetric crystals," *Phys. Rev. B*, vol. 35, pp. 1129–1141, 1987.

[36] M. Yamada, N. Nada, M. Saitoh, and K. Watanabe, "First-order quasi-phase matched LiNbO 3 waveguide periodically poled by applying an external field for efficient blue second-harmonic generation," *Appl. Phys. Lett.*, vol. 62, no. 5, pp. 435–436, Feb. 1993.

[37] C. Lacava, V. Pusino, P. Minzioni, M. Sorel, and I. Cristiani, "Nonlinear properties of AlGaAs waveguides in continuous wave operation regime," *Opt. Express*, vol. 22, no. 5, p. 5291, 2014.

[38] J. J. Wathen, P. Apiratikul, C. J. K. Richardson, G. A. Porkolab, G. M. Carter, and T. E. Murphy, "Efficient continuous-wave four-wave mixing in bandgap-engineered AlGaAs waveguides," *Opt. Lett.*, vol. 39, no. 11, p. 3161, Jun. 2014.

[39] K. Dolgaleva, W. C. Ng, L. Qian, and J. S. Aitchison, "Compact highly-nonlinear AlGaAs waveguides for efficient wavelength conversion," *Opt. Express*, vol. 19, no. 13, p. 12440, 2011.

[40] B. J. Eggleton, B. Luther-Davies, and K. Richardson, "Chalcogenide photonics," *Nature Photonics*, vol. 5, no. 3. pp. 141–148, 2011.

[41] L. Petit *et al.*, "Compositional dependence of the nonlinear refractive index of new germanium-based chalcogenide glasses," *J. Solid State Chem.*, vol. 182, no. 10, pp. 2756–2761, 2009.

[42] G. P. Agrawal, "Nonlinear Fiber Optics," in *Nonlinear Science at the Dawn of the 21st Century*, Berlin, Heidelberg: Springer Berlin Heidelberg, pp. 195–211.

[43] M. Borghi, C. Castellan, S. Signorini, A. Trenti, and L. Pavesi, "Nonlinear silicon photonics Nonlinear silicon photonics," *J. Opt.*, vol. 19, no. 9, p. 93002, 2017.

[44] M. Antelius, K. B. Gylfason, and H. Sohlström, "An apodized SOI waveguide-to-fiber surface grating coupler for single lithography silicon photonics," *Opt. Express*, vol. 19, no. 4, p. 3592, 2011.

[45] M. Streshinsky *et al.*, "The Road to Affordable, Large-Scale Silicon Photonics," *Opt. Photonics News*, vol. 24, no. 9, p. 32, 2013.

[46] C. Bellegarde, H. El Dirani, … X. L.-… in P. of, and undefined 2019, "Technological advances on Si and Si3N4 low-loss waveguide platforms for nonlinear and quantum optics applications," *spiedigitallibrary.org*.

[47] R. Claps, D. Dimitropoulos, V. Raghunathan, Y. Han, and B. Jalali, "Observation of stimulated Raman amplification in silicon waveguides," *Opt. Express*, vol. 11, no. 15, p. 1731, 2003.

[48] R. L. Espinola, J. I. Dadap, R. M. Osgood, Jr., S. J. McNab, and Y. A. Vlasov, "C-band wavelength conversion in silicon photonic wire waveguides," *Opt. Express*, vol. 13, no. 11, p. 4341, 2005.

[49] F. Li *et al.*, "Error-free all-optical demultiplexing at 160Gb/s via FWM in a silicon nanowire," *Opt. Express*, vol. 18, no. 4, p. 3905, 2010.

[50] A. Biberman, M. J. Shaw, E. Timurdogan, J. B. Wright, and M. R. Watts, "Ultralow-loss silicon ring resonators," in *IEEE International Conference on*

Group IV Photonics GFP, 2012, pp. 39–41.

[51] A. Yokoo *et al.*, "Subwavelength Nanowire Lasers on a Silicon Photonic Crystal Operating at Telecom Wavelengths," *ACS Photonics*, vol. 4, no. 2, pp. 355–362, Feb. 2017.

[52] A. Liu, H. Rong, M. Paniccia, O. Cohen, and D. Hak, "Net optical gain in a low loss silicon-on-insulator waveguide by stimulated Raman scattering," *Opt. Express*, vol. 12, no. 18, p. 4261, Sep. 2004.

[53] C. Grillet *et al.*, "Amorphous silicon nanowires combining high nonlinearity, FOM and optical stability," *Opt. Express*, vol. 20, no. 20, p. 22609, 2012.

[54] A. G. Griffith *et al.*, "Silicon-chip mid-infrared frequency comb generation," *Nat. Commun.*, vol. 6, 2015.

[55] C. Ciret and S.-P. Gorza, "Generation of ultra broadband coherent supercontinuum in tapered and dispersion managed silicon nanophotonic waveguides," *J. Opt. Soc. Am. B*, vol. 34, no. 6, p. 1156, Jun. 2017.

[56] J. S. Levy, "Integrated Nonlinear Optics in Silicon Nitridewaveguides and Resonators," Cornell University, 2011.

[57] C. J. Krückel, A. Fülöp, Z. Ye, P. A. Andrekson, and V. Torres-Company, "Optical bandgap engineering in nonlinear silicon nitride waveguides," *Opt. Express*, vol. 25, no. 13, p. 15370, Jun. 2017.

[58] K. H. Nam, I. H. Park, and S. H. Ko, "Patterning by controlled cracking," *Nature*, vol. 485, no. 7397, pp. 221–224, May 2012.

[59] K. Luke, Y. Okawachi, M. R. E. Lamont, A. L. Gaeta, and M. Lipson, "Broadband Mid-Infrared Frequency Comb Generation in a Si3N4 Microresonator," in *CLEO: 2015*, 2015, p. STu4I.8.

[60] H. El Dirani *et al.*, "Crack-free silicon-nitride-on-insulator nonlinear circuits for continuum generation in the c-band," *IEEE Photonics Technol. Lett.*, vol. 30, no. 4, pp. 355–358, 2018.

[61] H. El Dirani *et al.*, "Annealing-free Si3N4 frequency combs for monolithic integration with Si photonics," *Appl. Phys. Lett.*, vol. 113, no. 8, 2018.

[62] X. Liu *et al.*, "Octave-spanning supercontinuum generation in a silicon-rich nitride waveguide," *osapublishing.org*.

[63] C. J. Krückel, A. Fülöp, T. Klintberg, J. Bengtsson, P. A. Andrekson, and V. Torres-Company, "Linear and nonlinear characterization of low-stress high-confinement silicon-rich nitride waveguides: erratum," *Opt. Express*, vol. 25, no. 7, p. 7443, 2017.

[64] M. Pu *et al.*, "Supercontinuum Generation in AlGaAs-On-Insulator Nano-Waveguide at Telecom Wavelengths," in *Conference on Lasers and Electro-Optics*, 2016.

[65] L. Ottaviano, M. Pu, E. Semenova, and K. Yvind, "Low-loss high-confinement waveguides and microring resonators in AlGaAs-on-insulator," *Opt. Lett.*, vol. 41, no. 17, p. 3996, 2016.

[66] U. D. Dave *et al.*, "Dispersive-wave-based octave-spanning supercontinuum generation in InGaP membrane waveguides on a silicon substrate," *Opt. Lett.*, vol. 40, no. 15, p. 3584, 2015.

[67] P. Winzer *et al.*, "Integrated lithium niobate electro-optic modulators operating at CMOS-compatible voltages," *Nature*, vol. 562, no. 7725, pp.

101–104, 2018.
[68] M. Pu, L. Ottaviano, E. Semenova, and K. Yvind, "Efficient frequency comb generation in AlGaAs-on-insulator," *Optica*, vol. 3, no. 8, p. 823, 2016.
[69] T. W. Baehr-Jones and M. J. Hochberg, "Polymer Silicon Hybrid Systems: A Platform for Practical Nonlinear Optics," *J. Phys. Chem. C*, vol. 112, no. 21, pp. 8085–8090, May 2008.
[70] J. Brosi *et al.*, "Silicon Organic Hybrid Technology," *Proc. IEEE*, vol. 97, no. 7, 2009.
[71] S. Mas, J. Caraquitena, J. V. Galán, P. Sanchis, and J. Martí, "Tailoring the dispersion behavior of silicon nanophotonic slot waveguides," *Opt. Express*, vol. 18, no. 20, p. 20839, 2010.
[72] A. Yariv, "Universal relations for coupling of optical power between microresonators and dielectric waveguides," *Electron. Lett.*, vol. 36, no. 11, pp. 999–999, 2000.
[73] W. Bogaerts *et al.*, "Silicon microring resonators," *Laser Photon. Rev.*, vol. 6, no. 1, pp. 47–73, Jan. 2012.
[74] I. Chremmos, N. K. Uzunoglu, and O. Schwelb, *Photonic Microresonator Research and Applications*, vol. 156. Springer, 2010.
[75] B. E. Deal and A. S. Grove, "General relationship for the thermal oxidation of silicon," *J. Appl. Phys.*, vol. 36, no. 12, pp. 3770–3778, 1965.
[76] I. Kobayashi, T. Ogawa, and S. Hotta, "Plasma-enhanced chemical vapor deposition of silicon nitride," *Jpn. J. Appl. Phys.*, vol. 31, no. 2R, pp. 336–339, Feb. 1992.
[77] P. Pan, "The Composition and Physical Properties of LPCVD Silicon Nitride Deposited with Different NH 3 / SiH2Cl2 Gas Ratios," *J. Electrochem. Soc.*, vol. 132, no. 12, p. 3001, 2006.
[78] S. A. Campbell, "The Science and Engineering of Microelectronic Fabrication (The Oxford Series in Electrical and Computer Engineering)," *Potentials*, pp. 557–565, 1996.
[79] G.W.A.D., "Introduction to microelectronic fabrication," *Microelectron. Reliab.*, vol. 28, no. 5, p. 823, Jan. 1988.
[80] R. M. De Ridder, K. Wörhoff, A. Driessen, P. V. Lambeck, and H. Albers, "Silicon oxynitride planar waveguiding structures for application in optical communication," *IEEE J. Sel. Top. Quantum Electron.*, vol. 4, no. 6, pp. 930–937, 1998.
[81] T. Gu, M. Yu, D.-L. Kwong, and C. W. Wong, "Molecular-absorption-induced thermal bistability in PECVD silicon nitride microring resonators," *Opt. Express*, vol. 22, no. 15, p. 18412, 2014.
[82] "Low pressure chemical vapor deposition," *Lnf-wiki.eecs.umich.edu*, 2019. [Online]. Available: http://lnf-wiki.eecs.umich.edu/wiki/Low_pressure_chemical_vapor_deposition. [Accessed: 30-May-2019].
[83] J. Z. Xie, "Stability of hydrogen in silicon nitride films deposited by low-pressure and plasma enhanced chemical vapor deposition techniques," *J. Vac. Sci. Technol. B Microelectron. Nanom. Struct.*, vol. 7, no. 2, p. 150, Mar. 1989.

[84] J. Riemensberger, K. Hartinger, T. Herr, … V. B.-O., and undefined 2012, "Dispersion engineering of thick high-Q silicon nitride ring-resonators via atomic layer deposition," *osapublishing.org*.

[85] C. Yang and J. Pham, "Characteristic Study of Silicon Nitride Films Deposited by LPCVD and PECVD," *Silicon*, vol. 10, no. 6, pp. 2561–2567, Nov. 2018.

[86] L. Wang, H. S. Reehal, F. L. Martínez, E. San Andrés, and A. Del Prado, "Characterization of nitrogen-rich silicon nitride films grown by the electron cyclotron resonance plasma technique," *Semicond. Sci. Technol.*, vol. 18, no. 7, pp. 633–641, Jul. 2003.

[87] Q. Lin, "Properties of Photoresist Polymers," in *Physical Properties of Polymers Handbook*, 2007, pp. 965–979.

[88] "What's the difference between an etcher and a lithography machine for making chips?," *Elinfor.com*, 2019. [Online]. Available: https://www.elinfor.com/knowledge/whats-the-difference-between-an-etcher-and-a-lithography-machine-for-making-chips-p-11025. [Accessed: 30-May-2019].

[89] K. R. Williams and R. S. Muller, "Etch rates for micromachining processing," *J. Microelectromechanical Syst.*, vol. 5, no. 4, pp. 256–269, 1996.

[90] M. Inokuti, *Advances in Atomic, Molecular, and Optical Physics: Fundamentals of Plasma Chemistry*. 1999.

[91] L. Chen, L. Xu, D. Li, and B. Lin, "Mechanism of selective Si3N4 etching over SiO2 in hydrogen-containing fluorocarbon plasma," *Microelectron. Eng.*, vol. 86, no. 11, pp. 2354–2357, Nov. 2009.

[92] C. K. Park, H. T. Kim, C. H. Lee, N. E. Lee, and H. Mok, "Effects of CH2F2 and H2 flow rates on process window for infinite etch selectivity of silicon nitride to ArF PR in dual-frequency CH2F2/H2/Ar capacitively coupled plasmas," *Microelectron. Eng.*, vol. 85, no. 2, pp. 375–387, Feb. 2008.

[93] Y. X. Li, "Selective reactive ion etching of silicon nitride over silicon using CHF3 with N2 addition," *J. Vac. Sci. Technol. B Microelectron. Nanom. Struct.*, vol. 13, no. 5, p. 2008, 1995.

[94] S. McNab, N. Moll, and Y. Vlasov, "Ultra-low loss photonic integrated circuit with membrane-type photonic crystal waveguides," *Opt. Express*, vol. 11, no. 22, p. 2927, Nov. 2003.

[95] J. Liu *et al.*, "Frequency Comb Assisted Broadband Precision Spectroscopy with Cascaded Diode Lasers," *Opt. Lett.*, vol. 41, no. 13, p. 3134, Jul. 2016.

[96] P. Del'Haye, O. Arcizet, M. L. Gorodetsky, R. Holzwarth, and T. J. Kippenberg, "Frequency comb assisted diode laser spectroscopy for measurement of microcavity dispersion," *Nat. Photonics*, vol. 3, no. 9, pp. 529–533, 2009.

[97] H. Hu *et al.*, "Single-source chip-based frequency comb enabling extreme parallel data transmission," *Nat. Photonics*, vol. 12, no. 8, pp. 469–473, 2018.

[98] T. Herr *et al.*, "Universal formation dynamics and noise of Kerr-frequency combs in microresonators," *Nat. Photonics*, vol. 6, no. 7, pp. 480–487, Jul. 2012.

[99] A. Billat, D. Grassani, M. H. P. Pfeiffer, S. Kharitonov, T. J. Kippenberg, and

C. S. Brès, “Large second harmonic generation enhancement in Si 3 N 4 waveguides by all-optically induced quasi-phase-matching,” *Nat. Commun.*, vol. 8, no. 1, p. 1016, Dec. 2017.

[100] J. S. Levy, M. A. Foster, A. L. Gaeta, and M. Lipson, “Harmonic generation in silicon nitride ring resonators.,” *Opt. Express*, vol. 19, no. 12, pp. 11415–21, 2011.

[101] A. Politi, M. J. Cryan, J. G. Rarity, S. Yu, and J. L. O’Brien, “Silica-on-Silicon Waveguide Quantum Circuits 10.1126/science.1155441,” *Science (80-.).*, vol. 320, no. 5876, pp. 646–649, 2008.

[102] F. Dell’Olio, T. Tatoli, C. Ciminelli, and M. N. Armenise, “Recent advances in miniaturized optical gyroscopes,” *J. Eur. Opt. Soc.*, vol. 9, no. 0, p. 14013, Mar. 2014.

[103] M. Belt *et al.*, “Sidewall gratings in ultra-low-loss Si_3N_4 planar waveguides,” *Opt. Express*, vol. 21, no. 1, p. 1181, Jan. 2013.

[104] X. Ji *et al.*, “Ultra-low-loss on-chip resonators with sub-milliwatt parametric oscillation threshold,” *Optica*, vol. 4, no. 6, p. 619, 2017.

[105] Y. Xuan *et al.*, “High-Q silicon nitride microresonators exhibiting low-power frequency comb initiation,” *Optica*, vol. 3, no. 11, p. 1171, 2016.

[106] D. T. Spencer, J. F. Bauters, M. J. R. Heck, and J. E. Bowers, “Integrated waveguide coupled Si_3N_4 resonators in the ultrahigh-Q regime,” *Optica*, vol. 1, no. 3, p. 153, 2014.

[107] M. H. P. Pfeiffer, J. Liu, A. S. Raja, T. Morais, B. Ghadiani, and T. J. Kippenberg, “Ultra-smooth silicon nitride waveguides based on the Damascene reflow process: fabrication and loss origins,” *Optica*, vol. 5, no. 7, p. 884, 2018.

[108] A. S. Raja *et al.*, “Electrically pumped photonic integrated soliton microcomb,” *Nat. Commun.*, vol. 10, no. 1, pp. 1–8, 2019.

[109] M. Hubert *et al.*, “Photonic Damascene Process for Low-Loss , High-Confinement Silicon Nitride Waveguides,” *IEEE J. Sel. Top. Quantum Electron.*, vol. 24, no. 4, pp. 1–11, 2018.

[110] H. Guo *et al.*, “Universal dynamics and deterministic switching of dissipative Kerr solitons in optical microresonators,” *Nat. Phys.*, vol. 13, no. 1, pp. 94–102, 2017.

[111] A. L. Gaeta, M. Lipson, and T. J. Kippenberg, “Photonic-chip-based frequency combs,” *Nat. Photonics*, vol. 13, no. 3, pp. 158–169, Mar. 2019.

[112] N. G. Pavlov *et al.*, “Narrow-linewidth lasing and soliton Kerr microcombs with ordinary laser diodes,” *Nat. Photonics*, vol. 12, no. 11, pp. 694–698, 2018.

[113] M. Faugeron *et al.*, “High-Power Tunable Dilute Mode DFB Laser With Low RIN and Narrow Linewidth,” *IEEE Photonics Technol. Lett.*, vol. 25, no. 1, pp. 7–10, Jan. 2013.

[114] D. S. Weiss, V. Sandoghdar, J. Hare, V. Lefèvre-Seguin, J.-M. Raimond, and S. Haroche, “Splitting of high-Q Mie modes induced by light backscattering in silica microspheres,” *Opt. Lett.*, vol. 20, no. 18, p. 1835, Sep. 1995.

[115] Y. K. Chembo, “Kerr optical frequency combs: theory, applications and perspectives,” *Nanophotonics*, vol. 5, no. 2, Jan. 2016.

FRENCH SUMMARY

INTRODUCTION

Les pertes de propagations dans les guides d'onde intégrés sur puce sont cruciales pour plusieurs applications telles que l'optique non linéaire [1, 2], les gyroscopes optiques [3] et les lasers à faible largueur de raie [4]. Au cours des dix dernières années, l'optique non linéaire à base de Si_3N_4 a bénéficié des progrès considérables en termes de technologie de fabrication et de compréhension physique [5] des phénomènes optiques en cause. Les peignes de fréquence optique cohérents ainsi obtenus ont permis des communications optiques à très haut débit [6], une génération hyperfréquence à faible bruit [7] et des synthétiseurs de fréquence intégrés entièrement optiques [8].

Les processus non linéaires écoénergétiques, tels que le mélange à quatre ondes et la conversion de fréquence, nécessitent de maximiser l'interaction lumière-matière. De plus, les sources de peigne de fréquence optique cohérentes nécessitent des guides d'ondes à dispersion conçus avec précision et fabriqués dans des matériaux à faibles défauts pour la formation de solitons de Kerr dissipatifs (DKS) à haute efficacité et stables en énergie. Pour ce faire, des guides d'ondes optiques présentant des pertes de propagation extrêmement faibles (~ 1 dB / m), des seuils d'endommage de la puissance élevés et le facteur de confinement le plus élevé possible sont alors nécessaires.

Les facteurs de qualité des microrésonateurs intégrés les plus élevés jamais rapportés sont obtenus dans les microrésnoteurs toroïdales en silice [9] et les résonateurs de modes de galerie MgF_2 [10]. Au-delà du faible indice non linéaire du dioxyde de silicium [11] ($2,7 \times 10^{-20}$ m^2/ W à une longueur d'onde de télécommunication de 1,5 µm), son faible indice de réfraction impose une gaine d'air et complique l'intégration. C'est pourquoi les résonateurs à facteur de qualité élevé à indice de réfraction élevé et à confinement élevé en mode optique présentent des avantages considérables. De plus, lorsque l'indice de réfraction est élevé (par exemple dans le silicium), l'indice non linéaire n_2 a tendance à être plus élevé. Cependant, la bande interdite du matériau a également tendance à être plus petite et des processus de perte non linéaires - tels que l'absorption à deux photons - auront généralement lieu. À cet égard, le nitrure de silicium (Si_3N_4) est un matériau CMOS de compromis offrant à la fois une non-linéarité relativement élevée, de faibles pertes de propagation,

l’absence de processus d’absorption directs liés à l’absorption à deux photons, tout en préservant la possibilité d’obtenir des guides d’onde à fort confinement et encapsulés totalement par la silice.

Des travaux récents basés sur de grands guides d'ondes hautement multimodes (avec des largeurs de section allant de 2,5 µm à 10 µm) ont montré des facteurs de qualité extrêmement élevés (37×10^6 et 67×10^6) [12-14]. Cependant, de tels guides d'ondes de grande taille limitent la capacité d'ingénierie précise de la dispersion, ce qui est condition indispensable à la génération de peignes de fréquences large bande en pompant dans la bande télécom (1550 nm). De plus, les interactions entre différentes familles de modes supportées par la cavité peuvent empêcher la formation de solitons, comme indiqué dans [15], [16], tandis que des pertes excessives systématiques dues aux interactions entre modes au niveau de la section de couplage du résonateur peuvent se produire [17]. Des guides d'ondes de dispersion anormaux fortement confinés d'une largeur de 1,5-2 µm et de 0,75-0,85 µm d'épaisseur sont alors nécessaires pour la génération de peignes de fréquence large bande et à seuil bas aux longueurs d'onde des télécommunications [16]. Le paramètre non linéaire γ_{nl} est un autre avantage de l’utilisation de guides d’onde fort confinement: il est inversement proportionnel à la surface de section transversale de guide d’onde A_{eff}.

Fin 2018, des guides d'ondes en nitrure de silicium à fort confinement, présentant des pertes de propagations faibles, compris entre 5 dB / m et 6 dB / m, ont été rapportés en utilisant le procédé de Damascene sur des guides d'ondes de 2 µm de large [16], [17]. Cependant, une telle approche introduit une non-uniformité d'épaisseur de film intrinsèquement sévère sur la plaque, car un tel processus implique une étape de polissage chimique-mécanique (CMP) utilisée pour l'élimination du nitrure de silicium après remplissage de la silice gravée et recuit à haute température. Cette variance induite par le CMP est beaucoup plus élevée que l'uniformité du dépôt de vaporisation chimique à basse pression (c'est-à-dire une variance sigma inférieure à 1%), et ce indépendamment de la maturité de l'outil de fabrication et de la mise à l'échelle des plaques. Plus important encore, le recuit haut température utilisé pour lisser les flancs de silice pré-tranchés introduit systématiquement une forte non-uniformité verticale dans la largeur du guide d’ondes (c’est-à-dire la pente des

flancs) de plusieurs dizaines voire centaines de nanomètres [17]. La combinaison des inhomogénéités verticales et horizontales a une incidence importante sur l'ingénierie de la dispersion et le taux de couplage du guide d'ondes de bus au microrésonateur, rendant plus difficile la réalisation d'un contrôle déterministe des largueurs des guides ainsi que des conditions de couplage.

Dans ce travail, nous décrivons la fabrication et la caractérisation linéaire de guides d'ondes Si_3N_4 à très haute perte et à très faible perte avec des coefficients d'atténuation proches de 1 dB / m, éléments essentiels de l'optique non linéaire. Ces dispositifs sont fabriqués selon un processus entièrement soustractif basé sur un recuit chimique-physique en plusieurs étapes, une encapsulation et une gravure sèche au fluorocarbure sur mesure du film de Si_3N_4. Grâce à un tel traitement, facilement accessible sur une ligne de fabrication standard et largement évolutif sur les outils de fonderie de grand format, nous obtenons facilement des facteurs de qualité intrinsèques approchants à 10^7 pour un résonateur en anneau à 200 GHz formé de guides d'ondes à dispersion anormale et fort confinement de 1,65. -µm-largeur x 800 nm-hauteur dimensions. De plus, cette approche permet une reproductibilité élevée à l'échelle de la plaque et des seuils d'endommagement extrêmement importants, grâce aux faibles niveaux de contamination des films de Si_3N_4 tels que déposés et à la méthode d'encapsulation de silice sans défauts dans la région du couplage. Les travaux établiront également des lignes directrices pour les futures percées, en analysant notamment les pertes liées à la diffusion ainsi que les mécanismes d'absorption liés aux états de surface induits par la contamination métallique résiduelle.

Cette thèse de recherche est organisée comme suit. La section II décrit le processus de fabrication, notamment les éléments de nouveauté tels que le recuit physico-chimique en plusieurs étapes, la gravure plasma au fluorocarbone et l'encapsulation multicouche appropriée des guides d'ondes Si_3N_4. Dans la section III, nous décrivons la caractérisation optique linéaire étendue de cette plate-forme en mesurant les facteurs de qualité des résonateurs. Les mesures, effectuées sur une série de microrésonateurs identiques, fournissent des informations précieuses sur les statistiques entre plaques, notamment les pertes de résonateur totales et intrinsèques

ainsi que les écarts dans les conditions de couplage critiques sur une plaque de 200 mm. La section IV évalue quantitativement les seuils de dommages de puissance causés par les ondes continues (guides d'onde), tout en présentant la susceptibilité thermique du microrésonateur et une analyse quantitative de la contamination des structures fabriquées, nécessaires à la compréhension des mécanismes de perte et de leur origine.

FABRICATION DE CIRCUITS PHOTONIQUES A BASE DE Si_3N_4 A FAIBLES PERTES

2.1 Déposition du film

Comparé à la littérature la plus récente, les pertes de propagation les plus faibles signalés pour les guides d'ondes Si_3N_4 de 2 µm de large et à fort confinement ne dépasse pas 5,5-6,5 dB / m [17]. Contrairement au traitement photonique Damascene, dans notre cas, les films de Si_3N_4 ont été déposés selon la technique déjà publiée dans [18], [19]. Cette approche, que nous avons baptisée plus tard processus de torsion-croissance, fournit des capacités de dépôt de film d'épaisseur élevée (> 1 µm) en s'adaptant à la contrainte de traction élevée, provoquant sinon la fissuration de tels films. Cette capacité devient particulièrement intéressante lorsque des films plus épaisses doivent être déposés pour de nombreuses applications, allant de la cointégration laser III-V / SiN à la photonique quantique intégrée, en passant par les peignes à fréquence optique, offrant ainsi une flexibilité exceptionnelle à notre plate-forme lorsqu'elle est déclinée sur une photonique à base de Si_3N_4. Ci-dessous, nous expliquons comment nous avons optimisé le traitement de tels films pour obtenir des microrings à facteur de qualité très élevé x 20 fois supérieurs à ceux de nos travaux antérieurs [18], [19].

2.2 Lithographie et gravure

Le processus de fabrication commence par une oxydation thermique de 3 µm d'épaisseur d'un substrat de silicium de 200 mm de diamètre. Ensuite, une couche de nitrure de silicium de 800 nm d'épaisseur (Si_3N_4) est déposée par dépôt chimique en phase vapeur à basse pression selon une méthode de dépôt publiée dans [18], [19], qui minimise la teneur en hydrogène et empêche la Si_3N_4 déposé de la fissuration, comme indiqué sur les Fig. 1 (a) et (b).

En ce qui concerne les motifs en Si_3N_4, une lithographie à UV profonds de 248 nm est ensuite réalisée avec une résine de 820 nm d'épaisseur après un revêtement anti-reflet de fond de 49 nm d'épaisseur, [Fig. 1 (c)]. Avant la gravure du Si_3N_4, les motifs de résine photosensible sont durcis avec un plasma de HBr afin d'augmenter leur résistance au plasma de gravure, et ainsi d'améliorer la sélectivité de la gravure [20]. La couche BARC est d'abord ouverte avec un procédé au plasma Ar / Cl2 / O2,

puis le Si_3N_4 est gravé avec un plasma CF4 / CHF3 / Ar dans un réacteur à couplage inductif (ICP). La sélectivité de gravure entre le Si_3N_4 et la résine durcie est de 1,2. Le masque de la résine et les polymères fluorocarbonés présents sur les parois latérales de Si_3N_4 après la gravure sont ensuite éliminés par un procédé au plasma à O2 réalisé dans un réacteur de gravure ionique réactive améliorée magnétiquement connecté au réacteur ICP par une chambre de transfert sous vide. Après le plasma, les surfaces de Si_3N_4 sont nettoyées avec une solution humide H2SO5. La Fig. 1 (d) met en évidence la bonne qualité du processus de structuration au plasma développé dans cette étude, qui permet d'obtenir des profils anisotropes bien formés, sans résidus, du guide d'ondes.

Il est à noter que dans nos travaux précédents [18], le procédé au plasma CF4 / CH2F2 / O2 utilisé pour structurer le guide d'ondes Si_3N_4 entraîne systématiquement la présence de résidus de polymères sur les flancs de nitrure de silicium. Les résidus de polymères entraînent alors inévitablement une augmentation de la rugosité du bord du guide [21], [22] et une contamination organique dans les régions critiques de ces architectures. Une solution proposée a été d'augmenter le débit d'oxygène pour réduire l'épaisseur des polymères [22]. Cependant, dans ce cas, l'oxygène diluerait la résine photosensible, entraînant une diminution de la sélectivité, ce qui augmenterait la rugosité des parois latérales. Ceci imposerait également des profils de guide d'onde trapézoïdaux d'épaisseur de guide d'ondes sub-micrométriques limités, entraînant ainsi l'imprévisibilité du taux de perte extrinsèque kc (c'est-à-dire la perte de la puissance optique du résonateur au guide d'ondes de bus). Le plasma CF4 / CH2F2 / O2 présentant certaines limitations du procédé, une chimie du plasma moins polymérisant utilisant CHF 3 au lieu de CH2F2 est avantageusement utilisée dans ce travail.

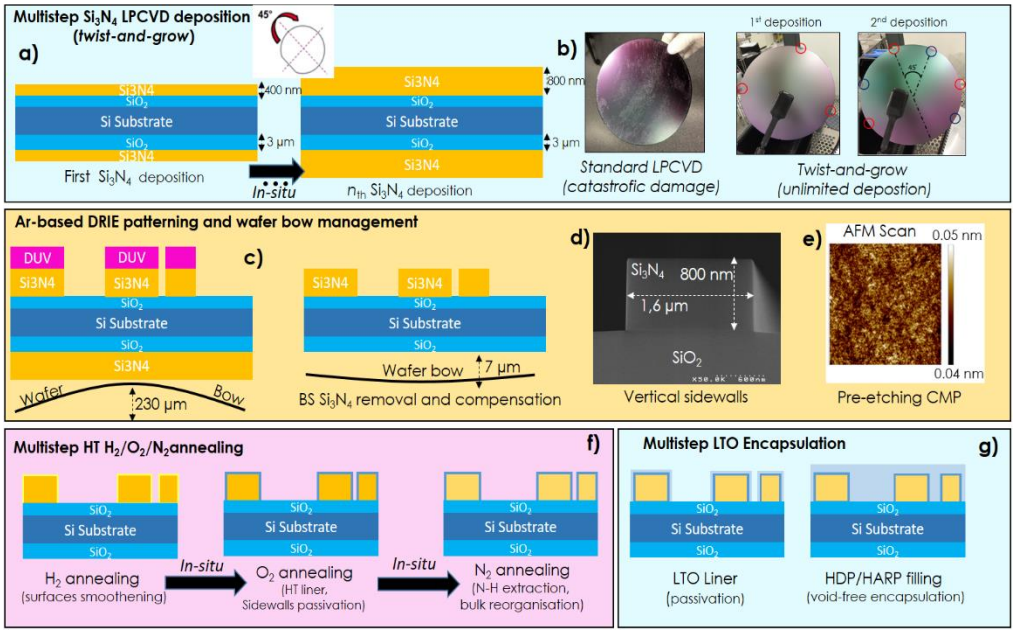

Figure 1. Schémas du processus de recuit physico-chimique par rotation et croissance en plusieurs étapes pour les guides d'ondes à faibles pertes. a) Une oxydation thermique de 3 µm d'épaisseur d'une plaque de Si de 200 mm est suivie d'un dépôt par torsion et croissance de films de Si_3N_4 jusqu'à ce que l'épaisseur de film souhaitée soit adaptée (800 nm). b) Images de films Si_3N_4 avec et sans utilisation de cette approche. c) gravure sèche à base de fluorocarbone et compensation de la contrainte de la plaque d) réduction de la rugosité supérieure du guide d'ondes à des niveaux inférieurs à Angstrom par CMP sur les films après déposition. e) Exemple d'un guide d'ondes Si_3N_4 d'une largeur de 1,6 µm et d'une épaisseur de 800 nm utilisant le procédé de gravure plasma à la CMP et au fluorocarbone, avec un angle d'inclinaison des parois latérales inférieur à 2 °. f) Recuit in situ en plusieurs étapes H_2 / O_2 / N_2 de guides d'ondes Si_3N_4. g) Encapsulation en plusieurs étapes avec de dioxyde de silicium à basse température avant l'encapsulation de silice plasma à haute densité.

Après la gravure, la plaque a une contrainte assez élevé de 230 µm qu'il faut compenser pour lui permettre de poursuivre le processus de fabrication. La contrainte est due à la présence de Si_3N_4 en traction à l'arrière de la plaque. Souvent analysés avec soin, l'impact de la contrainte sur la plaque tout au long du procès de fabrication est crucial, en particulier sur les grandes plates-formes de traitement utilisant principalement des plaques de 200 et 300 mm. L'accumulation de contraintes de compression (typiques pour le SiO_2 thermique) et de traction du film de Si_3N_4 provoque de fortes déformations des substrats porteurs de silicium. Une telle contrainte des plaques, qui peut atteindre 250-350 µm, peut endommager le film, mais aussi créer des fissures sous-micrométriques invisibles pour les yeux le long des guides d'ondes après structuration. Comme le montre la figure 1 (c), ceci peut être facilement géré par un retrait sélectif du film de Si_3N_4 restant sur la face arrière de la plaque après gravure face avant du nitrure de silicium. Cela garantira une plaque presque parfaitement plate, avec une contrainte réduite à quelques

microns seulement (contrainte mesuré ~ 7 µm sur une moyenne de la plaque croisée), ouvrant également des perspectives intéressantes pour la co-intégration photonique Si_3N_4 par collage des plaques.

Dans une approximation au premier ordre, le coefficient d'atténuation (, exprimé en dB / m) d'un guide d'ondes dépend des deux côtés, de la rugosité supérieure et inférieure du guide d'ondes [25]. En fait, avant définir les motifs, nous avons utilisé un microscope à force atomique (AFM) pour mesurer la rugosité de surface des films déposés. Les mesures AFM ont révélé une rugosité de surface de 0,4 nm des films de Si_3N_4 sans aucun traitement. Afin de réduire cette rugosité de surface à une amplitude inférieure à Angstrom, un CMP en pleine plaque de 10 nm de profondeur est réalisé sur les plaques avant lithographie. Comme le montre la figure 1 (e), la rugosité de la surface est maintenant réduite de 0,4 nm à seulement 0,09 nm (ou 0,9 Å) par la seule action bénéfique du CMP. Les guides d'ondes Si_3N_4 gravés présentent une rugosité moyenne des flancs gauche / droite carrée dans la plage de 1,2 à 1,3 nm, confirmée par les observations morphologiques AFM et CD-SEM.

2.3 Recuit physico-chimique en plusieurs étapes de guides d'ondes Si_3N_4

Le nitrure de silicium stœchiométrique déposé par dépôt chimique en phase vapeur à basse pression n'est pas totalement exempt d'hydrogène [19], [23], même lorsqu'on utilise des vitesses de dépôt ultra-faibles visant à minimiser la contenance en hydrogène. Malgré que des peignes de fréquences optique puissent être obtenus sans recuire le film du nitrure de silicium [23], soulignant de nouveau la haute qualité du matériau déposé, les facteurs de qualité des micro-anneaux résultants ont été limités à quelques centaines de milliers dans la bande C. Afin de réduire les pertes de propagation à la valeur la plus basse possible, nous avons développé et optimisé dans ce travail une séquence de recuit à haute température chimico-physique in situ à plusieurs étapes utilisant H_2, O_2 et N_2 après la gravure. La séquence est décrite, notamment pour chaque sous-étape de recuit, dans les trois paragraphes suivants.

Des études récentes ont montré que la capacité du recuit d'hydrogène pur diminuer la rugosité des parois des guides d'ondes en silicium monomodes à motifs soustractifs

pour un fonctionnement en TE à des valeurs basses, lors de la mise en oeuvre d'un tel recuit à des conditions d'exposition particulières à la pression, à la température et à la durée [26]. En suivant le même raisonnement, nous avons d'abord appliqué un recuit flash à base d'hydrogène à 1100 ° C (c'est-à-dire de quelques minutes) afin d'induire une modification morphologique du guide d'ondes. L'effet bénéfique d'un tel traitement est analysé via des tests de caractérisation morphologique et optique dans la section suivante.

Après le recuit hydrogène, les guides d'ondes ont été recuisent à 1200 ° C dans un environnement d'O_2 pendant quelques minutes. Cette étape vise à réduire les états de surface par la passivation efficace et l'encapsulation mécaniquement robuste des guide d'ondes via une oxydation native dense et à haute température de la surface de nitrure de silicium, empêchant la formation de centres d'absorption de diffusion intra-gap.

Enfin, le film de nitrure de silicium devrait être densifié par élimination de l'excès d'hydrogène et par la rupture des liaisons N-H afin de se rapprocher d'un film stoechiométrique de Si_3N_4, réduisant à son tour la perte d'absorption de matériau dans la bande C. Un recuit pur à l'azote est appliqué sur les guides d'ondes non encapsulés (1200 ° C pendant 3 heures) afin de chasser l'hydrogène résiduel, en cassant les liaisons N-H et en réduisant leur population résiduelle. Ceci fournit une énergie d'activation suffisante pour réorganiser la structure globale du guide d'ondes afin de minimiser la présence d'états de défaut global qui provoquerait une absorption néfaste [Fig. 1 (f)].

2.4 Encapsulation à plusieurs étapes oxyde native/oxyde à basse température

Bien que cela puisse sembler trivial, une encapsulation correcte du dispositif, sans vide, fournit les propriétés optiques nécessaires pour obtenir une propagation de la lumière avec des pertes très faibles.

Dans notre cas, comme pour la procédure de recuit, nous procédons à une encapsulation en plusieurs étapes pour le dépôt d'oxydes à basse température (400 °

C) consistant tout d'abord en couche mince (40 nm) à faible débit à base de tétraéthyle orthosilicate (TEOS) déposée sur l'oxyde native. Après, comme indiqué sur la figure 1 (g), plusieurs couches de silice haute densité ont été déposées afin de réaliser une encapsulation sans vide grâce aux phases alternées de gravure et de remplissage correct du dépôt chimique en phase vapeur assisté par plasma haute densité. Cette procédure nous permet d'obtenir simultanément a) une interface d'oxyde natif appropriée du guide d'onde, b) une protection contre le bombardement d'ions HDP-plasma au sommet du guide d'onde ainsi que le long de ses parois, et enfin c) a encapsulation sans vide de régions critiques de grand rapport d'aspect, en particulier dans la région de couplage entre le bus et le résonateur. En outre, une encapsulation sans vide est essentielle pour garantir la réduction de la dispersion au niveau de la région de couplage, minimiser les pertes excessives systématiques dues aux interactions intra-modales et augmenter la puissance de seuil des événements de défaillance. Ceci est de la plus haute importance, en particulier dans la perspective de la co-intégration d'amplificateurs à semi-conducteurs réfléchissants basés sur III-V ou même de sources laser multimodes autonomes, couplées bout à bout à des microrésonateurs ultra-haute Q Kerr pour des Sources peignes de fréquence optique sur puce à faible consommation d'énergie [27-31].

CARACTERISATION OPTIQUE ET ANALYSE STATISTIQUE

Afin d'évaluer l'impact des différentes étapes de traitement présentées dans la section précédente sur les performances des microrésonateurs Si_3N_4 et leur dispersion statistique entre plaques, les résonateurs en anneau sont caractérisés optiquement par des coupleurs de réseau de surface en polarisation TE sur une station de test de fibre optique de 300 mm, fournissant une perte d'insertion d'entrée / sortie (E / S) de l'ordre de 6 dB environ. Une source laser accordable fournissant une puissance d'entrée stable de 1 mW est utilisée pour le balayage sur le résonance sur les bandes S et C dans la plage de 1519-1525 nm (pour la bande S) et 1560-1562 nm (pour la bande C) avec un pas de longueur d'onde de 0,1 pm (12,5 MHz) qui correspond au pas d'échantillonnage de longueur d'onde minimum de notre source laser. Un atténuateur optique de -20 dB est utilisé avant le couplage à la puce afin d'évaluer avec précision les caractéristiques spectrales de résonance (c'est-à-dire la largeur de raie de résonance) à de faibles niveaux de puissance, afin de supprimer le biais de résonance provenant de la susceptibilité thermique th du microrésonateur [16]. Le schéma de configuration de mesure ainsi qu'une image au microscope optique à vue de dessus des résonateurs en anneau sont représentés sur les Fig. 2 (a, b).

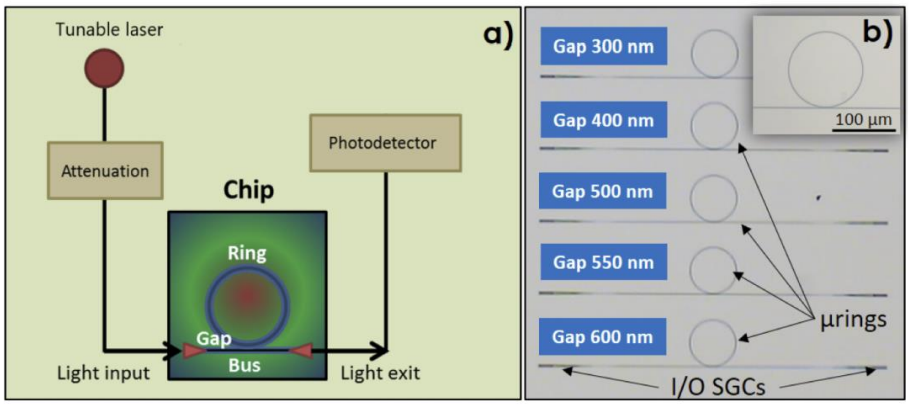

Figure 2. Représentation schématique de a) la configuration de mesure optique utilisée pour la caractérisation des microrésonateurs et des structures de test. La spectroscopie par balayage laser direct est réalisée à l'aide d'un photodétecteur à haute sensibilité. b) Image au microscope des résonateurs en anneau à 200 GHz-FSR avec différentes configurations de bus / anneaux. Le signal d'entrée / sortie (I / O) est collecté via des coupleurs de réseau de surface (SGC) fonctionnant en polarisation TE.

3.1. Calcul du coefficient d'atténuation via l'analyse du spectre des résonateurs sous-couplés

La lumière polarisée TE est injectée dans les guides d'ondes de bus via les SCG d'entrée, puis couplée dans une série de microrings nominalement identiques utilisant différents espaces séparant le résonateur en anneau du guide d'ondes afin de produire différents régimes de couplage de microrésonateurs. La dimension de la section transversale du guide d'ondes (w*x*h) est de 1,65 µm x 0,8 µm, tandis que cinq écarts entre le bus et l'anneau sont testés de 300 nm à 600 nm, afin d'accéder à une distribution statistique des performances du dispositif sur-couplé, couplée de manière critique, et des régimes sous-couplés. La configuration sous-couplée est la plus appropriée pour évaluer les facteurs de qualité intrinsèques Q_0 et les largeurs de raie $\kappa_0/2\pi$ ainsi que les pertes d'atténuation α_i (dB / m) des guides d'onde de microrésonateurs [21], tandis que le régime à couplage critique optimise le charge sur les microrésonateurs et les taux d'extinction de la transmission. Sur la figure 2 (b), nous montrons une image au microscope d'un jeu de puces typique contenant les cinq configurations testées de microrésonateurs à gamme spectrale libre (FSR) de 200 GHz.

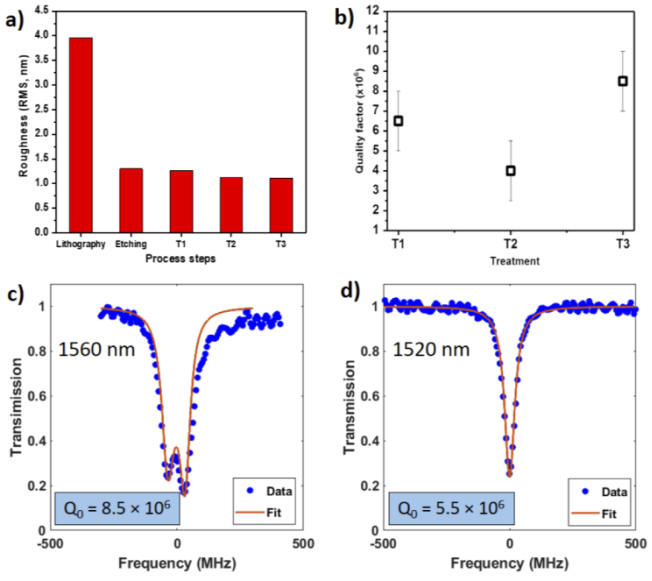

Figure 3-(a) Évolution de la rugosité des parois latérales du guide d'onde pendant le processus de fabrication (lithographie, gravure sèche), y compris la comparaison de différentes stratégies de recuit de post-gravure (T1, T2 et T3). (b) Facteurs de qualité et taux d'extinction en fonction du traitement de recuit utilisé. c) Doublet de résonance à λ =1560 nm nm présentant une largeur de raie de perte totale de 23 MHz correspondant à un Q_0 ~

8.5 *x* 10^7 intrinsèque, et un taux de division ajusté $\Omega/2\pi$ = 62 MHz (plaque T3). d) Doublet de résonance à λ = 1520 nm présentant une largeur de raie de perte totale de 36 MHz correspondant à une valeur intrinsèque $Q_0 \sim 5.3$ *x* 10^6, et un taux de division ajusté $\Omega/2\pi$ = 50 MHz (tranche T3).

Les résultats de la figure 3 (a) montrent la rugosité des parois latérales du guide d'ondes non revêtue mesurée par analyse de données au microscope électronique à balayage de dimension critique à différents stades du traitement du guide d'ondes et pour différents traitements de recuit de post-structuration. Tout d'abord, la rugosité des parois latérales diminue d'environ 4 nm après la lithographie à 1,25 nm juste après l'attaque du guide d'ondes Si_3N_4. Comme autre preuve de la haute qualité du processus de structuration développé dans ce travail, les guides d'ondes résultants présentent des profils anisotropes bien formés, comme le montre déjà la Fig. 1 (d). De plus, la figure 3 (a) compare trois traitements thermiques différents après traitement thermique à haute température dans différents environnements chimiques. Plus précisément, nous avons désigné ces traitements thermiques physico-thermiques comme suit: a) traitement T1 (utilisant seulement 100% de N_2 à 1200 ° C pendant 3 heures), b) traitement T2 (utilisant 99% de N_2 + 1% d'O_2 à 1200 ° C) pendant 3 heures) et enfin c) le traitement T3 (recuit flash à 1100 ° C sous H2 suivi d'un recuit à 100% d'O2 pendant 20 minutes et de 100% de N_2 pendant 3 heures, les deux derniers étant effectués à 1200 ° C). Comme indiqué sur la figure 3 (a), ces trois post-traitements n'ont pas d'effet remarquable sur la rugosité de la paroi latérale par rapport aux dispositifs gravés, sauf une légère amélioration lors de l'utilisation du recuit flash sous atmosphère de H2 pur (plaquette T3) où la valeur efficace atteint ~ 1,1 nm. En réalité, ce traitement se révélera décisif pour la réalisation de guides d'ondes avec des pertes ultra-faibles. Afin d'évaluer le coefficient d'atténuation des guides d'ondes du résonateur sur la plaque T3 (ayant subi le traitement de recuit H2) via les facteurs de qualité intrinsèques, nous avons commencé l'analyse des résonateurs fonctionnant dans le régime sous-couplé, afin de minimiser la contribution des pertes excédentaires résultant de la non-idéalité du couplage, et ont donc le taux de perte interne $\kappa_0/2\pi$ dominant le taux de perte totale. En détail, l'analyse est effectuée en mesurant les largeurs de raie de résonance du spectre de transmission. Ceci fournit le taux de perte totale du résonateur $\kappa/2\pi = (\kappa_0 + \kappa_{ex})/2\pi$,

qui est la somme du taux de perte de couplage $\kappa_{ex}/2\pi$ du bus vers le microrésonateur et du taux de perte intrinsèque du microrésonateur $\kappa_0/2\pi$.Des résonateurs sous-couplés ont été trouvés uniquement pour l'écart maximal disponible sur l'ensemble de masques (c'est-à-dire, un écart de 600 nm). Comme présenté sur les Fig. 3 (c, d), des doublets de résonance, provenant de la rétrodiffusion cohérente dans le microrésonateur et d'une signature optique typique des résonateurs à ultra haute Q, pourraient être facilement observés sur toute la plaque pour un tel taux de couplage. Comme le montre la figure 3 (c), en utilisant un modèle d'ajustement de forme de ligne de doublet résonant, une largeur de ligne de perte totale (chargée) $\kappa/2\pi$ de 18 MHz, correspondant à des facteurs de qualité intrinsèques $Q_0 \sim 8{,}5 \times 10^6$ à une longueur d'onde de 1560 nm (bande C) pour un taux de perte interne ajusté estimé à $\kappa_0/2\pi = 23$ MHz et un taux de division ajusté $\Omega/2\pi = 62$ MHz.

En répétant la même mesure à 1520 nm (bande S) illustrée à la Fig. 3 (d), nous avons extrait des largeurs de raie intrinsèques de 36 MHz correspondant à des Q intrinsèques élevés supérieurs à $5{,}3 \times 10^6$. Cela indique que l'absorption de N*H résiduelle provenant du matériau Si_3N_4 a été presque totalement éliminée des guides d'ondes par les étapes de recuit in situ. En comparant les Figs. 3 (c, d), l'augmentation des pertes à cette longueur d'onde décalée vers le bleu provient cependant de l'absorption harmonique de la population de liaisons N-H résiduelles encore présente dans le film et responsable d'une différence d'environ 20 MHz par rapport aux largeurs de raie totales comprises entre 1520 nm et 1560 nm. La figure 3 (b) montre les facteurs de qualité intrinsèques et les taux d'extinction extraits de ces mesures lors de la comparaison de l'utilisation des trois traitements de recuit différents T1, T2 et T3. On peut notamment déduire de ces résultats que le meilleur coefficient d'atténuation a été obtenu sur la plaquette T3, qui a subi le traitement de recuit éclair H2. Comme déjà mentionné, le traitement T3 entraîne une augmentation du facteur Q0 intrinsèque mesuré par rapport aux deux autres processus de recuit. Cela peut s'expliquer par le fait que ce traitement permet un lissage supplémentaire (bien que fractionnel) des guides d'ondes comme indiqué sur la figure 3 (a), et donc une forte réduction des pertes liées à la diffusion.

L'analyse des propriétés spectrales des résonances du microrésonateur permet de déduire le coefficient d'atténuation des guides d'ondes. La valeur intrinsèque Q_0 est liée au coefficient d'atténuation sous la forme $\alpha = k_0 n_{eff}/Q_0$, où k_0 est le nombre d'onde et n_{eff} est l'indice effectif du mode fondamental optique en polarisation TE (1,79 dans notre cas). Cela correspond donc dans notre cas à un coefficient d'atténuation aussi faible que ~ 1,6 dB / m pour une longueur d'onde de 1560 nm, ce qui représente la plus faible perte de propagation pour les guides d'ondes en nitrure de silicium à fort confinement rapportés jusqu'à présent [17]. Notez que ces pertes de propagation estimées constituent une estimation prudente du coefficient d'atténuation réel, car nous fonctionnons toujours à la limite du régime sous-couplé en utilisant la dimension d'écart maximale disponible sur le jeu de masques. Une deuxième source de surestimation des pertes de propagation provient du fait que nous extrayons les pertes à partir de mesures facteur de qualité des résonateurs en anneau. Dans un anneau, le mode optique interagit davantage avec la rugosité de la paroi latérale due à la flexion, en particulier lorsqu'il fonctionne en polarisation TE.

En résumé, les pertes optiques ultra-faibles obtenues pour le recuit à plusieurs étages H_2 / O_2 / N_2 et le traitement d'encapsulation séquentiel résultent de la combinaison de plusieurs améliorations intrinsèques de la structure des matériaux et des dispositifs. Cela provient en premier lieu de a) la réorganisation structurelle et b) de la déshydrogénation par recuit N_2 du film de Si_3N_4, puis c) d'une passivation effective à l'état de surface et d) de la protection des guides d'ondes contre le bombardement ionique pendant l'encapsulation en faisant un recuit O_2 contrôlé, pour créer un oxyde natif et grâce à l'oxyde basse température, et enfin e) la diminution de la perte de diffusion par lissage de la paroi latérale via un recuit flash H_2 .

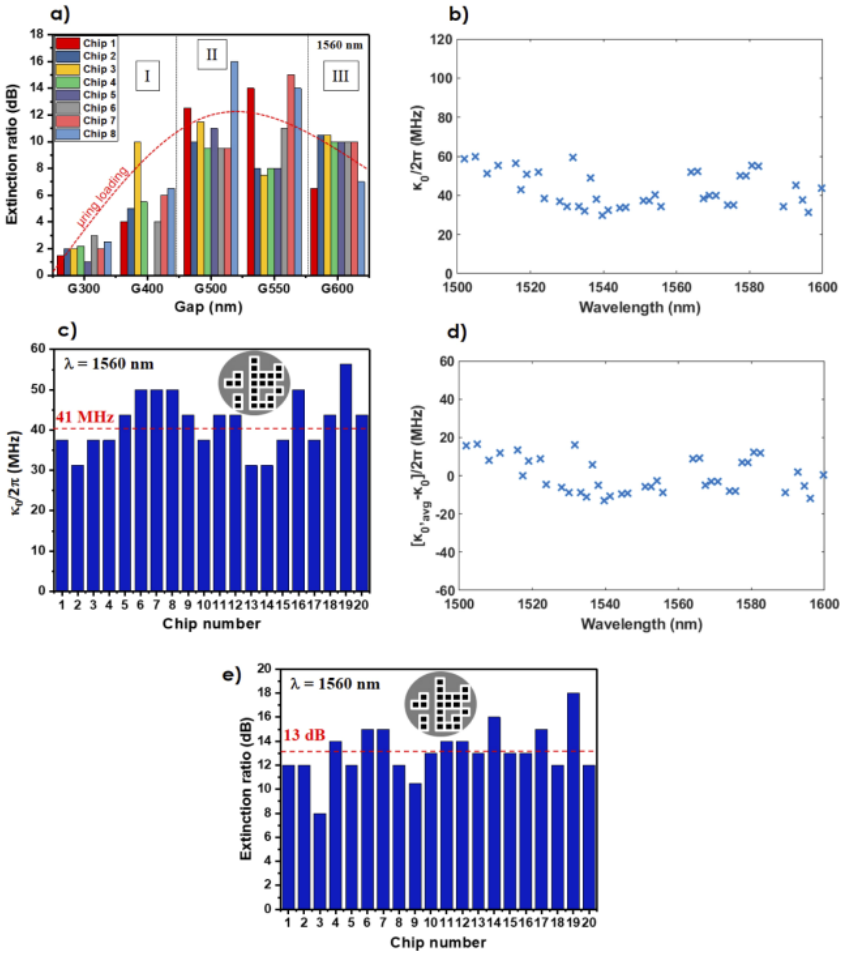

Figure 4. (a) Taux d'extinction des résonateurs avec intervalle spectrale libre de 200 GHz surcouplés (zone I) et quasi en couplage critique (zone II) et sous-couplés (zone III). (b, d) Largeurs de raie intrinsèques (MHz) et leur variation absolue par rapport à la largeur de raie moyenne sur les longueurs d'onde de 1500 à 1600 nm (bandes S, C et L), (c) Largeurs de raie intrinsèques (MHz) et (e) dispositifs à couplage critique (intervalle de couplage = 550 nm) mesurés dans un intervalle de longueur d'onde de 20 nm centré à 1560 nm et échantillonnés sur 20 matrices différentes (avec les valeurs moyennes respectives indiquées par une ligne pointillée rouge). Les positions relatives des 20 matrices sur la tranche T3 de 200 mm sont indiquées dans l'encadré de (c, e).

3.2. Analyse statistique des résonateurs à couplage critique

Suite à cela, une caractérisation optique approfondie des dispositifs était obligatoire pour étudier l'impact des différents traitements post-recuit sur les performances globales du dispositif. Cela inclut le taux d'extinction, la largeur de raie intrinsèque $\kappa_0/2\pi$ ainsi que la déviation des longueurs d'onde absolues de résonance telles que fabriquées à 1561 nm de microrésonateurs nominalement identiques. Comme le montre la figure 4 (a), une étude statistique est réalisée sur la configuration susmentionnée de cinq espaces de bus à anneau afin de discriminer les dispositifs

sucouplés (zone I), en couplage critique (zone II) et sous-couplés (zone III). Une telle répartition des dispositifs sur les trois zones susmentionnées est basée sur les taux d'extinction des microrésonateurs. Les dispositifs sous-couplés de la zone III ont un intervalle de couplage bus-à-microrésonateur de 600 nm, le plus grand disponible sur notre ensemble de masques. D'autre part, les dispositifs utilisant un intervalle de couplage de 550 nm présentent statistiquement les taux d'extinction les plus élevés et fonctionnent donc à proximité des conditions de couplage critiques à une longueur d'onde de 1561 nm. En outre, l'analyse est effectuée sur la tranche de type 3 (T3), qui a subi un recuit H2 instantané et présente les valeurs de coefficient d'atténuation et de rugosité des parois latérales du guide d'onde les plus faibles.

Afin d'estimer la reproductibilité élevée des pertes optiques et du facteur de qualité après notre processus de fabrication totalement soustractif, une étude statistique sur 20 puces (partie de la même plaquette de 200 mm) est réalisée pour l'espace de couplage de 550 nm de large à λ = 1561 nm, afin de fonctionner près des conditions de couplage critiques. Premièrement, l'écart de longueur d'onde de résonance absolue de λ = 1561 nm est analysé.

Comme indiqué sur la figure 4 (b), les longueurs d'onde absolues couvrent un intervalle spectral aussi étroit que 1,8 nm, plus de 75% des dispositifs se situant dans la région de déviation inférieure au nm. La valeur de la largeur de raie intrinsèque $\kappa_0/2\pi$ indiquée à la Fig. 4 (c) est lue à une valeur moyenne de 41,2 MHz, avec un écart-type de seulement 6,8 MHz.

Enfin, en ce qui concerne les taux d'extinction des microrésonateurs, lorsque l'écart entre l'anneau et le guide d'ondes est de 550 nm, plus de 10 dB sont obtenus sur 95% des dispositifs testés, comme illustré à la Fig. 4 (d). De plus, la valeur moyenne calculée pour le taux d'extinction est de 13,1 dB, avec un écart type de seulement 2,1 dB échantillonné sur la plaque de 200 mm. De tels résultats reflètent l'uniformité extrêmement élevée du dépôt en épaisseur de film Si_3N_4, tout en confirmant la haute reproductibilité de toute la technologie sur un réticule.

LIMITES D'ABSORPTION INTRINSEQUE, SUSCEPTIBILITE THERMIQUE ET FIABILITE DES COMPOSANTS

Enfin, nous avons étudié et mesuré par fluorescence X à réflexion totale (TXRF) la nature et la concentration relative de la contamination métallique contenue dans le film de Si_3N_4. En fait, la présence de tels éléments métalliques peut jouer le rôle de centre de diffusion à mi-gap responsable de l'absorption des photons à la fois dans le corps du guide et à la surface du guide d'ondes. Les résultats de la figure 5 (a) montrent que de très faibles niveaux de contamination sont présents, notamment Ca et K (10^{11} atomes / cm²), tandis que les contaminants provenant de Fe, Co, Cr, Cu présentent des niveaux compris entre 10^{10} et 10^{11} atomes / cm². La présence de Ca et de K est notamment liée à la contamination résiduelle provenant de l'eau dé-ionisée utilisée pour le nettoyage des plaquettes, tandis que Cu, Al, Ni, Ti sont plutôt issus de la technologie des métaux de contact à base de CMOS. L'origine de la contamination par Fe, Al, Zn peut être liée à un dopage épitaxial et à un substrat InP et GaAs, ainsi qu'à des compositions d'alliages ternaires et quaternaires III-V.

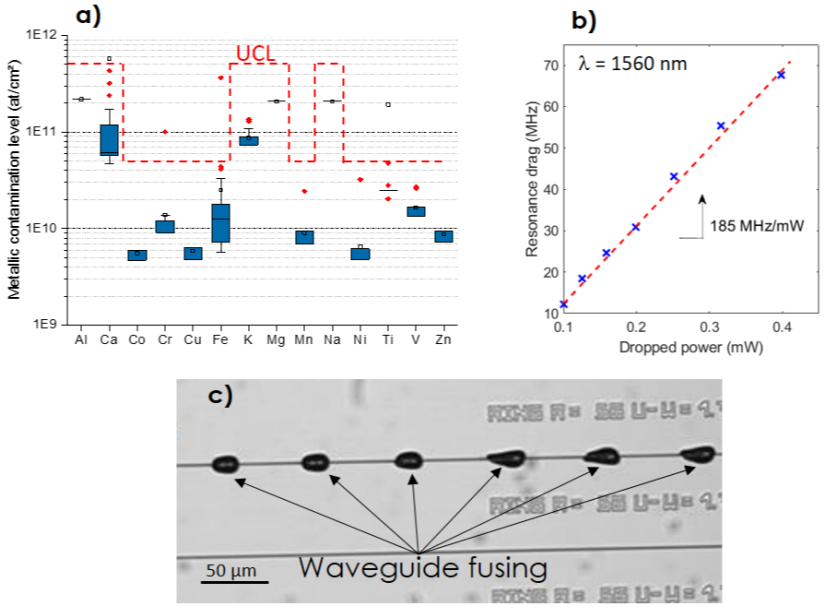

Fig. 5. (a) Analyse TXRF de la contamination métallique des films de Si_3N_4 tels que déposés tels que décrits et traités dans ce travail. La ligne rouge (appelée UCL) indique la «limite de contamination supérieure» détectée dans le film par rapport aux éléments métalliques d'intérêt. (b) Des traînées de résonance extraites (MHz) pour différentes puissances (mW) révélant la susceptibilité thermique du résonateur χ_{th} = 185 MHz / mW à une longueur d'onde de 1560 nm. (c) Image d'un événement de défaillance lorsqu'une puissance optique d'entrée CW de +38 dBm est couplée à un guide d'onde Si_3N_4. L'événement de défaillance n'a été observé qu'une seule fois lors de mesures à de tels niveaux de puissance. Aucun événement de défaillance n'a été observé sur aucun microrésonateur lors des tests à des niveaux de puissance aussi élevés.

Les niveaux de contamination détectés dans le film utilisé dans ce travail sont inférieurs de 6 à 7 ordres de grandeur aux valeurs rapportées pour le procédé

photonique Damascene [16]. Cela ouvre clairement des perspectives intéressantes pour l'identification et l'atteinte des limites ultimes de l'absorption globale de Si_3N_4 et de la réduction ultérieure des pertes de propagations. De plus, un faible niveau de contamination contribue à réduire la susceptibilité thermique des dispositifs, ce qui est par exemple de la plus haute importance pour la stabilité des dispositifs d'optique quantique en fonctionnement. De toute évidence, la susceptibilité thermique χ_{th} (c'est-à-dire la bistabilité thermique) des résonateurs intégrés à perte ultra-faible Si_3N_4 est lié à la densité apparente des contaminants métalliques qui jouent le rôle de centres de diffusion d'événements de recombinaison non radiative, produisant principalement une émission de phonons. La susceptibilité thermique est à son tour liée au taux de perte d'absorption et à la contribution globale des pertes non liées à la diffusion dans le système de guides d'ondes [16]. Comme indiqué sur la figure 5 (b), nous avons extrait le χ_{th} de la pente du droit du déplacement de la résonance (en MHz) en fonction de la puissance couplée dans l'anneau (en mW). Ceci révèle une susceptibilité thermique du microrésonateur de 185 MHz / mW pour un résonateur à couplage critique à une longueur d'onde de 1560 nm. Cette valeur est environ 30% plus petite que celle rapportée précédemment [16, Fig. 3 (b)] lors de la comparaison de la même méthodologie pour la déduction de la susceptibilité thermique.

Les seuils d’endommagement sont également très importants pour évaluer la fiabilité et le vieillissement de l’appareil. Des tests optiques approfondis sous injection à onde continue à des puissances allant jusqu'à +20 dBm ont été effectués sur les mêmes puces pendant plus de 3 mois, sans modification visible des propriétés spectrales (et matérielles) des microrésonateurs. Les dispositifs ont également subi des tests de résistance à des niveaux de puissance d'onde continue très élevés, avec des puissances couplées au guide d'ondes de bus d'environ +40 dBm. Aucun cas de défaillance d'un dispositif microrésonateur n'a jamais été observé pendant toute la durée du test pour de tels niveaux de puissance. Cependant, un seul événement de défaillance d'un guide d'onde s'est produit, dont les résultats sont présentés sur la figure 5 (c).

CONCLUSIONS ET PERSPECTIVES

Dans ce travail, nous avons présenté à la fois la fabrication et les tests de guides d'ondes Si_3N_4 à perte ultra-faible à confinement élevé et de microrésonateurs à Q élevé présentant des coefficients d'atténuation aussi faibles que 1,6 dB par mètre et des facteurs de qualité intrinsèques approchant à 8,5 x 10^6 sur la bande C, respectivement. Ces appareils présentent de très faibles écarts de performances avec une uniformité élevée sur une échelle de tranche de 200 mm, une faible susceptibilité thermique et des seuils de dommages en CW élevés. Cela a été rendu possible grâce au développement d'un procédé optimisé entièrement soustractif introduisant un nouveau recuit chimique-physique à plusieurs étapes et un procédé d'encapsulation soigneusement adapté. Cette technologie produit des circuits optiques à base de Si_3N_4 de haute qualité, parfaitement adaptés à la photonique non linéaire à haut rendement énergétique et à l'optique quantique intégrée.

Références

1. A. Politi, M. J. Cryan, J. G. Rarity, S. Yu, and J. L. O'Brien, "Silica-on-silicon waveguide quantum circuits 10.1126/science.1155441," *Sci.,* **320**, 646–649, (2008).
2. S. Ramelow, A. Farsi, Z. Vernon, S. Clemmen, X. Ji, J. E. Sipe, M. Liscidini, M. Lipson, and A. L. Gaeta, "Strong nonlinear coupling in a Si_3N_4 ring resonator," *Phys. Rev. Lett.,* **122**, 153906, (2019).
3. F. Dell'Olio, T. Tatoli, C. Ciminelli, and M. N. Armenise, "Recent advances in miniaturized optical gyroscopes," *J. Eur. Opt. Soc.,* **9**, 14013 (2014).
4. M. Belt, J. Bovington, R. Moreira, J. F. Bauters, M. J. Heck, J. S. Barton, J. E. Bowers, and D. J. Blumenthal, "Sidewall gratings in ultra-low-loss Si_3N_4 planar waveguides," *Opt. Exp.* **21**, 1181 (2013).
5. T. Herr, K. Hartinger, J. Riemensberger, C. Y. Wang, E. Gavartin, R. Holzwarth, M. L. Gorodetsky and T. J. Kippenberg, "Universal formation dynamics and noise of Kerr-frequency combs in microresonators," *Nat. Phot.*, **6** (2012).
6. P. Marin-Palomo, J. N. Kemal, M. Karpov, A. Kordts, J. Pfeifle, M.H. Pfeiffer, P. Trocha, S. Wolf, V. Brasch, M.H. Anderson, and R. Rosenberger, "Microresonator-based solitons for massively parallel coherent optical communications," *Nat.*, **546**, 274–279 (2017).
7. W. Liang *et al.*, "High spectral purity Kerr frequency comb radio frequency photonic oscillator," *Nat. Commun.*, **6,** 7957 (2015).
8. D.T. Spencer, T. Drake, T.C. Briles, J. Stone, L.C. Sinclair, C. Fredrick, Q. Li, D. Westly, B.R. Ilic, A. luestone, and N. Volet, "An optical-frequency synthesizer using integrated photonics," *Nat.*, **7703**, p.81 (2018).
9. H. Lee , T. Chen, J. Li, K. Y. Yang, S. Jeon, O. Painter, and K. J. Vahala, "Chemically etched ultrahigh-Q wedge-resonator on a silicon chip," *Nat. Phot.* **6**, 369–373, Jun. 2012.
10. N. G. Pavlov, S. Koptyaev, G. V. Lihachev, A. S. Voloshin, A. S. Gorodnitskiy, M. V. Ryabko, S. V. Polonsky & M. L. Gorodetsky, "Narrow-linewidth lasing and soliton Kerr microcombs with ordinary laser diodes," *Nat. Phot.*, **12** (2019).
11. M. J. Weber, D. Milam. and W. L. Smith, "Nonlinear refractive index of glasses and crystals", *Opt. Eng.*, 17, 463 (1978)
12. X. Ji, A. B. Felippe, S. P. Roberts, A. Dutt, J. Cardenas, Y. Okawachi, A.Bryant, A. L. Gaeta, and M. Lipson., "Ultra-low-loss on-chip resonators with sub-milliwatt parametric oscillation threshold," *Optica* **4**, 619 (2017).
13. Y. Xuan, Y. Liu, L.T. Varghese, A.J. Metcalf, X. Xue, P.H. Wang, K. Han, J.A. Jaramillo-Villegas, A. Al Noman, C. Wang, and S. Kim, "High-Q silicon nitride microresonators exhibiting low-power frequency comb initiation," Optica 3, 1171 (2016).
14. D. T. Spencer, J. F. Bauters, M. J. R. Heck, and J. E. Bowers, "Integrated waveguide coupled Si_3N_4 resonators in the ultrahigh-Q regime," *Optica* **1**, 153 (2014).

15. T. Herr, V. Brasch, J. Jost, I. Mirgorodskiy, G. Lihachev, M. Gorodetsky, and T. J. Kippenberg," Mode spectrum and temporal soliton formation in optical microresonators" Phys. *Rev. Lett.,* **113**, 123901 (2014).
16. M. H. P. Pfeiffer, J. Liu, A. S. Raja, T. Morais, B. Ghadiani, and T. J. Kippenberg, "Ultra-smooth silicon nitride waveguides based on the Damascene reflow process: fabrication and loss origins," *Optica*, **5**,884, (2018).
17. M. H. P. Pfeiffer, C. Herkommer, J. Liu, T. Morais, M. Zervas, M. Geiselmann, and T. J. Kippenberg, "Photonic Damascene process for low-loss, high-confinement silicon nitride waveguides," *IEEE J. of. Sel. Top. Quantum Elec.,* **24**, 4 (2018).
18. H. El Dirani, M. Casale, S. Kerdiles, C. Socquet-Clerc, X. Letartre, C. Monat, C. Sciancalepore, "Crack-free silicon-nitride-on-insulator nonlinear circuits for continuum generation in the C-band," in *IEEE Phot. Technol. Lett.,* **30**, 355-358 (2018).
19. H. El Dirani, A. Kamel, M. Casale, S. Kerdiles, C. Monat, X. Letartre, M. Pu, L. K. Oxenløwe, K. Yvind, C. Sciancalepore, "Annealing-free Si_3N_4 frequency combs for monolithic integration with Si photonics," *App. Phys. Lett.,* **8**, 113 (2018).
20. L. Azarnouche, E. Pargon, K. Menguelti, M. Fouchier, O. Joubert, P. Gouraud, C. Verove, "Benefits of plasma treatments on critical dimension control and line width roughness transfer during gate patterning," *J. Vac. Sci. Technol., B* **31**, 012205 (2013).
21. M. Schaepkens, T. E. F. M. Standaert, N. R. Rueger, P. G. M. Sebel, G. S. Oehrlein, and J. M. Cook, "Study of the SiO_2-to-Si_3N_4 etch selectivity mechanism in inductively coupled fluorocarbon plasmas and a comparison with the SiO_2-to-Si mechanism," *J. Vac. Sci. Technol.,* A **17**, 26–37 (1999).
22. D. Beery, K. Reinhardt, P. B. Smith, J. Kelley, and A. Sivasothy, "Post etch residue removal: novel dry clean technology using densified fluid cleaning (DFC)," in *IEEE International Interconnect Technology Conference* (Cat. No. 99EX247) 140–142 (1999).
23. J. Z. Xie, "Stability of hydrogen in silicon nitride films deposited by low-pressure and plasma enhanced chemical vapor deposition techniques," *J. Vac. Sci. Technol. B Microelectron. Nanom. Struct.,* **7**,150 1989.
24. M. H. Pfeiffer, A. Kordts, V. Brasch, M. Zervas, M. Geiselmann, J. D.Jost, and T. J. Kippenberg, *Optica* **3**, 20 (2016).
25. F. P. Payne, J. P. R. Lacey, "A theoretical analysis of scattering loss from planar optical waveguides," *Opt. and Quant. Elec.,* **26**, 977 (1994).
26. C. Bellegarde, E. Pargon, C. Sciancalepore, C. Petit-Etienne, V. Hughes, D. Robin-Brosse, J.-M. Hartmann, P. Lyan, "Improvement of sidewall roughness of sub-micron SOI waveguides by hydrogen plasma and annealing" in *IEEE Phot. Technol. Lett.,* **30**, 591-594 (2018).
27. A. Matsko, A. Savchenkov, D. Strekalov, V. Ilchenko, and L. Maleki,"Optical hyperparametric oscillations in a whispering-gallery-mode resonator: threshold and phase diffusion," *Phys. Rev. A* **71**, 033804 (2005).

28. S. A. Raja et al., “Electrically pumped photonic integrated soliton microcomb,” *Nature Comm.* **1**, 680, (2019).
29. A. L. Gaeta, M. Lipson, T. J. Kippenberg, “Photonic-chip-based frequency combs,” *Nat. Phot.*, **13**, 158-169 (2019).
30. S. Boust, H. El Dirani, F. Duport, L. Youssef, S. Kerdiles, Y. Robert, C. Petit-Etienne, M. Faugeron, E. Vinet, M. Viallet, E. Pargon, C. Sciancalepore, F. Van Dijk, “Compact optical frequency comb source based on a DFB butt-coupled to a silicon nitride microring,” *IEEE Microwave Photonics Conference*, (2019).
31. J. Liu, A. S. Raja, M. Karpov, B. Ghadiani, M. H. P. Pfeiffer, B. Du, N. J. Engelsen, H. Guo, Mi. Zervas, and T. J. Kippenberg, “Ultralow-power chip-based soliton microcombs for photonic integration,” *Optica*, **5**, 10 , pp.1347-1353, (2018).